UNIVERSITY OF CALIFORNIA, SAN DIEGO

Experimental and Numerical Investigation of the Seismic Performance of Reinforced Masonry Structures

A dissertation submitted in partial satisfaction of the requirements for the degree Doctor of Philosophy

in

Structural Engineering

by

Marios Mavros

Committee in charge:

Professor P. Benson Shing, Chair
Professor Yuri Bazilevs
Professor Juan C. del Alamo
Professor Francesco Lanza Di Scalea
Professor Jose I. Restrepo

2015

The dissertation of Marios Mavros is approved and it is acceptable in quality and form for publication on microfilm and electronically:

_____

_____

_____

_____

_____

Chair

University of California, San Diego

2015

DEDICATION

To my family and friends

TABLE OF CONTENTS

LIST OF SYMBOLS

Chapter 2

Section 2.3

E_s	Initial elastic modulus of steel
E'_u	Unloading modulus of steel
P	Exponent that characterizes the hardening regime for the Dodd-Restrepo steel model
f'	True stress
f'_a	Stress at the end of the elastic region during unloading
f'_r	Stress at a reversal point
f'_{sh}	Stress at the onset of strain hardening
$f'_{sh,1}$	Stress of a point lying on the hardening regime
f'_t	Stress at the target point
f'_u	Ultimate stress
f_y	Yield stress of the steel in engineering coordinate system
f'_y	Yield stress of the steel in natural coordinate system
s	Parameter defining the direction of the strain increment
ε	Engineering strain
ε'	Natural strain
ε'_M	The maximum attained magnitude of strain

ε_r'	Strain at a reversal point
ε'_{sh}	Strain at the onset of strain hardening
$\varepsilon_{sh,1}'$	Strain of a point lying on the hardening regime
ε_t'	Strain at the target point
ε'_u	Strain at which the reinforcing bar fractures
$\varepsilon_{su,shift}'$	Shifted ultimate strain
ε'_y	Yield strain
ε_a'	Strain at the end of the elastic region during unloading
$\Delta\sigma_r$	Stress between two reversal points
σ	Engineering stress
$\varepsilon_o'(1), \varepsilon_o'(2)$	Strain of the shifted origins in the positive and negative directions, respectively

Section 2.4

E_c	Young's modulus of concrete
G_{f1}	Fracture energy
L_{ch}	Characteristic length
m_t	Tensile shape factor
f_c'	Concrete compressive strength
f_o	Initial yield stress

f_t	Tensile strength of masonry
r_c	Percentage of the residual concrete compressive strength
r_t	Percentage of the residual concrete tensile strength
ε_{cr}	Strain at which maximum tensile strength is attained
ε_e	Strain at which the linear elastic region in compression ends
ε_p	Plastic strain
ε_u	Ultimate strain for the orthotropic law
ε_{up}	Ultimate strain for the plasticity law
ε_1	Strain at which maximum compressive strength is attained for the orthotropic law
ε_2	Strain at which the linear degradation of the orthotropic law in compression begins
ε_{1p}	Effective strain at which maximum effective stress is attained
ε_{2p}	Effective strain at which the linear degradation of the effective stress begins
σ_e	Effective stress
σ_{2o}	Stress at which the concrete is considered crushed in the orthotropic law
σ_{2p}	Effective stress at which the concrete is considered crushed in the plasticity law
σ_1, σ_2	Maximum and minimum principal stresses, respectively

Section 2.5

$\mathbf{d}$	Vector of the relative displacements
$\mathbf{d}^e, \mathbf{d}^p, \mathbf{d}^g$	Elastic, plastic and geometric part of the relative displacement, respectively
D_{nn} , D_{tt}	Elastic stiffness constants for the normal and shear displacements, respectively
d_o	Parameter related to the aggregate size
$\mathbf{F}$	Nodal force vector
F	Yield criterion
G_f^I , G_f^{II}	Fracture energies of mode I and mode II, respectively
H_i	Hermitian polynomial shape function
J	Jacobian
L	Length of the interface element
N_1, N_2	Linear shape functions
r, r_o, r_r	Current, initial and residual radius of curvature of the apex of the yield surface, respectively
s, s_o	Current and initial tensile strength, respectively
t	Thickness of the interface elements
$\mathbf{U}$	Nodal displacement vector
u_{ox}^b, u_{ox}^t	X-displacement along the mid line on bottom and top surface, respectively

u_{oy}^{b}, u_{oy}^{t}	Y- displacement along the mid line of the bottom and top surface, respectively
u_{oz}^{b}, u_{oz}^{t}	Z-displacement along the mid line on bottom and top surface, respectively
u_{x}^{b}, u_{x}^{t}	X- displacement of the bottom and top surface, respectively
u_{xi}	X-displacement of the ith node
u_{y}^{b}, u_{y}^{t}	Y- displacement of the bottom and top surface, respectively
u_{yi}	Y-displacement of the ith node
u_{z}^{b}, u_{z}^{t}	Z-displacement of the bottom and top surface, respectively
α, β	Parameters governing the rate of change of μ and r
$\delta\mathbf{d}$	Virtual relative displacement vector
$\delta\mathbf{U}$	Virtual nodal displacement vector
$\Delta u_x, \Delta u_y, \Delta u_z$	Relative displacements in x-, y- and z-directions, respectively
$\delta W_I, \delta W_E$	Internal and external virtual work, respectively
$\zeta_{dil}, \zeta_{dil,o}, \zeta_{dil,r}$	Current, initial and residual dilatation coefficient, respectively
$\theta_{ox}^{b}, \theta_{ox}^{t}$	X-rotation along the mid line on bottom and top surface, respectively
θ_{xi}	X-rotation of the ith node
θ_{zi}	Z-rotation of the ith node
μ , μ_o, μ_r	Current, initial and residual friction coefficient, respectively

$\boldsymbol{\sigma}$	Generalized stress vector
σ_z	Component of the stress vector normal to the surface
τ_x , τ_y	Components of the stress vector parallel to the surface

Section 2.6

d_b	Steel bar diameter
E_c	Young's modulus of the concrete
F_d	Dowel force
F_{tr}	Force when a reversal point is registered
$\mathbf{F}_x$, $\mathbf{F}_y$	Vector of nodal forces for x- and y- direction, respectively
F_y	Dowel capacity
f_c'	Concrete compressive strength
f_y	Steel yield strength
$F_{rp,}$ F_{rn}	Force of the maximum and minimum reversal points, respectively
$F_{tp,}F_{tn}$	Force of the target point in the positive and negative direction, respectively
F_t	Force of a target point
f_{cb}	Concrete bearing strength
G_1, G_2	Gauss points
J	Jacobian
I_s	Moment of inertia of the steel bar

K_t	Tangent stiffness at the target point
K_d	Initial stiffness of the dowel law
K_u	Unloading stiffness for the dowel law
L_{12}	Length of the steel side
L_{34}	Length of the concrete side
M_{pl}	Plastic moment of the reinforcing bar
$N_1,\ N_2$	Linear shape functions
s_{peak}	Slip at which the peak strength is attained
s_R	Clear spacing between the bar ribs
t_r	Displacement when a reversal point is registered
$t_{rp},\ t_{rn}$	Displacement of the maximum and minimum reversal points, respectively
$t_{tp},\ t_{tn}$	Displacement of the target point in the positive and negative direction, respectively
t_t	Displacement of a target point
v_i	Displacement of the i^{th} node in the y-directions
$\tilde{v}$	Normal relative displacement
$v_c,\ v_s$	Displacement in the y-direction for the concrete and steel side, respectively
v_i	Y-displacement of the i^{th} node
$\tilde{u}$	Tangential relative displacement

u_i	Displacement of the ith node in the x-directions
u_c , u_s	Displacement in the x-direction for the concrete and steel side, respectively
u_i	X-displacement of the ith node
δW_I , δW_E	Internal and external virtual work, respectively
$\delta\tilde{u}$, $\delta\tilde{v}$	Virtual displacements along the element for x- and y- direction, respectively
$\delta\mathbf{u}$, $\delta\mathbf{v}$	Vector of virtual nodal displacements for x- and y- direction, respectively
η , η_c	Natural coordinate system for the steel and concrete side, respectively
$\rho_{b,y}$, $\rho_{f,y}$	Reduction factor of the bearing and friction capacity due to tensile yielding, respectively
$\rho_{b,c}$, $\rho_{f,c}$	Reduction factor of the bearing and friction capacity due to cyclic slip reversals, respectively
σ	Dowel stress
τ	Bond stress
τ_b	Bond strength due to bearing forces
$\tau_{\max}$	Peak bond strength
τ_f	Bond strength due to friction forces

Chapter 3

d_b	Steel bar diameter
f_c'	Concrete compressive strength
f_y	Steel yield strength
F_y	Dowel capacity
s_o	Initial tensile strength
r_o, r_r	Initial and residual radius of curvature of the apex of the yield surface, respectively
f_o	Initial yield stress
f_t	Tensile strength of masonry
$\zeta_{dil,o}, \zeta_{dil,r}$	Initial and residual dilatation coefficient, respectively
μ_o, μ_r	Initial and residual friction coefficient, respectively
f_{sh}'	Stress at the onset of strain hardening for the steel material law
$f_{sh,1}'$	Stress of a point lying on the hardening regime for the steel material law
E_s	Initial elastic modulus of steel
E_c	Young's modulus of concrete
G_f^I, G_f^{II}	Fracture energies of mode I and mode II, respectively
ε_u	Ultimate strain for the orthotropic law
ε_1	Strain at which maximum compressive strength is attained for the

	orthotropic law
f'_u	Ultimate stress
ε'_{sh}	Strain at the onset of strain hardening
$\varepsilon'_{sh,1}$	Strain of a point lying on the hardening regime

Chapter 3

S_{DS}	Spectral acceleration at short period
S_{D1}	Spectral acceleration at 1-sec period
ε_y	Yield strain
ε_{sh}	Strain at initiation of strain hardening
ε_{su}	Strain at bar fracture

Chapter 6

d_b	Steel bar diameter
f'_c	Concrete compressive strength
f_y	Steel yield strength
F_y	Dowel capacity
s_o	Initial tensile strength
r_o, r_r	Initial and residual radius of curvature of the apex of the yield surface, respectively

f_o	Initial yield stress
f_t	Tensile strength of masonry
$\zeta_{dil,o}, \zeta_{dil,r}$	Initial and residual dilatation coefficient, respectively
μ_o, μ_r	Initial and residual friction coefficient, respectively
f'_{sh}	Stress at the onset of strain hardening for the steel material law
$f'_{sh,1}$	Stress of a point lying on the hardening regime for the steel material law
E_s	Initial elastic modulus of steel
E_c	Young's modulus of concrete
G_f^I , G_f^{II}	Fracture energies of mode I and mode II, respectively
ε_u	Ultimate strain for the orthotropic law
ε_1	Strain at which maximum compressive strength is attained for the orthotropic law
f'_u	Ultimate stress
ε'_{sh}	Strain at the onset of strain hardening
$\varepsilon'_{sh,1}$	Strain of a point lying on the hardening regime

LIST OF FIGURES

LIST OF TABLES

ACKNOWLEDGMENTS

The research presented in this dissertation was conducted under the supervision of Professor P. Benson Shing at the University of California at San Diego (UC San Diego). It was supported by a NIST ARRA Measurement Science and Engineering Grant awarded to the University of California at San Diego under Award No. 60NANB10D013. The shake-table tests were conducted with the support of the Network for Earthquake Engineering Simulation Program of NSF. I would also like to acknowledge a Graduate Fellowship from UC San Diego, which partially supported his graduate studies.

The experimental work presented in this dissertation was conducted in the Englekirk Structural Engineering Center of the University of California, San Diego. I am grateful to all the personnel in the laboratories for their cooperation and valuable help.

I would like to thank the members of my committee, Professors Y. Bazilevs, F. Lanza Di Scalea, J. Restrepo and J. C. del Alamo for their feedback on my dissertation and for offering classes which have been invaluable to my research.

I would also like to thank Professor Charis Gantes from the National Technical University of Athens (NTUA) for supervising my undergraduate thesis and encouraging me to apply for a graduate degree at UC San Diego.

I am most grateful to Professor Richard Klingner, Professor David McLean, Professor Andreas Stavridis, and Dr. Farhad Ahmadi for helping in the design of the two full scale shake-table tests. I would also like to thank Andreas for his help during the construction and instrumentation of the three-story specimen.

I would like to thank deeply Professor Ioannis Koutromanos, Dr. Juan Murcia-Delso and Ms Alexandra Kottari for providing their finite element programming codes of

their material laws, which are used in this study. I want to thank my colleagues Mr. Vasileios Papadolopoulos and Mr. Andreas Koutras who I have work with at different times and situations during my studies at UC San Diego and NTUA.

I want to express my sincere gratitude to my advisor, Professor P. Benson Shing, for his invaluable help, guidance, and patience throughout all these years. His advice on both research as well as on my career have been invaluable. Finally, I wish to thank my parents, Charalambos and Androula, and my siblings, Ioanna and Theano, for their support throughout the duration of my undergraduate and graduate studies in Athens and San Diego.

Chapter 1 and Chapter 4, in part, is a reprint of material as it appears in Mavros, M., Ahmadi, F., Shing, P.B., Klingner, R., McLean, D., and Stavridis. A., "Shake-table Tests of a Full-scale Two-story Shear-dominated Reinforced Masonry Wall Structure," ASCE Journal of Structural Engineering (under review). The dissertation author was the primary investigator and author of this paper.

VITA

2010 Diploma in Civil Engineering, National Technical University of Athens

2012 Master of Science in Structural Engineering, University of California, San Diego

2015 Doctor of Philosophy in Structural Engineering, University of California, San Diego

ABSTRACT OF THE DISSERTATION

Experimental and Numerical Investigation of the Seismic Performance of Reinforced Masonry Structures

by

Marios Mavros

Doctor of Philosophy in Structrual Engineering

University of California, San Diego, 2015

Professor P. Benson Shing, Chair

This study is to acquire a better understanding of the seismic performance of reinforced masonry structures at the system level, and develop reliable computational models that can predict the performance of these structures. To this end, a nonlinear finite

element modeling scheme has been developed and a two-story reinforced masonry shear wall structure was tested on a shake-table. This structure had door and window openings and wall components with low aspect ratios. A displacement-based method was used to design the two-story structure taking into account the shear-critical wall components. The structure behaved as expected under the design earthquake, but the drift levels exceeded the design limit considerably for the maximum considered earthquake. The experimental results reveal the significant contribution of the out-of-plane walls to the behavior of the structure and they have been used to validate the computational models developed in the study.

Nonlinear finite element models can be useful tools for assessing the performance of existing reinforced masonry structures, and for conducting parametric studies to evaluate different design methodologies and reinforcing details. A major challenge is to simulate the behavior of a reinforced masonry structural system with wall components that can be dominated by diagonal shear cracks or shear sliding. A general finite element modeling scheme that can predict the aforementioned failure mechanisms has been developed in this research. In this scheme, masonry is modeled with shell elements. A phenomenological law for simulating the dowel action of reinforcing bars has been proposed and implemented in a newly developed interface element that allows different mesh refinements for reinforcing bars and shell elements. An existing cohesive crack line interface model has been extended to account for the three-dimensional kinematic fields compatible with shell elements. The capability of the models to capture the response of the two-story structure has been demonstrated. Results from numerical studies have been used to validate the displacement-based design methodology and to quantify the

contribution of the out-of-plane walls to the lateral load resistance of the two-story structure.

1. INTRODUCTION

1.1. Background

Masonry has been commonly used worldwide for many years for the construction of buildings due to its beneficial features, like the fire protection, the sound and thermal insulation, the durability and its aesthetic characteristics. Masonry structures can be classified into two categories: reinforced and unreinforced. Unreinforced masonry structures provide low levels of ductility and thus they are not allowed to be constructed in earthquake prone regions in the U.S. In reinforced masonry structures, steel bars can be combined with masonry to enhance the seismic performance and to increase the strength and ductility capacity of these structures. The main lateral load resisting system of a reinforced masonry structure consists of reinforced masonry walls. Usually, the geometry of the walls is defined by the architectural design. With the given wall configuration, the design engineer has to determine the reinforcing details to provide the adequate strength and ductility according to the governing design codes.

Current design methods and code requirements in the U.S. for reinforced masonry structures are based on the consideration of forces. In force-based design according to ASCE 7 (ASCE 2010), a structure is assigned a Seismic Design Category (SDC) based on the design spectral intensity and the Risk Category of the building. For SDC D or above, special reinforced masonry shear walls are required for masonry structures. Special reinforced masonry load-bearing wall systems are permitted to have a response modification coefficient R equal to 5, which is based on the expectation that such wall systems are able to develop a ductile flexure-dominated behavior. As such, special

reinforced masonry walls are required to meet stringent reinforcing and detailing requirements in the MSJC Code (MSJC 2013), which include shear capacity design and overlaying prescriptive requirements such as the maximum spacing of the vertical and horizontal reinforcing bars. While these provisions can generally provide satisfactory designs, the approach is not entirely rational. In particular, these provisions neither effectively prohibit brittle shear-dominated wall behavior that is intrinsic to wall components with low aspect ratios nor impose more stringent lateral displacement limits to account for the reduced ductility capacities of these components. While the prescriptive reinforcing requirements provide additional safeguard against catastrophic failures for these structures, they can be excessive for many low-rise reinforced masonry structures that have long wall systems subjected to very low seismic demand.

To address the aforementioned issues, a Limit Design Method has been introduced in Appendix C in the 2013 edition of the MSJC Code (MSJC 2013) for the design of special walls. This alternative seismic design method permits the designer to identify the controlling yield mechanism of the wall system, and determine the base-shear strength, drift limit, and reinforcement quantity for each wall component based on its anticipated yield mechanism. Shear-dominated wall components are subject to more stringent drift limits and reinforcement requirements, and are assigned more conservative base-shear strengths than flexure-dominated walls. This can be considered as an intermediate step towards the displacement-based design approach proposed by Priestley et al. (2007).

However the design codes for reinforced masonry are based on very limited experimental data and on numerical analyses using simplified models that cannot capture

the shear and sliding behavior of the reinforce masonry wall components. Experimental studies have to be conducted to provide the much-needed experimental data that can be used to improve the design codes. Nevertheless, experiments are usually expensive, time consuming, they need special equipment and they have certain size limitations. Furthermore, during an experiment specific quantities in predefined locations can be recorded. For that reason, numerical tools that can predict the behavior of reinforced masonry structures in a realistic manner are highly desirable.

1.2. Overall project objectives and thesis scopes

The study presented in this dissertation is part of a bigger project funded by the National Institute for Standards and Technology. The project is a joint effort between researchers from the University of California at San Diego, the University of Texas at Austin, and Washington State University. The main objectives of this project are to develop and validate an innovative displacement-based method to design reinforced masonry structures, to provide the much-needed experimental data from quasi-static tests and dynamic tests and to develop nonlinear finite element models that can predict the behavior of these structures.

Simple in-plane walls were constructed and tested quasi-statically by the research teams of the University of Texas at Austin and the Washington State University and they are described by Sherman (2011), Ahmadi (2012), Kapoi (2012) and Cyrier (2012). These tests include walls with different aspect ratios, axial load ratios, boundary conditions, splice lengths, and reinforcement ratios. Two dynamic tests were performed at the shake-table facilities of the University of California at San Diego. The first

structure tested on the shake-table, was a full-scale, three-story reinforced masonry shear wall structure that it designed with the force-based methodology (Ahmadi et al. 2013a, Stavridis et al., 2015) while the second structure was a two-story structure that it was designed with a displacement-based approach proposed by Ahmadi et al. (2013a, 2013b).

This dissertation presents the experimental procedure and the major findings from the second shake-table experiment. The two-story structure had door and window openings. The wall components adjacent to the window had a small clear height and were shear-dominated. The structure was subjected to a series of dynamic tests with a historical ground motion record scaled to intensity levels up to that of the maximum considered earthquake (MCE). The test results have been analyzed to provide insight on the seismic performance of the structural system.

The experimental data have been used for the calibration and validation of the numerical tools. To this end, shell elements with a smeared crack law are combined with discrete cohesive interface to capture the inelastic behavior of masonry. The previously developed 2D discrete cohesive interface element has been modified to be used for three dimensional analyses using shell elements. A new interface formulation with a phenomenological dowel action law has been developed and implemented to capture the dowel action, which is important to consider for shear and sliding dominated walls. After the calibration and the validation of the finite element models, numerical analyses have been conducted to provide a better understanding on the behavior of reinforced masonry structures.

1.3. Dissertation outline

Chapter 2 presents a literature survey of past studies pertaining to the modeling of reinforced masonry structures. The description of the modeling methodology, the constitutive laws and element formulations developed and used in this study are also presented in this chapter.

In **Chapter 3,** experimental data of walls tested under quasi-static loadings are used to validate the proposed modeling methodology. Walls that experienced different failure mechanisms have been selected for this purpose.

Chapter 4 presents a literature review of the previous experimental research pertaining to reinforced masonry structures tested under dynamic or quasi-static loads. Furthermore, the construction, the instrumentation and the shake-table testing of a two-story reinforced are presented. The experimental data have been analyzed and presented to provide a good understanding of the behavior of the structure.

In **Chapter 5** the nonlinear finite element analysis of the two-story structure tested on the shake-table, which has been conducted to validate the modeling method and provided a better understanding of the behavior of the structure is presented. Moreover, a series of analyses have been conducted to examine the performance of the structure and validate the displacement-based design method.

Chapter 1, in part, is a reprint of material as it appears in Mavros, M., Ahmadi, F., Shing, P.B., Klingner, R., McLean, D., and Stavridis. A., “Shake-table Tests of a Full-scale Two-story Shear-dominated Reinforced Masonry Wall Structure,” ASCE Journal of

Structural Engineering (under review). The dissertation author was the primary investigator and author of this paper.

2. FINITE ELEMENT MODELING

In this chapter, modeling methods developed in previous research studies that can be used to analyze reinforced masonry (RM) and reinforced concrete (RC) structures are summarized. Furthermore, the finite element modeling scheme and computational models that have been developed in the current study to simulate the nonlinear behavior of RM and RC structures are presented. The modeling scheme adopts the smeared-crack and the discrete-crack approaches, with constitutive models implemented in shell and interface elements, to simulate the behavior of masonry and concrete. Reinforcing steel is modeled with truss elements with a uniaxial material law that describes the inelastic behavior of reinforcing steel under cyclic loading. A unique interface element with appropriate material laws has been developed to simulate the interaction of the reinforcing steel with the surrounding masonry or concrete, including the bond slip and dowel action. The novel contribution of the interface element formulation is that it enables the connection of steel and shell elements of different sizes. This feature allows a significant reduction of the number of shell elements required in an analysis and consequently the computational demand; and at the same time, it permits a sufficiently fine mesh to capture the bond slip and dowel action of reinforcing bars in an accurate manner. The element formulations and the material models are implemented in the finite element software FEAP (Taylor, 2014). The modeling scheme has been validated with experimental data from wall segments tested with quasi-static loads (presented in Chapter 3), and experimental data from shaking-table tests conducted on a full-scale RM wall structure (Chapter 5).

2.1. Available numerical tools – literature review

2.1.1. Beam models

The simplest way to model RC and RM structures is with beam elements which are aligned with the centroidal axis of different structural elements (beams, columns and walls) to simulate their behavior. Beam elements can be categorized into two separate classes: concentrated plasticity, in which the formation of the plastic hinges can happen only at the members' ends, and distributed plasticity, in which plasticity can be developed in a finite length hinge zone or anywhere along the length of the beam (fiber section beam elements). Clough et al. (1965), Gilberson (1967), Otani and Sozen (1972) and Saidi and Sozen (1979) used the concentrated plasticity approach to model multi-story, concrete frame buildings. They used plastic hinges that do not allow the moment to exceed a specific yield value or nonlinear spring hinges with a bilinear or trilinear bending-rotation law.

Later, other researchers (Takayanagi and Shnobrich, 1976, Aristizabal, 1983, Keshavarzian and Schnobrich, 1985, Saatcioglu et al., 1987, Roufaiel and Meyer, 1987, Satyarno et al., 1998) used the concentrated as well as the distributed plasticity approach, and by introducing several nonlinear springs, they tried to take into account effects like the axial force – moment interaction, inelastic shear deformation, pinching effect, strength degradation, spread of plasticity and the concrete-steel bond slippage. The assumption that the rotations occur along the centroidal axis without the capability of shifting the neutral axis and the assumption that all the plastic deformation is lumped at the end of the member are some of the limitations.

Mahin et al. (1975) developed a beam element using a fiber-section approach which is a type of distributed plasticity element. For this type of beam elements, the section is discretized in small areas (fibers), which are characterized by uniaxial laws of steel or concrete. The response of the section is derived by integrating the stresses in the fibers and, thus, these models inherently satisfy the moment-axial load interaction. The advantage of this method is that the analyst is more likely to know the material behavior than the moment-rotational relationships of the structural elements. Two main formulations of these elements are the force-based (Kaba and Mahin, 1984, Zeris and Mahin, 1991) and the displacement-based elements. Fiber-section elements use the Bernoulli's assumption that the plane sections remain plane, which is not necessarily true in cases of squat walls, and the assumption of perfect bond between steel and concrete; thus, the effects of bond-slip are neglected (Spacone et al., 1996). Furthermore, the numerical results are depend on the mesh size because of the localization issues these models have.

Although analysis with beam elements can simulate accurately and efficiently the behavior of flexural dominated members, they fail to predict the performance of members that are shear critical like squat walls.

2.1.2. Truss models

The truss analogy method is an alternative way to evaluate the linear and nonlinear behavior of RC or RM wall structures. Truss models are an efficient way to analyze these structures, as they use simple uniaxial constitutive laws employed to represent the behavior of the steel and the concrete. The behavior of wall structures was

simulated with truss models first by Ritter (1899) and Mörch (1902) (Bruggi, 2009). They used two parallel chords aligned with the longitudinal direction of the wall that were connected with diagonal and transverse members to represent the web. In this model, the diagonal members formed an angle of 45 degrees with the longitudinal direction assuming that the concrete cracks are formed in 45 degrees angle with respect to the reinforcement. The longitudinal and transverse members represented the concrete and the reinforcement while the diagonal members served as diagonal concrete compressive struts.

Hrennikoff (1941) used the framework method to model continuum elements by an elastic lattice. Later, Mazars et al. (2002) adopted Hrennikoff's method and simulated the dynamic and pseudodynamic tests of shear walls by using multi-cell truss configuration and nonlinear constitutive laws.

Experiments have shown that if the shear resistance is only taken into account by the diagonal struts that form 45 degrees with the longitudinal members, then the shear capacity is underestimated (Niwa et al. 1995). For this reason, Niwa et al. (1995) added arch members to contribute to the shear resistive mechanism and later Miki and Niwa (2004) extended this methodology for three dimensional lattices in order to simulate RC structural members under torsional and biaxial loads.

The modified compression field theory by Vecchio and Colins (1986) and the softened truss model by Hsu (1993) improved the truss modeling methodology. Later, Mansour and Hsu (2005) extended the rotating angle softened truss model theory (Hsu 1993) by introducing cyclic constitutive relationships. Panagiotou et al. (2012) refined their models by using more sophisticated material laws for modeling the behavior of

steel. Their concrete constitutive law takes into account the effect of the transverse strain, the stiffness and strength degradation. The transverse strain of the compression diagonal strut is registered by introducing a zero stiffness member that is connected to the other two nodes of the truss cell. Finally, Moharrami et al. (2014) modified the concrete equations to account for the aggregate interlock to the shear resistance and they proposed an equation to determine the inclination angle of the diagonal members.

Although truss element models can give good results for both flexural and shear dominated structural elements, they are inherently affected by the angle of the diagonal members. Since the analyst has the freedom to choose the angle of the diagonal members the procedure becomes less objective. Furthermore, truss element models can predict only the in-plane behavior and they neglect the out-of-plane contributions which makes the modeling procedure less appealing when three-dimensional effects are important.

2.2. Proposed modeling method and discretization scheme

The behavior of RM and RC structural systems under earthquake forces is complicated, rendering the evaluation of their seismic performance a challenging task. A good finite-element model of a 3-D RM or RC structure should be able to simulate diagonal shear cracking, flexural yielding, and shear sliding of wall components, which may have rectangular or flanged sections, as well as the bond-slip and dowel action behavior of reinforcing bars and the coupling effects of horizontal diaphragms. Mavros et al.(2015) demonstrated the importance of accounting for the 3-D behavior of wall systems in their study of a two-story RM wall structure tested on a shaking table.

Figure 2.1 shows the discretization scheme proposed in this study for RM or RC wall panels to capture all the main failure mechanisms. The physical model, shown in this figure, is a fully grouted masonry wall with vertical and horizontal reinforcement. A small portion of the wall is discretized, as shown in Figure 2.1. Smeared-crack shell elements are used to simulate the concrete compressive behavior, and cohesive discrete crack interface elements are used to represent the strongly localized tensile cracks. The cohesive interfaces can remove the undesired mesh-size sensitivity effect (Bazant and Oh., 1983) and the stress-locking effect (Rots and Blaauwendraad, 1989 and Lotfi and Shing., 1991), which could otherwise be introduced by the smeared-crack elements. The latter effect can lead to an overestimation of the shear strength and ductility of the wall components. In Figure 2.2, all the interface elements shown are expanded for clarity. Nodes 1 through 16 define the geometry of the smeared- and discrete crack elements. The cohesive interface elements are placed at 45^o and 135^o to capture the possible diagonal shear cracks.

Reinforcing steel is modeled with truss elements that are connected to the smeared-crack shell elements through the bond-slip and dowel action interface elements. The reinforcing steel elements shown in Figure 2.2 are defined by nodes 17 through 20. In general, the modeling of the bond-slip behavior and dowel action requires a relatively fine discretization for the reinforcing bars to capture the rapid variation of interaction stresses generated along the bar by these mechanisms, while the size of the smeared-crack elements needed to capture the fracture and compressive failure of masonry can be larger. To allow different element sizes for the reinforcing steel and the masonry elements, a special interface element is developed.

The rest of the wall can be discretized with repeated modules of elements as described above and each module is connected to the adjacent elements with vertical and horizontal discrete cohesive elements. The latter simulate the horizontal cracks that are developed due to flexural or sliding failure.

2.3. Truss elements

The reinforcing bars in RM and RC structures are of great importance as they can significantly affect the performance of these structures, and their behavior needs to be described accurately. The most appropriate element that can simulate both the axial and bending behavior of a reinforcing bar is a fiber-section beam element. For each fiber, a nonlinear uniaxial stress-strain law that describes the steel behavior can be used. Truss elements have a single fiber in contrast to the beam elements that should have several fibers to capture the bar bending behavior. Hence, truss elements are not as computationally demanding as beam elements, and they are preferred when the leading failure mechanism of a structural system is not greatly affected by the bending behavior of the reinforcing bar.

2.3.1. Steel material constitutive law

The uniaxial constitutive model developed by Kim (2015) based on the work of Dodd and Restrepo (1995) is used to represent the behavior of the steel reinforcement. This model has the salient features of the stress-strain relation of a reinforcing bar, including a yield plateau and subsequent strain hardening for initial monotonic loading, and the Bauschinger effect and kinematic hardening for cyclic loading.

The material model is formulated in the natural system, consisting of the true stress, f', and the natural strain, ε'. This has the advantage that a unique monotonic stress - strain curve can be implemented for both tension and compression. The monotonic envelope is described in the natural system by the following set of functions.

$$f' = \begin{cases} E_s \cdot \varepsilon' & \varepsilon' < \varepsilon'_y \\ s \cdot f_y \cdot e^{\varepsilon'} & \varepsilon'_y < \varepsilon' < \varepsilon'_{sh} \\ s\left(f'_y + f'_u(\varepsilon'_u - \varepsilon'_{sh}\right) - f'_u)\left(\dfrac{\varepsilon'_u - s(\varepsilon' - \varepsilon'_o(k))}{\varepsilon'_u - \varepsilon'_{sh}}\right)^P & \varepsilon'_{sh} < \varepsilon' < \varepsilon'_u \\ -f'_u\left(s \cdot \varepsilon'_u - (\varepsilon' - \varepsilon'_o(k)) - f'_u\right) + s \cdot f'_u & \\ s \cdot f'_u & \varepsilon' > \varepsilon'_u \end{cases} \tag{2.1}$$

in which E_s is the initial elastic modulus, f_y and f'_y are the yield stresses in engineering and natural system, respectively, ε'_y is the yield strain, ε'_{sh} is the strain at the onset of strain hardening, ε'_u is the ultimate strain, f'_u is the ultimate stress, *s*=1 for positive strain increment and *s*=-1 for negative strain increment. The parameter $\varepsilon'_o(k)$ is the shifted origin of the monotonic curve in case of cyclic loading, and its calculation will be discussed later. The exponent *P* that characterizes the hardening regime of the monotonic envelope is given by

$$P = \frac{\log\left(\dfrac{f'_{sh,1} + f'_u \cdot (\varepsilon'_u - \varepsilon'_{sh,1}) - f'_u}{f'_{sh} + f'_u \cdot (\varepsilon'_u - \varepsilon'_{sh}) - f'}\right)}{\log\left(\dfrac{\varepsilon'_u - \varepsilon'_{sh,1}}{\varepsilon'_u - \varepsilon'_{sh}}\right)} \tag{2.2}$$

in which $f'_{sh,1}$ and $\varepsilon'_{sh,1}$ are the values of any point lying on the hardening curve. The engineering stress σ and strain ε can then be obtained from the true stress and the natural strain by the following equations

$$\varepsilon = e^{\varepsilon'} - 1 \tag{2.3}$$

$$\sigma = \frac{f'}{1+\varepsilon} \tag{2.4}$$

Figure 2.3 shows the monotonic stress-strain curve and the characteristic values of the Dodd-Restrepo steel model in the engineering coordinate system.

The cyclic response of the material is characterized by reversal branches that depend on reversal points. A reversal point is defined as the set of strain and stress values, (ε'_r, f'_r) when the strain increment is reversed. Based on the reversal points, the reversal branches can be classified into three categories namely major, minor and simple reversals. If the first reversal occurs at the yield plateau or at the strain hardening region then the reversal branch is treated as minor or major respectively. Further reversals are classified into the three aforementioned categories depending on whether they occur inside or outside a previous reversal branch. If the magnitude of the stress difference between two consecutive reversal points, $\Delta\sigma_r$, is less than $2f'_y$ then the new reversal branch occurs inside the previous reversal branch, otherwise, it occurs outside. If the new branch occurs outside the previous branch, then the new branch is always major. If a reversal branch lies inside a major branch, then it is treated as minor, and similarly if the

reversal branch lies inside a minor then it is treated as simple. An example of the classification of the reversal branches is depicted in Figure 2.4.

Each reversal branch is characterized by linear elastic and a curved region. The linear elastic region is defined by the reversal point, (ε'_r, f'_r), and the point (ε'_a, f'_a), as shown in Figure 2.5. The point (ε'_a, f'_a) can be calculated by the following expressions

$$f'_a = f'_r + s \cdot f'_y \tag{2.5}$$

$$\varepsilon'_\alpha = \varepsilon'_r + \frac{s \cdot f'_y}{E'_u} \tag{2.6}$$

in which E'_u is the unloading modulus which can be calculated by

$$E'_u = E'_s \left(0.82 + \frac{1}{5.55 + 1000\varepsilon'_M} \right) \tag{2.7}$$

where $\varepsilon'_{\mathrm{M}}$ is the maximum attained magnitude of strain.

Dodd and Restrepo (1995) have proposed an implicit function of the stress and strain to calculate the curved region that is defined by the point (ε'_a, f'_a) and the target point, (ε'_t, f'_t). The target point depends on the classification of the reversal branch and it can be calculated as

$$\left(\varepsilon_t', f_t'\right) = \begin{cases} \left(\varepsilon_r' + s(\varepsilon_o'(2) - \varepsilon_o'(1)) + \dfrac{2 f_y'}{E_u'}, s \cdot f_y'\right) & \text{minor reversal branch starting from the yield platue} \\ \left(\varepsilon_{u,shift}', s \cdot f_u'\right) & \text{major reversal branch} \\ \left(\varepsilon_r', f_r'\right) \text{ of the previous major reversal branch} & \text{minor reversal branch} \\ \left(\varepsilon_r', f_r'\right) \text{of the previous major / minor reversal branch} & \text{simple reversal branch} \end{cases} \tag{2.8}$$

in which $\varepsilon_o'(1)$ and $\varepsilon_o'(2)$ are the shifted origins of the compression and tension monotonic curves, respectively, and $\varepsilon_{u,shift}'$ is the shifted ultimate strain (see Figure 2.5) that can be calculated by

$$\varepsilon_{u,shift}' = s \cdot \varepsilon_u' + \varepsilon_o'(k) \tag{2.9}$$

Kim (2015) replaced the implicit function that describes the hardening region by a quadratic non-uniform rational B-spline (NURBS) curve. Kim (2015) calibrated the parameters of the NURBS, so the new curves match the original hysteretic curves proposed by Dodd and Restrepo (1995). Furthermore, Kim (2015) proposed a methodology to account for the local buckling of the reinforcing bars phenomenologically. If buckling is detected, the obtained stress is multiplied by a reduction factor which is calculated based on the slenderness of the bar. More details for the steel constitutive laws, as well as the considerations for the local buckling can be found in Kim (2015) and Dodd and Restrepo (1995).

2.4. Shell elements

Shell elements are efficient for the analysis of 3-D wall structures, in which wall components can be oriented in different directions and can be subjected to in-plane, as well as, out-of-plane forces. The shell element formulation used here, which is described in detail in Burchnall (2014), is based on the discrete Kirchhoff theory and has multiple membrane layers across the thickness. The current element formulation used in this study has six layers across the thickness. At each layer, it is assumed a plane-stress condition. A smeared-crack model developed by Lotfi and Shing (1991) and improved by Koutromanos (2011, 2015) is adopted to represent the nonlinear stress-strain relation for each layer. The Lobatto quadrature method is employed to evaluate the through-thickness integrals to calculate the stress resultants.

2.4.1. Concrete and masonry material law

The behavior of the uncracked material in the shell layers is described by a plasticity model. As shown in Figure 2.6a, the failure surface for the plasticity model is a combination of the von Mises criterion given by

$$f = \sqrt{\sigma_1^2 - \sigma_1\sigma_2 + \sigma_2^2} - \sigma_e = 0 \tag{2.10}$$

and the tension cut-off criteria that are given by

$$f = \sigma_1 - f_t = 0 \tag{2.11}$$

$$f = \sigma_2 - f_t = 0 \tag{2.12}$$

where σ_1 and σ_2 are the principal stresses, f_t is the tensile strength, and σ_e is the effective stress. The effective stress describes the isotropic compressive strain hardening-softening behavior of the grouted masonry and is expressed with a parabolic function of the effective plastic strain, ε_p, followed by a linear softening tail (Figure 2.6b). After the ultimate strain ε_{up} is reached, the model maintains a constant residual concrete strength, $r_c f_c'$, to avoid possible convergences issues of the numerical analysis.

The effective stress is calculated as

$$\sigma_e = \begin{cases} f_o + (f_c' - f_o)\left(\dfrac{2\varepsilon_p}{\varepsilon_{1p}} - \dfrac{2\varepsilon_p^2}{\varepsilon_{1p}^2}\right) & \text{for } \varepsilon_p \le \varepsilon_{2p} \\ \sigma_{2p} + (r_c f_c' - \sigma_{2p})\left(\dfrac{\varepsilon_p - \varepsilon_{2p}}{\varepsilon_u - \varepsilon_{2p}}\right) & \text{for } \varepsilon_{2p} \le \varepsilon_p \le \varepsilon_{up} \\ r_c f_c' & \text{for } \varepsilon_p \ge \varepsilon_{up} \end{cases} \tag{2.13}$$

in which f_o and f_c' are the initial yield stress and the concrete compressive strength, ε_{1p} ε_{1p} is the plastic strain where the concrete strength is attained. The point (ε_{2p}, σ_{2p}) gives the plastic strain and the effective stress at which the concrete is crushed, and therefore the compressive strength is reduced linearly to a residual value.

When the maximum principal stress reaches the tension cutoff surface (Figure 2.6a), a crack is allowed to develop at each Gauss point, and its orientation remains fixed. Once the material has cracked, a nonlinear orthotropic material law is employed to describe the stress-strain relations in directions normal and parallel to the crack (Figure 2.6c). The monotonic uniaxial orthotropic law for both directions is expressed by

$$\sigma = \begin{cases} r_c f_c' & \varepsilon \le \varepsilon_u \\ \sigma_{2o} - \left(r_c f_c' + \sigma_{2o}\right)\left(\dfrac{\varepsilon - \varepsilon_2}{\varepsilon_u - \varepsilon_2}\right) & \varepsilon_u \le \varepsilon \le \varepsilon_2 \\ \left(f_c' - f_o\right)\left(\dfrac{\varepsilon - \varepsilon_1}{\varepsilon_1 - \varepsilon_e}\right)^2 - f_c' & \text{for } \varepsilon_2 \le \varepsilon \le \varepsilon_e \\ E_c \varepsilon & \text{for } \varepsilon_e \le \varepsilon \le \varepsilon_{cr} \\ f_t\left(r_t + \left(1 - r_t\right) e^{-\frac{m_t\left(\varepsilon - \varepsilon_{cr}\right)}{f_t\left(1 - r_t\right)}}\right) & \text{for } \varepsilon \ge \varepsilon_{cr} \end{cases} \tag{2.14}$$

in which $r_t f_t$ is the residual strength of the monotonic envelope for tension, ε_1 and ε_{cr} are the strains at which the maximum compressive and maximum tensile strength are attained respectively, ε_2 is the strain at which the linear degradation of the orthotropic law in compression begins, and E_c is the Young's modulus of concrete. The tensile shape factor, m_t, is adjusted with respect to the element size so that the area under the softening portion times the characteristic length, L_{ch}, is equal to the tensile fracture energy, G_{f1}, and can be calculated by

$$\begin{Bmatrix} \tilde{u} \\ \tilde{v} \end{Bmatrix} = \begin{Bmatrix} u_s(x) - u_c(x) \\ v_s(x) - v_c(x) \end{Bmatrix} \tag{2.15}$$

The strain levels ε_e and ε_{cr} are defined by

$$\begin{aligned} \varepsilon_e &= -\frac{f_o}{E_c} \\ \varepsilon_{cr} &= \frac{f_t}{E_c} \end{aligned} \tag{2.16}$$

The model allows a second crack to open, perpendicular to the first crack when the tensile strength in this direction reaches the tensile strength of the concrete. For the shear strain – stress law in the fixed crack coordinate system, the model uses an elastic-plastic law with shear strength being half of the tensile strength of the concrete.

The uniaxial cyclic behavior given by the smeared-crack model is depicted in Figure 2.7. The material model uses a secant stiffness rule for loading/unloading in the tensile regime and an initial stiffness rule for loading/unloading in the compressive regime. The two material laws are calibrated such that the same behavior for uniaxial compression is obtained.

2.5. 3D cohesive crack interface

Cohesive crack interface elements are used to model the localized crack behavior introduced by in- or out-of-plane stresses in wall components. An interface element formulated by Koutromanos (2015) in order to be used for analysis using shell elements, is implemented. The interface can describe the kinematic field of a three-dimensional crack, and is used to capture the behavior of reinforced concrete and masonry walls under multi-axial cyclic loading. The element combines a previously proposed cohesive traction-separation law, which can account for mixed-mode fracture, frictional sliding, irreversible compaction and reversible normal dilatation. Since the previously proposed model had been developed for two-dimensional problems, the constitutive law was modified by Kottari (2015) to account for the triaxial traction-separation behavior.

2.5.1. Element formulation

The interface element formulation developed in a 4-node element with two surfaces. As illustrated in Figure 2.8, the element is described by the local coordinate system, *x*-*y*-*z*, which can be transform to the natural coordinate system, (η, ξ), using the following transformation equations

$$\eta = \frac{2x}{L} - 1$$
$$\xi = \frac{2y}{t} \tag{2.17}$$

in which L and t are the length and width of the element, respectively.

Nodes 1 and 2 define the midline of the bottom surface and the nodes 3 and 4 define the midline of the top surface. The local *x*-direction is defined by the geometry of the element but the user has to input the *y*-direction with respect to the global coordinate system as a material parameter. Each nodal point has six degrees of freedom, i.e. three translations and three rotations in the local coordinate system.

Each surface has in- and out-of-plane displacements, as shown in Figure 2.9. The in-plane displacements due to bending (Figure 2.9a) and axial (Figure 2.9b) deformations, are obtained by using the kinematics of Euler-Bernoulli beam theory, assuming a uniform cross section beam. For all the points on the midline of the bottom surface, the in-plane displacements are given by

$$u_{ox}^{b}(\eta) = N_1(\eta)\cdot u_{x1} + N_2(\eta)\cdot u_{x2} \tag{2.18}$$

$$u_{oy}^{b}(\eta) = H_1(\eta)\cdot u_{y1} + H_2(\eta)\cdot \theta_{z1} + H_3(\eta)\cdot u_{y2} + H_4(\eta)\cdot \theta_{z2} \tag{2.19}$$

in which N_i's and H_i's are the linear and the Hermitian polynomial shape functions, respectively, and they are defined in the natural coordinate η as follows.

$$N_1(\eta) = \frac{1-\eta}{2} \tag{2.20}$$

$$N_2(\eta) = \frac{1+\eta}{2} \tag{2.21}$$

$$H_1 = \frac{1}{4}(1-\eta)^2(2+\eta) \tag{2.22}$$

$$H_2 = \frac{1}{4}(1-\eta)^2(\eta+1) \tag{2.23}$$

$$H_3 = \frac{1}{4}(1+\eta)^2(2+\eta) \tag{2.24}$$

$$H_4 = \frac{1}{4}(1+\eta)^2(\eta-1) \tag{2.25}$$

The in-plane displacements of any point with natural coordinates (η, ξ) are obtained as

$$u_x^b(\eta,\xi) = u_{ox}^b(\eta) - \frac{du_{oy}^b(\eta)}{d\eta}\xi \tag{2.26}$$

$$u_y^b(\eta,\xi) = u_{oy}^b(\eta) \tag{2.27}$$

Finally, the out-of-plane displacements (i.e. along the *z*-direction along the midline) and the rotation about the x-axis of the midline are given by

$$u_{oz}^b(\eta) = N_1(\eta)\cdot u_{z1} + N_2(\eta)\cdot u_{z2} \tag{2.28}$$

$$\theta_{ox}^{b}(\eta) = N_1(\eta)\cdot\theta_{x1} + N_2(\eta)\cdot\theta_{x2} \tag{2.29}$$

Combining Eqs 2.28 and 2.29, the *z*-displacement at any point with natural coordinates (η, ξ) can be obtained as

$$u_z^b(\eta,\xi) = u_{oz}^b(\eta) + \xi\cdot\theta_{ox}^b(\eta) \tag{2.30}$$

Similarly, the displacements field of the top surface can be calculated by

$$u_x^t(\eta,\xi) = u_{ox}^t(\eta) - \frac{du_{oy}^t(\eta)}{d\eta}\xi \tag{2.31}$$

$$u_y^t(\eta,\xi) = u_{oy}^t(\eta) \tag{2.32}$$

$$u_z^t(\eta,\xi) = u_{oz}^t(\eta) + \xi\cdot\theta_{ox}^t(\eta) \tag{2.33}$$

in which

$$u_{ox}^t(\eta) = N_1(\eta)\cdot u_{x4} + N_2(\eta)\cdot u_{x3} \tag{2.34}$$

$$u_{oy}^t(\eta) = H_1(\eta)\cdot u_{y4} + H_2(\eta)\cdot\theta_{z4} + H_3(\eta)\cdot u_{y3} + H_4(\eta)\cdot\theta_{z3} \tag{2.35}$$

$$u_{oz}^t(\eta) = N_1(\eta)\cdot u_{z4} + N_2(\eta)\cdot u_{z3} \tag{2.36}$$

$$\theta_{ox}^t(\eta) = N_1(\eta)\cdot\theta_{x4} + N_2(\eta)\cdot\theta_{x3} \tag{2.37}$$

The kinematic quantities that affect the resistance of the interface are the relative displacements of the two surfaces, i.e. the difference in the displacement vector of the bottom surface from the displacement vector of the top surface.

$$\mathbf{d}=\begin{Bmatrix}\Delta u_x\\ \Delta u_y\\ \Delta u_z\end{Bmatrix}=\begin{Bmatrix}u_x^t-u_x^b\\ u_y^t-u_y^b\\ u_z^t-u_z^b\end{Bmatrix}=\mathbf{B}(\eta,\xi)\cdot\mathbf{U} \tag{2.38}$$

with

$$\mathbf{B}(\eta,\xi)=\begin{bmatrix}\mathbf{B_1}(\eta,\xi) & \mathbf{B_2}(\eta,\xi) & \mathbf{B_3}(\eta,\xi) & \mathbf{B_4}(\eta,\xi)\end{bmatrix} \tag{2.39}$$

in which

$$\mathbf{B_1}(\eta,\xi)=\begin{bmatrix}-N_1 & \xi\dfrac{dH_1}{d\eta} & 0 & 0 & 0 & \xi\dfrac{dH_2}{d\eta}\\ 0 & -H_1 & 0 & 0 & 0 & -H_2\\ 0 & 0 & -N_1 & -\xi N_1 & 0 & 0\end{bmatrix} \tag{2.40}$$

$$\mathbf{B}_2(\eta,\xi)=\begin{bmatrix}-N_2 & \xi\dfrac{dH_3}{d\eta} & 0 & 0 & 0 & \xi\dfrac{dH_4}{d\eta}\\ 0 & -H_3 & 0 & 0 & 0 & -H_4\\ 0 & 0 & -N_2 & -\xi N_2 & 0 & 0\end{bmatrix} \tag{2.41}$$

$$\mathbf{B}_3(\eta,\xi)=\begin{bmatrix}N_2 & -\xi\dfrac{dH_3}{d\eta} & 0 & 0 & 0 & -\xi\dfrac{dH_4}{d\eta}\\ 0 & H_3 & 0 & 0 & 0 & H_4\\ 0 & 0 & N_2 & \xi N_2 & 0 & 0\end{bmatrix} \tag{2.42}$$

$$\mathbf{B}_4(\eta,\xi)=\begin{bmatrix}N_1 & -\xi\dfrac{dH_1}{d\eta} & 0 & 0 & 0 & -\xi\dfrac{dH_2}{d\eta}\\ 0 & H_1 & 0 & 0 & 0 & H_2\\ 0 & 0 & N_1 & \xi N_1 & 0 & 0\end{bmatrix} \tag{2.43}$$

and $\mathbf{U} = \begin{Bmatrix} \mathbf{U}_1 \\ \mathbf{U}_2 \\ \mathbf{U}_3 \\ \mathbf{U}_4 \end{Bmatrix}$, $\mathbf{U}_i = \begin{Bmatrix} u_{xi} \\ u_{yi} \\ u_{zi} \\ \theta_{xi} \\ \theta_{yi} \\ \theta_{zi} \end{Bmatrix}$

The relative displacement in the z-direction, Δu_z, is the normal component of the interface displacement vector, while the other two relative displacement components are the tangential components.

Given the values of the relative displacements, **d**, the generalized stress vector, **σ**, can be determined by a set of constitutive law which will be described briefly in the next section. The element nodal forces, **F**, can be formulated with the principle of virtual displacement, with the internal virtual work given by

$$\delta W_I = -\int_{-\frac{t}{2}}^{\frac{t}{2}} \left(\int_0^L \delta \mathbf{d} \cdot \boldsymbol{\sigma} dx \right) dy \tag{2.44}$$

and the external virtual work by

$$\delta W_E = \delta \mathbf{U}^T \mathbf{F} \tag{2.45}$$

in which $\delta \mathbf{d}$ is the virtual relative displacements vector along the surface of the element, $\delta \mathbf{U}$ is the vector of the virtual nodal displacements, and $\mathbf{F}$ is the vector of the element nodal forces. With Eqs. 2.44 and 2.45, and the condition that $\delta W_I + \delta W_E = 0$, we have

$$\mathbf{F} = \int_{-1}^{1} \int_{-1}^{1} \mathbf{B}(\eta, \xi) \boldsymbol{\sigma}(\eta, \xi) J d\eta d\xi \tag{2.46}$$

$$J = \frac{dx}{d\eta} \frac{dy}{d\xi} = \frac{L \cdot t}{4} \tag{2.47}$$

2.5.2. Discrete cohesive crack material law

The material law formulated by Kottari (2015) is implemented for the discrete cohesive crack interfaces. It is suitable for three-dimensional analysis, as it can account for shear loading in the two directions of a shear plane. This model is based on a previous formulation of Koutromanos and Shing (2011) that can simulate the reversible shear dilatation caused by a crack roughness, and crack opening and closing. The relative displacement vector, **d**, is decomposed into three parts, as proposed by Mehrabi and Shing (1997).

$$\mathbf{d} = \mathbf{d}^e + \mathbf{d}^p + \mathbf{d}^g = \begin{Bmatrix} \Delta u_x^e \\ \Delta u_y^e \\ \Delta u_z^e \end{Bmatrix} + \begin{Bmatrix} \Delta u_x^p \\ \Delta u_y^p \\ \Delta u_z^p \end{Bmatrix} + \begin{Bmatrix} 0 \\ 0 \\ \Delta u_z^g \end{Bmatrix} \tag{2.48}$$

where d^e is the elastic part, d^p is the plastic part and d^g is the geometric part of the relative displacement vector. The geometric part consists of only a geometric normal component to account for the reversible dilatation.

The yield criterion considered is the following.

$$F = \tau_x^2 + \tau_y^2 - \mu^2 \left(\sigma_z - s\right) - 2r\left(\sigma_z - s\right) = 0 \tag{2.49}$$

in which τ_x, τ_y and σ_z are the components of the stress vector **σ**, μ is the friction coefficient, *r* is the radius of curvature at the apex of the yield surface, and *s* is the tensile strength, as shown in Figure 2.10. The values of these parameters are expected to decrease from their initial values (μ_o, r_o and s_o) to their residual values (μ_r, r_r and s_r). Their softening behavior is described by the following set of equations.

$$s = s_o\left(1-\frac{\kappa_1}{G_f^I}-\frac{\kappa_2}{G_f^{II}}\right) \tag{2.50}$$

$$r = \left(r_o - r_r\right)e^{-\beta\kappa_3} + r_r \tag{2.51}$$

$$\mu = \left(\mu_o - \mu_r\right)e^{-\alpha\kappa_3} + \mu_r \tag{2.52}$$

In Eq. 2.50 through 2.52, G_f^I and G_f^{II} are the energies of mode I and mode II fracture, respectively, α and β are parameters governing the rate of change of μ and r, and κ_1, κ_2 and κ_3 are associated with the plastic work of mode I and mode II fractures. A detailed explanation can be found in Kottari (2015).

Finally, the dilatation of the sliding surface is accounted for in the following manner.

$$\dot{\Delta}u_z^g = \zeta_{dil}\dot{\Delta}_{res}^p \tag{2.53}$$

in which $\dot{\Delta}u_z^g$ is the rate of the geometric part of the relative displacement vector, ζ_{dil} is the dilatation coefficient, and $\dot{\Delta}_{res}^p$ is the rate of the resultant plastic displacement in the shear plane given by

$$\Delta_{res}^p = \sqrt{\left(\Delta u_x^p\right)^2 + \left(\Delta u_y^p\right)^2} \tag{2.54}$$

Following the work of Koutromanos and Shing (2011), Kottari (2015) suggested the following formula for the degradation of the dilatation parameter, to account for the smoothing of a sliding surface

$$\zeta_{dil} = \left(\zeta_{dil,o} - \zeta_{dil,r}\right) e^{\left(-\frac{\left|\Delta_{res}^{p}\right|}{d_o}\right)} + \zeta_{dil,r} \tag{2.55}$$

in which $\zeta_{dil,o}$ and $\zeta_{dil,o}$ are the initial and final values of the dilatation coefficient, and d_o is a parameter related to the aggregate size. Values for the calibration of this parameter are given from Koutromanos and Shing (2011).

From the relative displacements, the normal and shear stresses are calculated as follows, from work of Koutromanos and Shing (2011):

$$\sigma_z = -D_{nn}\left\langle d_{n1} - \Delta u_z \right\rangle + D_{nn}\left\langle \Delta u_z - d_{n2} \right\rangle \tag{2.56}$$

$$\tau_x = D_{tt}\left(\Delta u_x - \Delta u_x^P\right) \tag{2.57}$$

$$\tau_y = D_{tt}\left(\Delta u_y - \Delta u_y^P\right) \tag{2.58}$$

in which D_{nn} and D_{tt} are the elastic stiffness constants for the normal and shear displacements. In Eq. 2.56 variables d_{n1} and d_{n2}, that are schematically depicted in Figure 2.11, have been used by Koutromanos and Shing (2011) to effectively simulate the crack closing and re-opening behavior and can be calculated by:

$$\dot{d}_{n1} = -\left\langle -\dot{\Delta} u_z^p \right\rangle + \dot{\Delta} u_z^g \tag{2.59}$$

$$\dot{d}_{n2} = \dot{\Delta} u_z^p \tag{2.60}$$

2.6. Interface element for bond-slip and dowel action

In this section, an interface element formulation to model the dowel action and bond-slip behavior of the steel reinforcement is presented. The interface connects steel to concrete, and the formulation allows the steel elements to have smaller size than the concrete elements. It adopts a bond stress-vs.-slip law previously developed by Murcia-Delso and Shing (2014) and a phenomenological model has been developed to account for the cyclic behavior of the dowel action.

2.6.1. Element formulation

To study the phenomena of bond slip and dowel action, reinforcing bars normally require a relatively fine mesh to accurately capture the variation of the shear and normal stresses along the steel-concrete interface, as compared to the size of concrete elements needed to simulate the nonlinear behavior of an RC member in an accurate manner. Figure 2.12 illustrates the meshing scheme proposed here to address the need to have different element sizes for concrete and the steel reinforcement. Figure 2.12c shows an example in which four bar elements are to be connected to a single concrete element. For this type of meshing, a 4-node zero-thickness interface element formulation is presented here. As illustrated in Figure 2.13, each steel element in Figure 2.12c is connected to the concrete element with one interface element.

Figure 2.14 shows an isolated interface element with Gauss points G_1 and G_2. Nodes 3 and 4 are connected to the concrete element, while nodes 1 and 2 to the steel element. It is so configured that the length of the steel element (L_{12}) has to be equal to or

shorter than that of the concrete element (L_{34}) and that the steel element has to be between nodes 3 and 4 in its undeformed state.

Each node i of the interface element has two degrees of freedom, i.e., displacements in the x and y directions, denoted by u_i and v_i, respectively. The shear (bond) stress τ and the normal (dowel) stress σ along the element depend on the values and histories of the relative tangential (slip) displacement $\tilde{u}$ and relative normal displacement $\tilde{v}$, which are defined as

$$\begin{Bmatrix} \tilde{u} \\ \tilde{v} \end{Bmatrix} = \begin{Bmatrix} u_s(x) - u_c(x) \\ v_s(x) - v_c(x) \end{Bmatrix} \tag{2.61}$$

in which u_c, u_s, v_c, and v_s are displacements in the x and y directions along the concrete side and the steel side of the element. They are determined by displacement shape functions and the nodal displacements. To calculate the relative displacements, the steel side (1-2) and the concrete side (3-4) have individual natural coordinate systems η and η_c, respectively, which satisfy the following linear relation.

$$\eta_c = \alpha + \beta\eta \tag{2.62}$$

where

$$\alpha = \frac{L_{14} - L_{23}}{L_{34}} \tag{2.63}$$

$$\beta = \frac{L_{12}}{L_{34}} \tag{2.64}$$

The displacements of any point along the steel side are given by

$$u_s(\eta) = N_1(\eta) \cdot u_1 + N_2(\eta) \cdot u_2 \tag{2.65}$$

$$v_s(\eta) = N_1(\eta) \cdot v_1 + N_2(\eta) \cdot v_2 \tag{2.66}$$

in which N_i's are linear shape functions defined in the natural coordinate η as follows.

$$N_1(\eta) = \frac{1-\eta}{2} \tag{2.67}$$

$$N_2(\eta) = \frac{1+\eta}{2} \tag{2.68}$$

The displacements along the concrete side are defined in the same way as follows.

$$u_c(\eta_c) = N_1(\eta_c) \cdot u_4 + N_2(\eta_c) \cdot u_3 \tag{2.69}$$

$$v_c(\eta_c) = N_1(\eta_c) \cdot v_4 + N_2(\eta_c) \cdot v_3 \tag{2.70}$$

Based on the relation in Eq. 2.62, the relative displacements along the interface can be expressed as functions of η.

$$\begin{Bmatrix} \tilde{u} \\ \tilde{v} \end{Bmatrix} = \begin{Bmatrix} u_s(\eta) - u_c(\alpha + \beta\eta) \\ v_s(\eta) - v_c(\alpha + \beta\eta) \end{Bmatrix} = \begin{bmatrix} \mathbf{b}(\eta) & \mathbf{0} \\ \mathbf{0} & \mathbf{b}(\eta) \end{bmatrix} \cdot \begin{Bmatrix} \mathbf{u} \\ \mathbf{v} \end{Bmatrix} \tag{2.71}$$

where

$$\mathbf{b}(\eta) = \begin{bmatrix} N_1(\eta) & N_2(\eta) & -N_2(\alpha + \beta\eta) & -N_1(\alpha + \beta\eta) \end{bmatrix} \tag{2.72}$$

and

$$\begin{Bmatrix} \mathbf{u} \\ \mathbf{v} \end{Bmatrix} = \begin{Bmatrix} u_1 & u_2 & u_3 & u_4 & v_1 & v_2 & v_3 & v_4 \end{Bmatrix}^T \tag{2.73}$$

Given $\tilde{u}$ and $\tilde{v}$, the values of the shear and normal stresses, τ and σ, are determined by a set of constitutive laws. As will be described in the following two sections, the stress-strain relations in the normal and tangential directions are assumed to be independent for the sake of simplicity and numerical robustness. This would have the implication that the deterioration of the bond stress would not be affected by the damage of the concrete due to the dowel action mechanism. However, the damaged concrete due to the dowel action mechanism is limited to the vicinity of the sliding plane and it is not expected to affect significant the results in system level.

With the consideration that each concrete element is in contact with one or more steel elements, for each interface element, only the stresses along the length of the connected steel element (i.e., L_{12} as shown in Figure 2.14) are determined and used to calculate the element nodal forces. For a unit length of the steel bar with diameter d_b, the shear stress τ acts around the bar circumference, πd_b, while the normal stress σ is assumed to act on a rectangular area, d_b, which represents the projection of the contact surface between the bar and the concrete on the *x*-*z* plane. The element forces can be formulated with the principle of virtual displacements, with the internal virtual work given by

$$\delta W_I = -\pi d_b \int_0^{L_{12}} \delta\tilde{u} \cdot \tau dx - d_b \int_0^{L_{12}} \delta\tilde{v} \cdot \sigma dx \tag{2.74}$$

and the external virtual work by

$$\delta W_E = \delta \mathbf{u}^T \mathbf{F}_x + \delta \mathbf{v}^T \mathbf{F}_y \tag{2.75}$$

in which $\delta\tilde{u}$ and $\delta\tilde{v}$ are the virtual relative displacements along the element, $\delta\mathbf{u}$ and $\delta\mathbf{v}$ are the vectors of virtual nodal displacements, and $\mathbf{F}_x$ and $\mathbf{F}_y$ are vectors of element nodal forces in the x and y directions. With Eqs. 2.74, 2.75 and the condition that $\delta W_I + \delta W_E = 0$, we have

$$\begin{aligned} \mathbf{F}_x &= \pi d_b \int_{-1}^{1} \mathbf{b}^T(\eta)\tau(\eta) J d\eta \\ \mathbf{F}_y &= d_b \int_{-1}^{1} \mathbf{b}^T(\eta)\sigma(\eta) J d\eta \end{aligned} \tag{2.76}$$

where

$$J = \frac{dx}{d\eta} = \frac{L_{12}}{2} \tag{2.77}$$

2.6.2. Bond-slip material law

The bond-slip law proposed by Murcia-Delso and Shing (2014) has been adopted here to describe the stress-strain relation in the tangential direction of the interface element. However, its interaction with the normal direction is ignored here. The model accounts for the bond-strength degradation caused by bar slip, cyclic slip reversals, and the tensile yielding of a bar. It requires only three parameters, namely, the peak bond strength (τ_{max}), slip at which the peak strength is attained (s_{peak}), and the clear spacing between the bar ribs (s_R), to calibrate. In the model, the bond resistance is assumed to be provided by two mechanisms, the bearing forces on the bar ribs and the friction forces between the concrete and steel surfaces, as shown in Figure 2.15a for the monotonic shear stress-slip relation. The bond-slip law is given by

$$\tau = \rho_{b,y} \cdot \rho_{b,c} \cdot \tau_b + \rho_{f,y} \cdot \rho_{f,c} \cdot \tau_f \tag{2.78}$$

where

$$\tau_b(\tilde{u}) = \begin{cases} 3.0\dfrac{\tau_{\max}}{s_{peak}}\tilde{u} & \text{for } 0 \le |\tilde{u}| < 0.1s_{peak} \\ sign(s)\cdot\tau_{\max}\left[0.75 - 0.45\left(\dfrac{|\tilde{u}| - s_{peak}}{0.9s_{peak}}\right)^4\right] & \text{for } 0.1s_{peak} \le |\tilde{u}| < s_{peak} \\ sign(\tilde{u})\cdot 0.75\tau_{\max} & \text{for } s_{peak} \le |\tilde{u}| < 1.1s_{peak} \\ sign(\tilde{u})\cdot 0.75\tau_{\max}\left[1 - \dfrac{|\tilde{u}| - 1.1s_{peak}}{s_R - 1.1s_{peak}}\right] & \text{for } 1.1s_{peak} \le |\tilde{u}| < s_R \\ 0 & \text{for } |\tilde{u}| \ge s_R \end{cases} \tag{2.79}$$

and

$$\tau_f(\tilde{u}) = \begin{cases} \dfrac{\tau_{\max}}{s_{peak}}\tilde{u} & \text{for } 0 \le |\tilde{u}| < 0.1s_{peak} \\ sign(\tilde{u})\cdot\tau_{\max}\left[0.25 - 0.15\left(\dfrac{\tilde{u} - s_{peak}}{0.9s_{peak}}\right)^4\right] & \text{for } 0.1s_{peak} \le |\tilde{u}| < s_{peak} \\ sign(\tilde{u})\cdot 0.25\tau_{\max} & \text{for } |\tilde{u}| \ge s_{peak} \end{cases} \tag{2.80}$$

in which τ_{max} and τ_{res} are the maximum and residual bond strengths for monotonic loading, $\rho_{b,s}$ and $\rho_{f,s}$ account for the reduction of the bearing and friction resistances due to the tensile yielding of the bar, and $\rho_{b,c}$ and $\rho_{f,c}$ account for the strength degradation due to cyclic slip reversals. Expressions for the strength reduction factors can be found in Murcia-Delso and Shing (2014). Moreover, Murcia-Delso and Shing (2014) proposed the following equations to estimate the values of the τ_{max}, s_{peak} and s_R

$$\tau_{\max} = 2.4\left(\frac{f_c'}{5.0}\right)^{0.75} \tag{2.81}$$

$$s_{peak} = 0.07 d_b \tag{2.82}$$

$$s_R = 0.5 d_b \tag{2.83}$$

in which d_b is the bar diameter (in.) and f_c' is the concrete compressive strength (ksi).

2.6.3. Dowel action material law

The force-displacement relation in the normal direction of the interface can be used to simulate the dowel action behavior. Dowel action is the capacity of a reinforcing bar to transfer shear forces parallel to a shear sliding crack when there is relative movement between the two sides of the crack. If the reinforcing bar is surrounded by sufficient concrete then the behavior of the dowel action mechanism for small deformations is governed by the bending capacity of the bar and the bearing strength of the concrete. For large deformation, the axial load of the reinforcing bar has a component parallel to the crack that can provide extra dowel capacity.

The proposed phenomenological dowel action law can describe the dowel action behavior only for small displacements. For the sake of computational efficiency, it is highly desirable to use truss elements instead of beam elements to represent the steel reinforcing bars. However, truss elements do not have any bending capacity hence; the dowel action law must take into account both the effect of the concrete strength and the bending capacity of the reinforcing bar. For that reason the material law that is discussed later must be only combined with truss elements as the reinforcing steel. Kottari (2015) developed a cyclic material law that represents only the concrete behavior in the vicinity

of the reinforcing bar and when it is combined with beam elements can predict accurately the dowel action behavior even for large deformations.

Previous studies (Paulay et al., 1974, Vintzeleou and Tassios, 1987, Dei Poli et al., 1992) examined the monotonic behavior of dowel action, which is schematically depicted in Figure 2.16. This behavior can be described with a modified version of the Menegotto and Pinto (1973) equation with zero hardening:

$$F_d = \frac{K_d \cdot \tilde{v}}{\left(1 + 30 \cdot \left(\frac{K_d \cdot \tilde{v}}{sF_y}\right) + \left(\frac{K_d \cdot \tilde{v}}{sF_y}\right)^3\right)^{\frac{1}{3}}} \tag{2.84}$$

in which F_y is the dowel capacity, K_d is the initial stiffness, s=1 for positive displacement increment and s=-1 for negative displacement increment. For the estimation of the dowel capacity (F_y) Eqs. 2.85 through 2.87, proposed by Kottari (2015), can be used

$$F_y = \sqrt{2M_{pl} d_b f_{cb}} \tag{2.85}$$

$$f_{cb} = \frac{\alpha}{d_b} f_c'^{1.2} \tag{2.86}$$

$$\alpha = 2 \cdot d_b + 0.5 \tag{2.87}$$

where f_{cb} is the concrete bearing strength and M_{pl} is the plastic moment of the reinforcing bar that can be calculated by

$$M_{pl} = \frac{f_y d_b^3}{6} \tag{2.88}$$

The initial stiffness (K_d) can be calculated by the analytical solution for the beam on elastic foundation problem which is

$$K_d = 2\left(\frac{E_c}{4E_s I_s}\right)^{3/4} E_s I_s \tag{2.89}$$

in which I_s is the moment of inertia of the steel bar and E_c is the Young's modulus of the concrete.

Figure 2.17 shows how the experimental results from Paulay et al. (1974) and Dei Poli et al. (1992) are compared with the analytical results produced by the Eq. 2.84. For these analyses, the concrete stiffness is estimated by the ACI formula:

$$E_c = 57,000\sqrt{f_c'} \tag{2.90}$$

The analysis slightly underestimates the dowel capacity, but given the simplicity of the model and the few parameters (f_c', d_b, E_s and f_y) to be calibrated, the results are acceptable.

The cyclic response of the dowel action is described by reversal branches that are characterized by maximum and minimum reversal points. A reversal point is defined as the set of force and displacement, (F_r, t_r) when the displacement increment is reversed. Maximum (F_{rp}, t_{rp}) or minimum (F_{rn}, t_{rn}) reversal points are the two reversal points with maximum or minimum registered displacement, respectively. Each reversal branch consists of an unloading and a reloading region. The unloading region initiates when a reversal point is registered and it ends when the reloading branch is reached. It is described by a linearly elastic law with unloading stiffness (K_u), which is assumed to be several times larger than the initial loading stiffness. For the purposes of this study in all

the analyses it is assumed that the unloading stiffness if 5 times the loading stiffness. The first part of the reloading region is described by Eq. 2.91

$$F_d = \begin{cases} F_{tp} e^{\frac{3(t-t_{tn})}{t_{tp}-t_{rn}}} & \text{for positive displacement increment} \\ F_{tn} e^{\frac{3(t-t_{tn})}{t_{tn}-t_{rp}}} & \text{for negative displacement increment} \end{cases} \tag{2.91}$$

in which (F_{tp}, t_{tp}) and (F_{tn}, t_{tn}) are the target points for positive and negative displacement increment and they can be calculated by

$$\left(F_t, t_t\right) = \begin{cases} \left(\alpha_p \cdot F_{rp},\ t_{rp} - \dfrac{F_{rp}}{2K_u}\right) & \text{for positive displacement increment} \\ \left(\alpha_n \cdot F_{rn},\ t_{rn} - \dfrac{F_{rn}}{2K_u}\right) & \text{for negative displacement increment} \end{cases} \tag{2.92}$$

The parameters α_p and α_n can be calculated from Figure 2.18. The second part of the reloading branch is given by

$$F_d = \frac{K_t \cdot \left(t - t_t\right)}{\left(1 + 30 \cdot \left(\dfrac{K_t \cdot \left(t - t_t\right)}{sF_y - F_t}\right) + \left(\dfrac{K_t \cdot \left(t - t_t\right)}{sF_y - F_t}\right)^3\right)^{\frac{1}{3}}} + F_t \tag{2.93}$$

in which K_t is the tangent stiffness at the target point and is calculated by

$$K_t = \begin{cases} \dfrac{F_{rp} \cdot K_d}{F_y} & \text{for positive displacement increment} \\ \dfrac{F_{rn} \cdot K_d}{F_y} & \text{for negative displacement increment} \end{cases} \tag{2.94}$$

Figure 2.19 shows schematically an example of the cyclic behavior of dowel action with the characteristic parameters indicated. The numerical result is compared to experimental

result for cyclic dowel action in a test conducted by Vintzeleou and Tassios (1987) in Figure 2.20. The model simulates very well the initial and reloading stiffnesses, and the dowel capacity but it fails to predict the gradual strength degradation due to cyclic loading.

2.6.4. Performance of the new interface element

It is known that the incorporation of bond-slip elements in FEA can alleviate the sensitivity of the response of reinforcing bars to the element size. However, this still requires that the size of the steel elements is sufficiently small. This is demonstrated below with the bond-slip element presented in a previous section. The advantage of using the new interface formulation in terms of the computational efficiency is also shown.

The physical model considered consists of two concrete blocks separated by a joint and a reinforcing bar passing through the blocks, as shown in Figure 2.21a. It is modeled by plane-stress elements. In the FE models, the nodes that are located along the edges of the lower block are restrained to prevent the vertical displacement and the rotation of the block, while the nodes at the edges of the upper block are subjected to uniform incremental vertical. The steel bar is modeled with truss elements. Different sizes of steel elements, namely, 1, 2, 4 and 8 in. long, are considered in different FE models. The concrete elements match the size of the steel elements. Figure 2.21b and Figure 2.21c show two of the four meshes used in this parametric study.

For the analyses, the steel reinforcement is a No. 4 reinforcing bar with a yield stress of 60 ksi and a tensile strength of 105 ksi. The concrete strength is considered to be 6.0 ksi. Three scenarios are investigated. One is with the steel elements directly

connected to the concrete elements, the second is to have bond-slip interface elements between the two, and the third is to have a finer discretization for the steel elements by using the new interface element formulation for bond-slip.

In the first set of analyses, no bond-slip elements are used. The vertical forces at the nodes of the upper block are recorded and their summation is plotted against the vertical displacements in Figure 2.22a. It is observed that the results vary with the element size. More specifically, the displacement at which the bar ruptures and the load-displacement curves in the pre-peak range are strongly influenced by the element size. This can be largely attributed to the fact that the degree of strain localization near the joint is governed by the element size, as shown in Figure 2.22b. One can also notice that the results do not converge to a unique solution as the element size diminishes.

In the second set of analyses, bond-slip elements are introduced to allow the slip of the truss elements. As shown in Figure 2.23a, results from these analyses are only slightly affected by the element size and the bar rupture point quickly converges as the element size is reduced. The sudden load drops shown in the load-displacement curves are due to the loss of the bond stress in the bond-slip elements. The curves become smoother as the mesh is refined because bond deterioration becomes more gradual and continuous. Moreover, as shown in Figure 2.23b, the extent of strain location is independent of the element size even though the strain magnitude is still affected.

The significant over-strength shown by the analysis with 8-in. elements in Figure 2.23a is due to the fact that a coarser mesh requires a larger bar deformation to trigger the first bond slip. The analyses have shown that in spite of the presence of bond-slip

elements, the length of each bar element has to be no more than $4.0d_b$ to achieve a good solution.

Although, a fine discretization of the steel elements is essential to capture the bond-slip mechanism, it is not necessary to apply fine discretization to the concrete elements. A fine mesh for both concrete and steel elements will increase the computational demand. To overcome the mismatch of the concrete and steel nodes the proposed element formulation and connection methodology can be used.

For the validation of the proposed element formulation, a new parametric study is performed. In this study, the considered models have the coarse and fine concrete meshes shown in Figure 2.21b and Figure 2.21c, respectively but only 1-in. long steel elements. The number of nodes and elements used for the two cases are shown in Table 2.1. Figure 2.24 shows identical results for both cases. Due to the fact that the analysis with coarse mesh has less nodes and elements than the fine mesh analysis, the computational time is 11 times faster, as summarized in Table 2.1.

Table 2.1 - Discretization and computational time

	No. of nodes	**No. of elements**				**Time [sec]**
		Concrete	Steel	Interface	Total	
Fine mesh	611	512	32	32	576	275
Coarse mesh	51	8	32	32	72	22

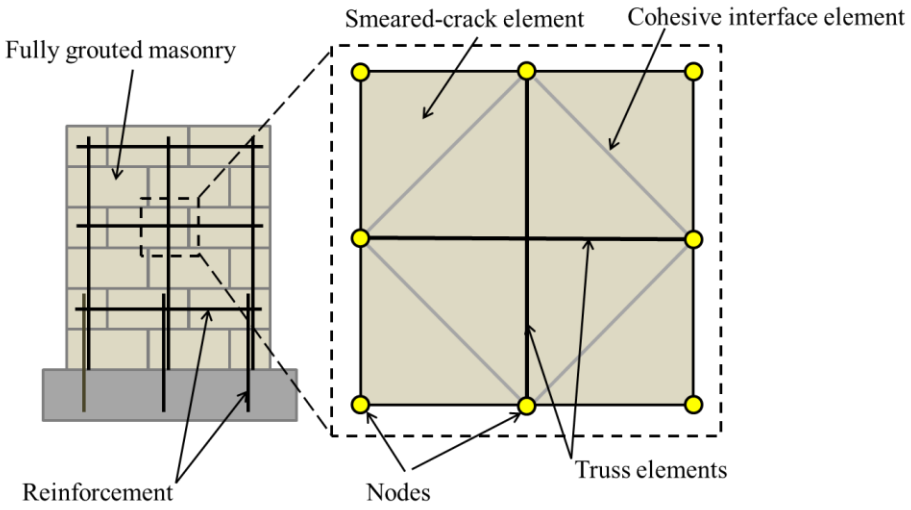

Figure 2.1 - Discretization scheme

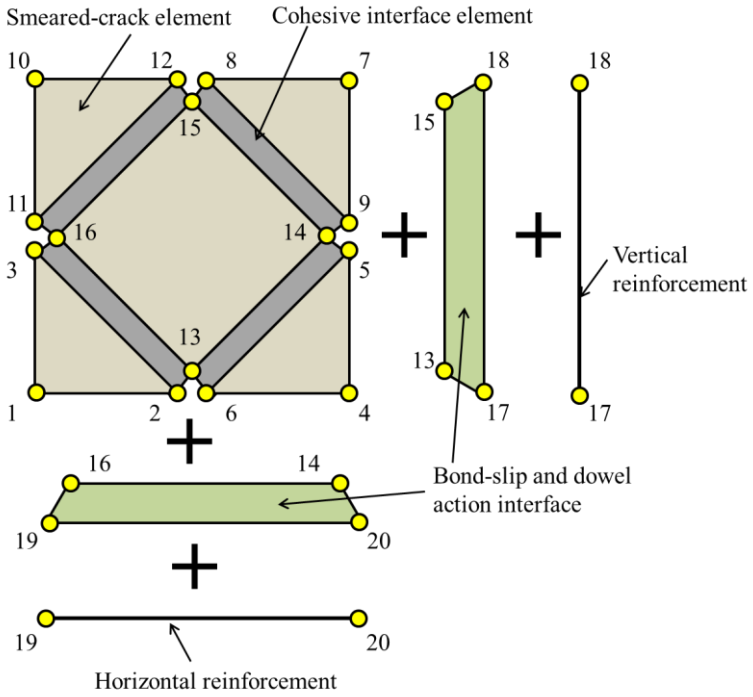

Figure 2.2 - Connectivity details

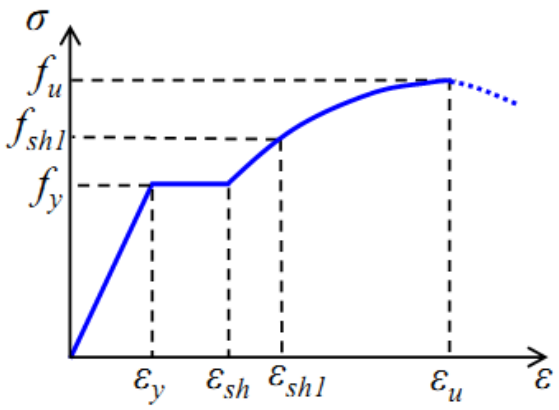

Figure 2.3 - Monotonic stress-strain curve of Dodd-Restrepo steel model (Kim, 2015)

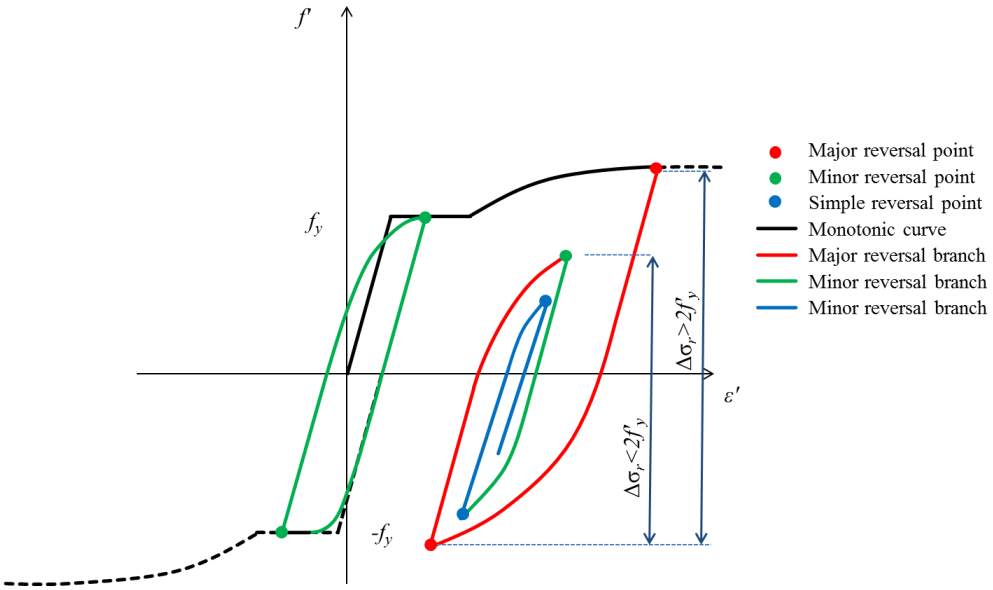

Figure 2.4 - Example of stress reversal branches

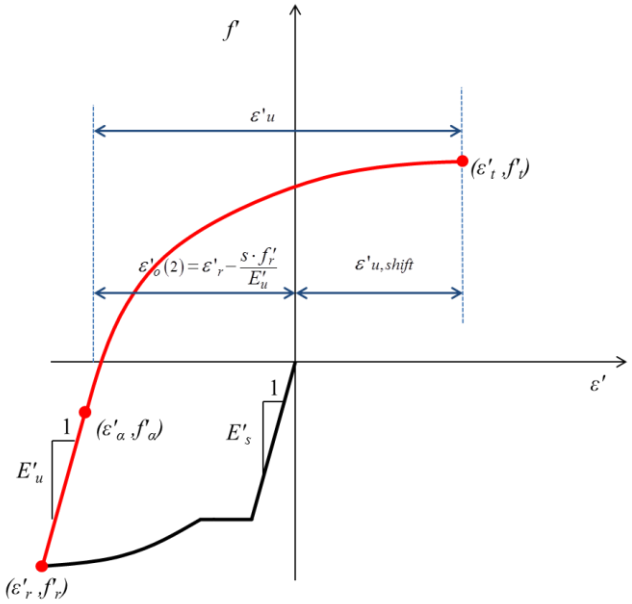

Figure 2.5 - Characteristic points of a stress reversal branch

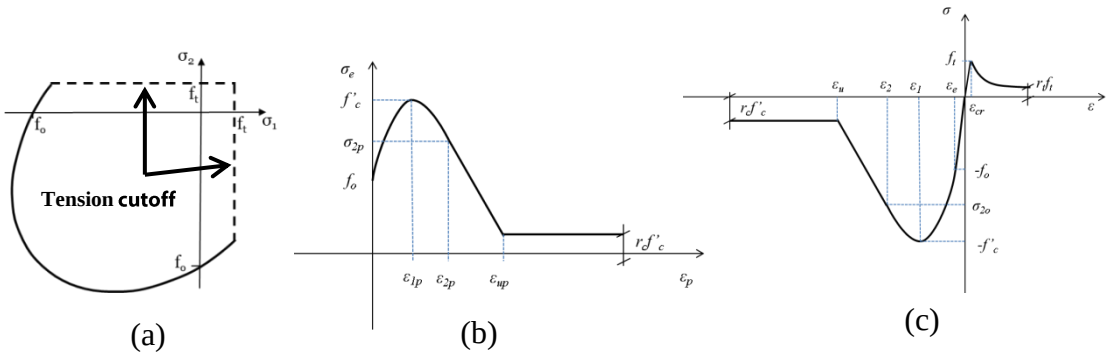

Figure 2.6 - Smeared-crack model: a) failure surface before tensile fracture; b) compressive strain hardening-softening law for the plasticity model; c) orthotropic material law after cracking (Koutromanos, 2015)

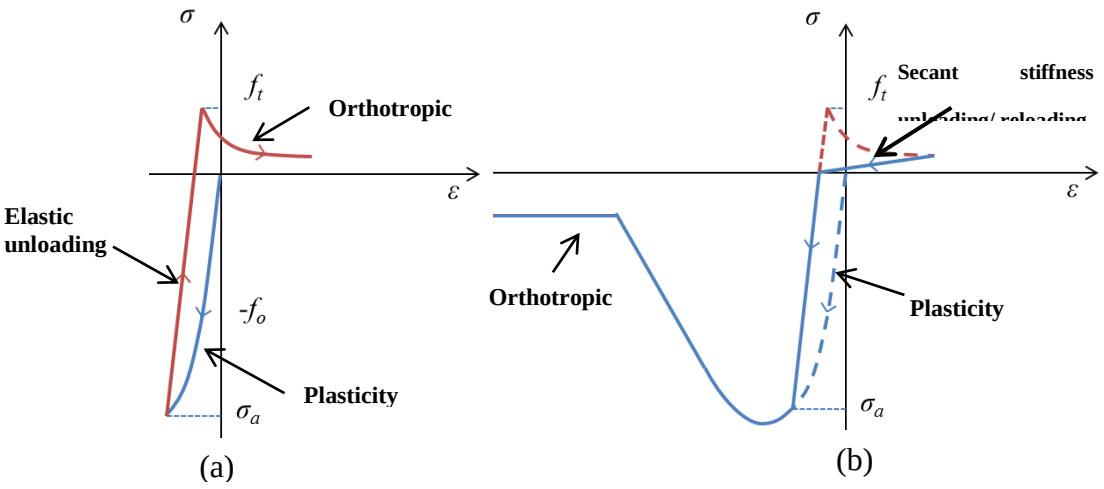

Figure 2.7 - Cyclic behavior: a) loading and unloading; b) reloading (Koutromanos, 2015)

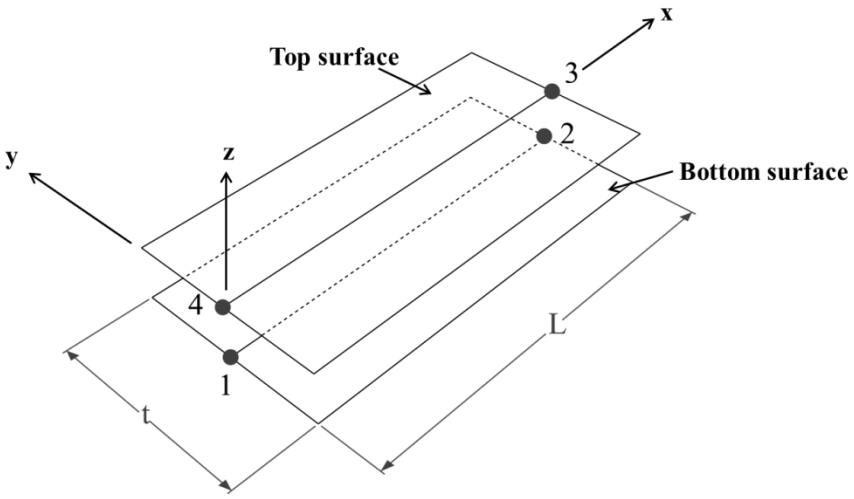

Figure 2.8 - Interface element

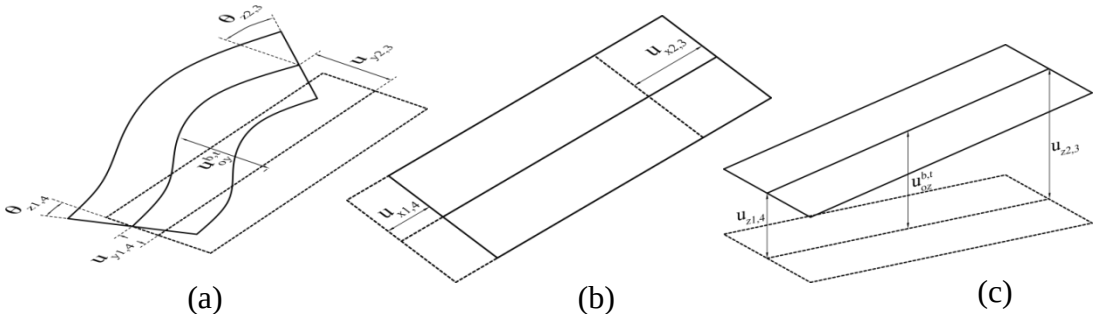

(a) (b) (c)

Figure 2.9 – In-plane displacement due to a) bending deformation; b) axial deformation; c) out-of-plane deformation

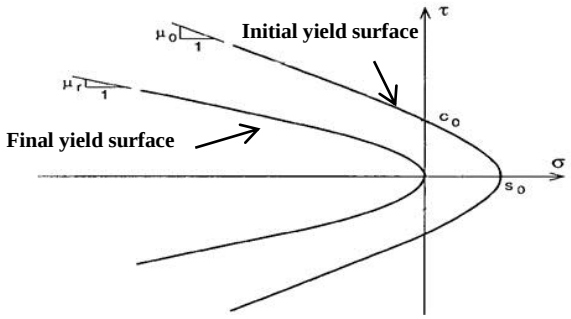

Figure 2.10 - Initial and final yield surfaces in stress space (Koutromanos, 2011)

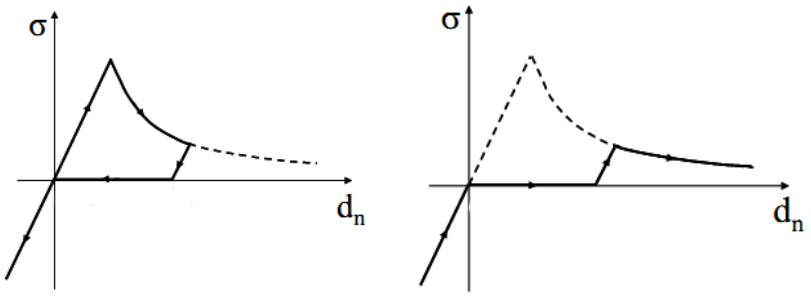

(a) (b)

Figure 2.11 - Uniaxial behavior of the interface: a) normal tensile loading and unloading; b) tensile reloading (Koutromanos, 2011)

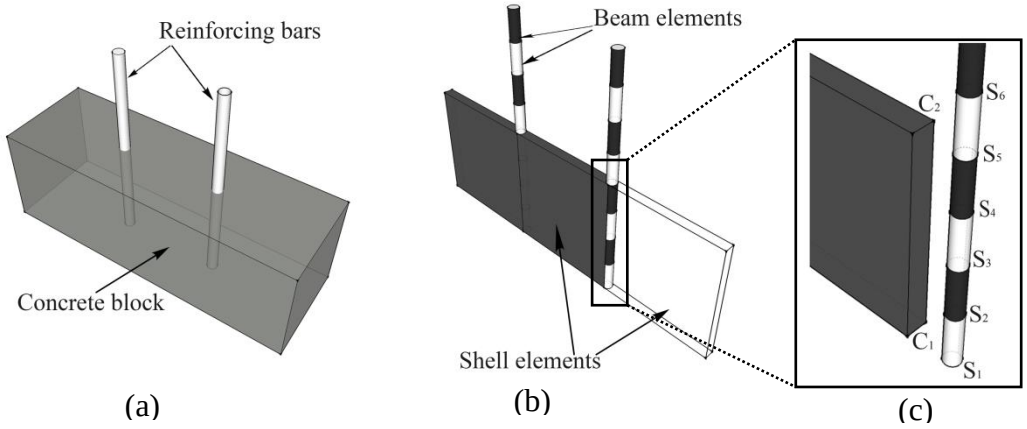

Figure 2.12 - Modeling of steel-concrete interaction: (a) physical model; (b) FEA model, (c) element size mismatch

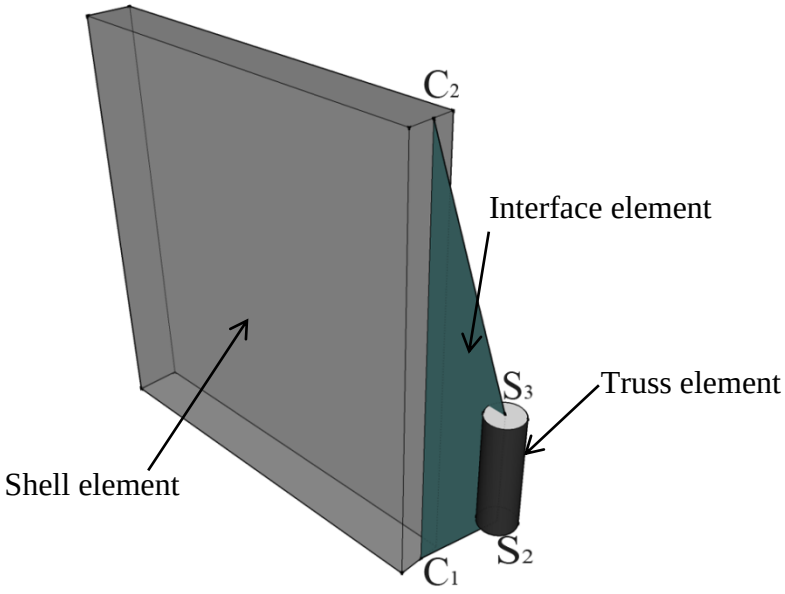

Figure 2.13 - Steel-concrete connectivity through interface element

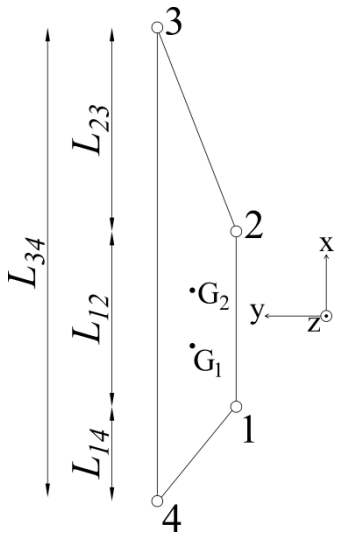

Figure 2.14 - Interface element

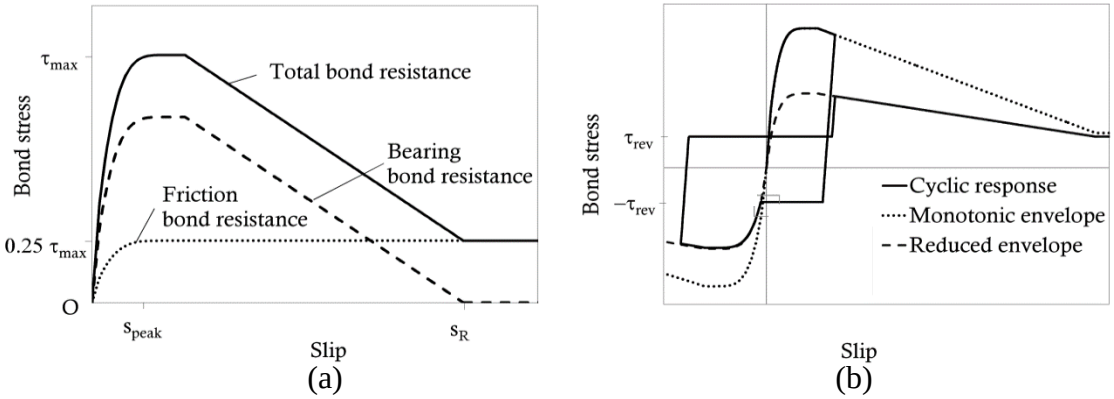

Figure 2.15 - Bond-slip model: a) monotonic response; b) cyclic response (Murcia-Delso and Shing 2014)

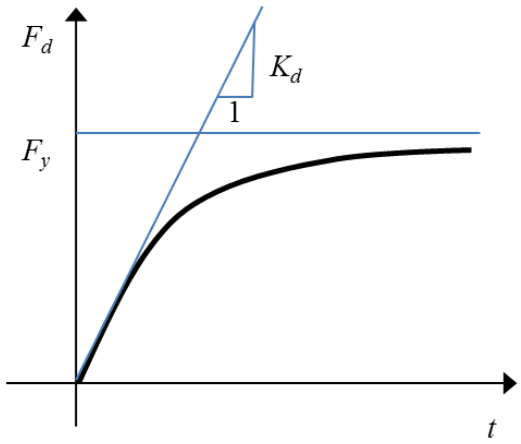

Figure 2.16 - Monotonic dowel force-vs-displacement relation

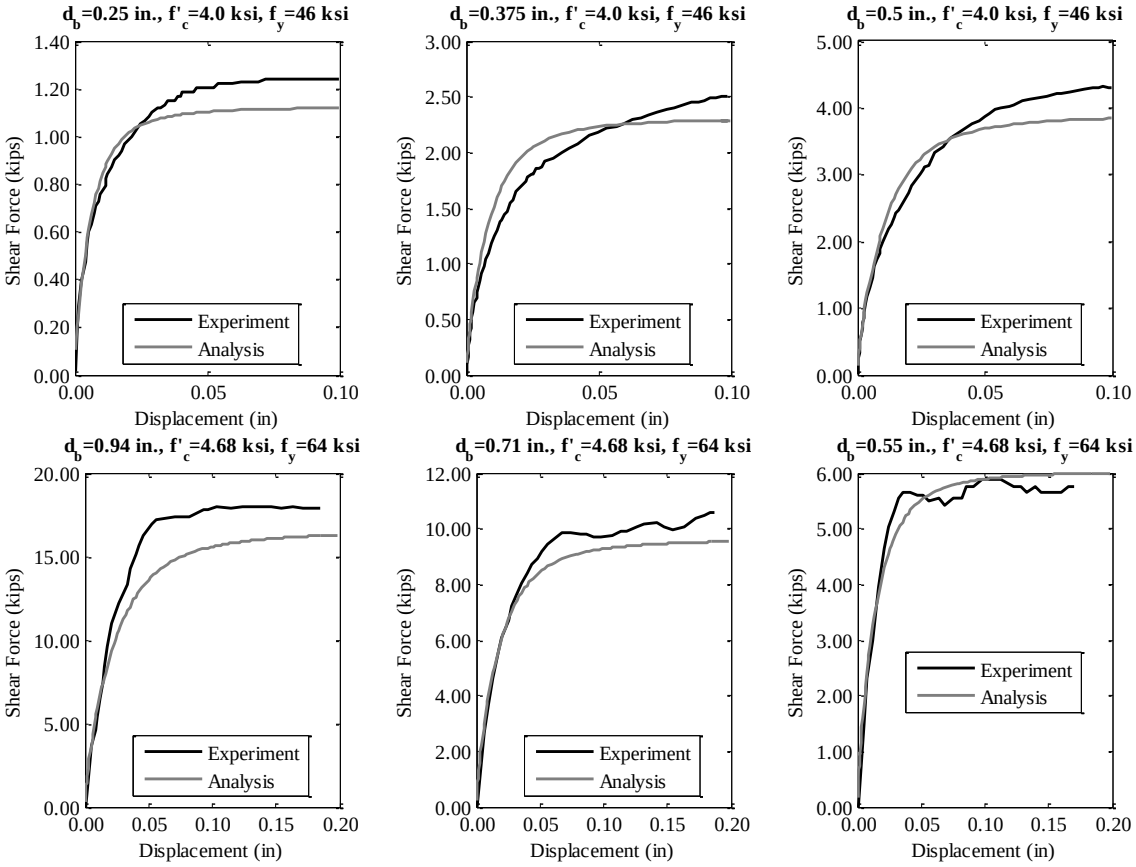

Figure 2.17 - Comparison of experimental and analytical results for monotonic dowel action behavior (Paulay et al., 1974, Dei Poli et al., 1992)

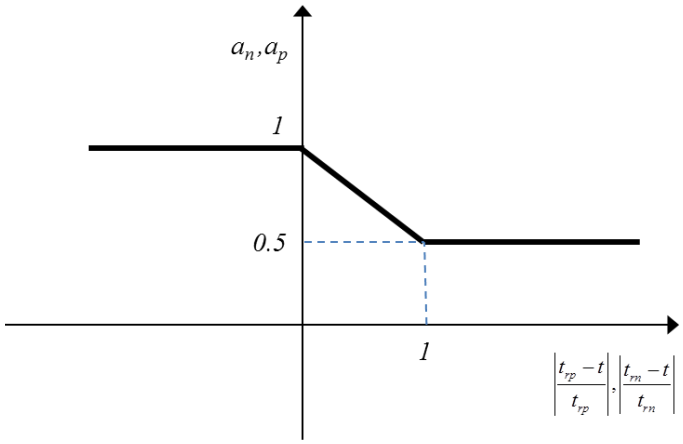

Figure 2.18 - Values of parameters a_n and a_p

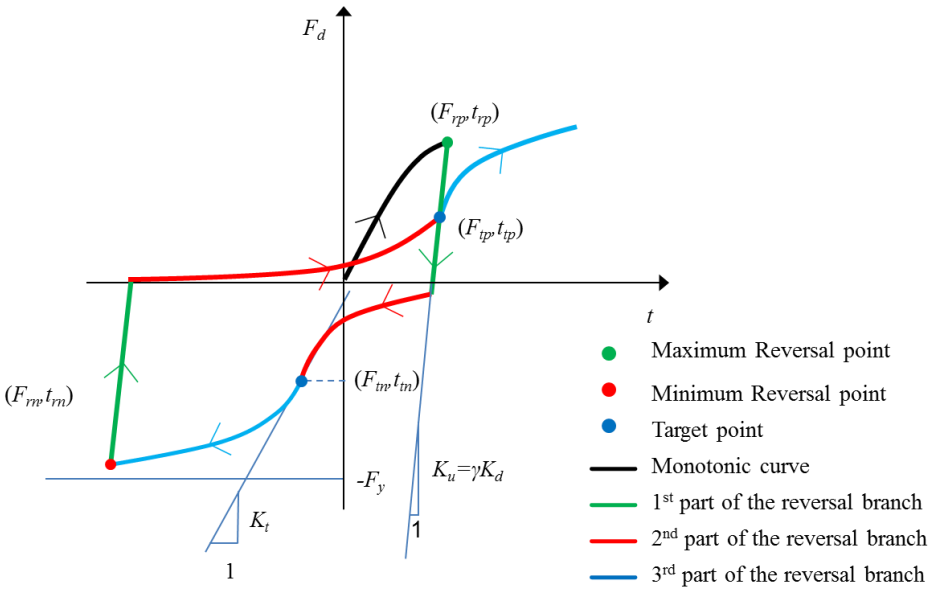

Figure 2.19 - Example of cyclic dowel force-vs-displacement relation

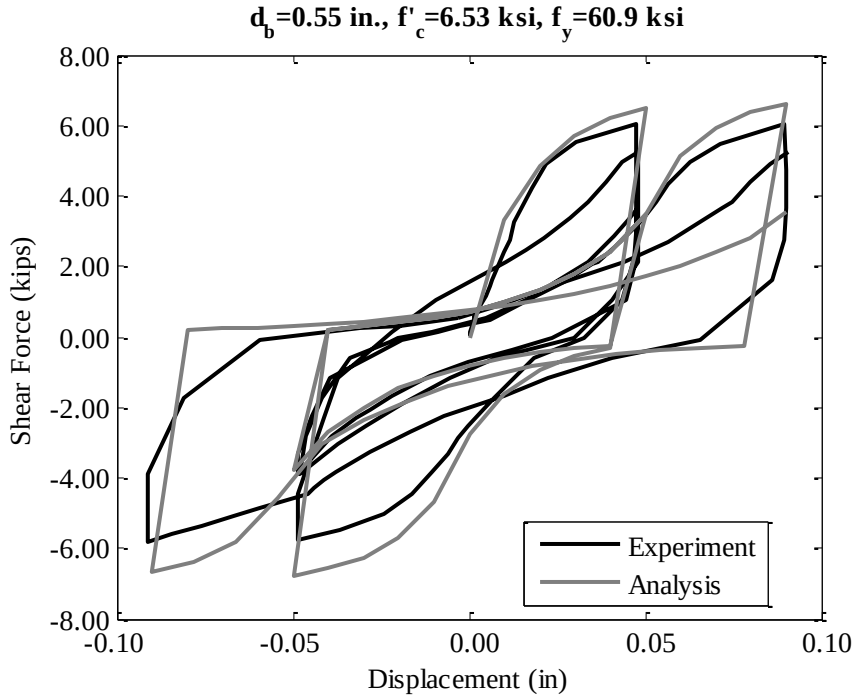

Figure 2.20 - Comparison of experimental and numerical results for cyclic dowel action behavior

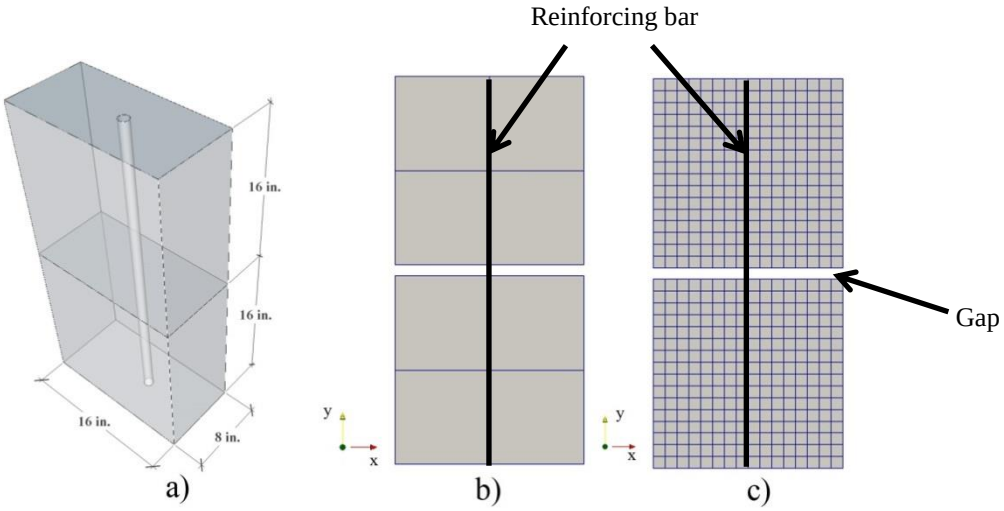

Figure 2.21 - Modeling of tension test: (a) physical model, (b) coarse-mesh FE model (8-in. elements), (c) fine-mesh FE model (1-in. elements)

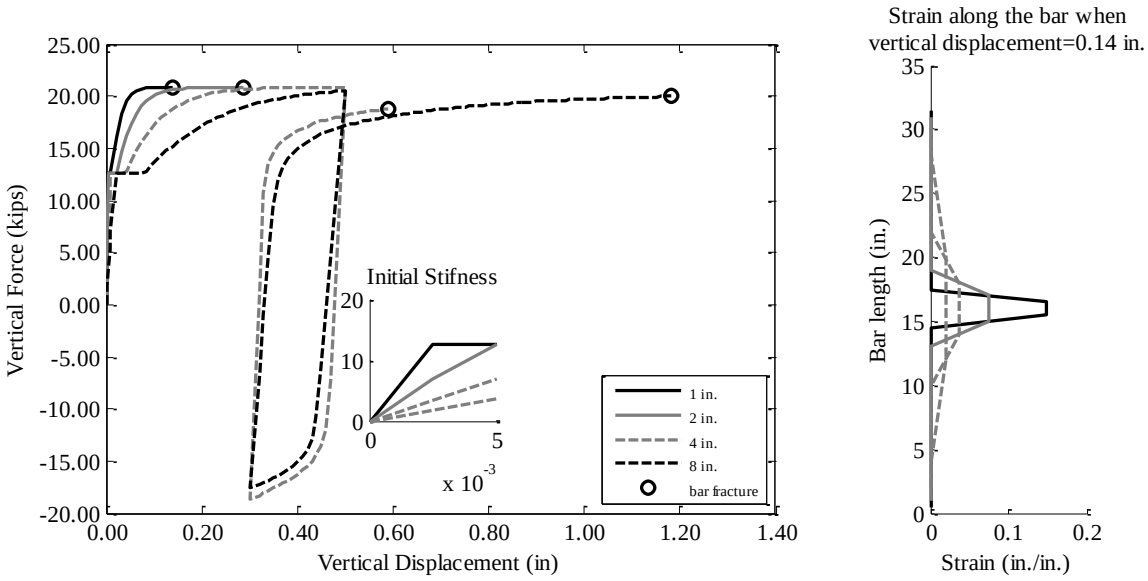

Figure 2.22 – Modeling of tension test without bond-slip elements: a) force-vs-displacement, b) strain along the bar

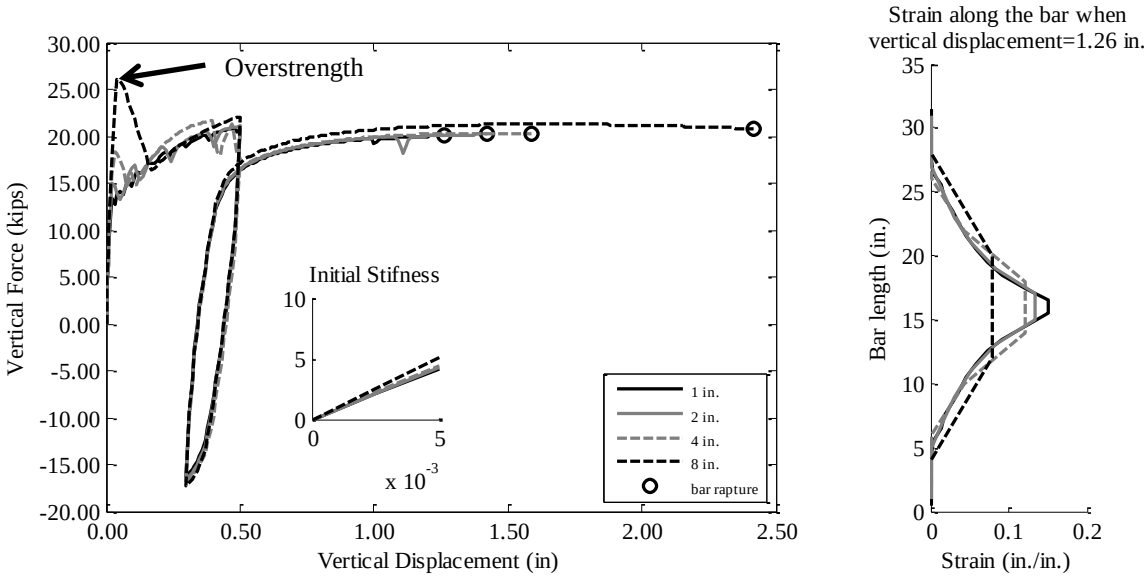

Figure 2.23 - Modeling of tension test with bond-slip elements: a) force-vs-displacement, b) strain along the bar

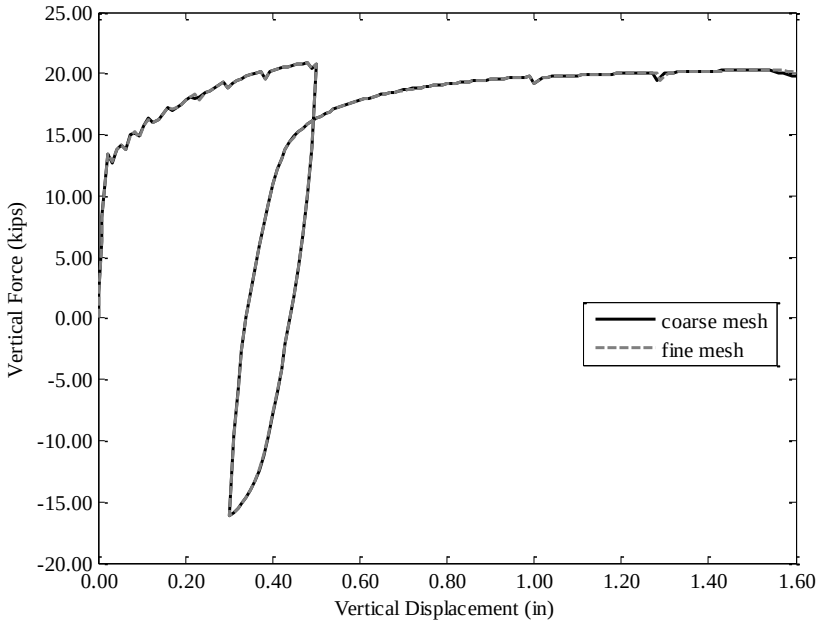

Figure 2.24 - Numerical results for tension test with different mesh discretizations

3. VERIFICATION OF THE MODELING METHOD

Results of quasi-static tests on single reinforced masonry walls tested by Ahmadi (2012), Voon (2007), Shing et al. (1991) and Kapoi (2012), are used to validate the proposed finite element modeling method. The wall responses chosen to be compared to verify the modeling and analysis approach are the failure mechanism, the hysteretic loops of the lateral force-vs.-the lateral displacement, the hysteretic energy dissipation, the stiffness and the strength of the walls. The good agreement between the experimentally recorded data and the numerically computed results indicates that the proposed modeling method can accurately simulate the behavior of reinforced masonry walls. Moreover, a parametric study is performed to investigate the influence of the cohesive crack interfaces, the bond-slip and dowel-action interfaces, and the steel material model on the cyclic behavior of the walls.

The proposed analysis method is able to predict different wall failure mechanisms. The wall specimens selected here for the model validation have different aspect ratios, splice lengths, wall thicknesses, reinforcement ratios, axial loads and boundary conditions. They exhibited different failure mechanisms, including flexure-dominated behavior, shear-dominated behavior, and sliding-dominated behavior. The design details of the investigated wall segments are summarized in Table 3.1. The layouts, reinforcement plans, and test setups for the wall specimens are shown in Figure 3.1 through Figure 3.12.

3.1. Shell and truss element size

The finite element modeling scheme and the constitutive models presented in Chapter 2 are used here. In reinforced masonry structures that are constructed of hollow block units, the reinforcing bars are placed in the center of the cells. Therefore, the space between adjacent reinforcing bars is always an integer multiple of the distance between the centers of two adjacent cells, which is 8 in. Hence, it is convenient to use modules of shell elements as shown in Figure 2.2, with outer dimensions of 8 x 8 in. (formed by four triangular elements with 4-in. sides surrounding a diamond-shaped element with $4\sqrt{2}$ -in. sides). The shell elements are connected by cohesive crack interface elements. This mesh size is convenient because it positions the nodes of the diamond-shaped elements along the locations of the vertical and horizontal reinforcing bars. However, a more refined mesh is used for the wall toe regions where masonry crushing is expected. By refining the mesh in the toe regions, the gauss points will be closer to the base of the walls where the highest compressive strains will be registered. This will capture the strengths of the walls in a more accurate manner. The meshing schemes used for the wall analyses are presented in Figure 3.13 through Figure 3.15.

As it is extensively discussed in Section 2.6.4, the truss elements need to be sufficiently small ($< 2\,d_b$) to capture the bond-slip in an accurate manner. For this reason, 1-in. long elements are used in all the analyses due to the fact that the smallest reinforcing bars used in the test specimens were No. 4 bars. The smaller bar elements are connected to the larger shell elements using the specially developed bond-slip/dowel action interface elements presented in Chapter 2.

3.2. Material parameter calibration and modeling details

The material properties of the specimens and the values of the material parameters for the constitutive models used in the analyses are shown in Table 3.2 and Table 3.3. To calibrate the smeared-crack shell elements, the compressive stress-strain relation for masonry has to be determined from masonry prism tests. However, the slope of the descending branch of the stress-strain relation, representing the softening behavior of masonry, needs to depend on the size of the shell elements used in the analysis in order to preserve the objectivity of the fracture energy release and of the numerical results. The post-peak stress-strain relations selected for the two meshing schemes used in the wall analyses (see Figure 3.13 through Figure 3.15) are determined by the analysis of four masonry prism specimens, which were prepared for a two-story reinforced masonry wall structure tested on a shake table, as it is presented in Chapter 5. The two meshing schemes applied to the prism analyses are shown in Figure 3.16. One has a coarse mesh and the other has a fine mesh. In the prism models, all the nodes at the base are fixed, while vertical displacements are imposed at the top nodes. However, the model is allowed to deform freely in the horizontal direction without boundary restraints. As shown in Table 3.4, different values of ε_u are used for the coarse and fine meshes to have different post-peak compressive stress-strain relations to maintain the objectivity of the numerical results. The compressive force - vs. - the vertical displacement relations obtained from the tests and the analyses are compared in Figure 3.17. It can be observed that the two different meshes result in similar behaviors.

For most of the walls analyzed here, data on the compressive force - vs. - displacement relations for the masonry are not available and only the compressive strengths are given. Hence, in these analyses, the Young's modulus for the smeared-crack elements is estimated with Eq. 2.90, and it is assumed that $\varepsilon_1 = 0.002$, $\varepsilon_u = 0.02$ for the coarse mesh and $\varepsilon_u = 0.05$ for the fine mesh, which have been determined from the above prism analyses, regardless of the compressive strength. This implies that the fracture energy for compression will be more or less proportional to the compressive strength of the masonry, which may not be exactly true but is sufficient accurate in view of the uncertainties in the localization of compressive strains in a wall. The tensile strength of masonry is assumed to be 0.4 ksi, which is 7-10% of the compressive strengths of the masonry.

Equations 2.78 through 2.94 define the bond–slip and dowel action laws, and they require the compressive strength of the grout that surrounds the steel. In the cases that the grout compressive strength is not available (i.e., for walls A1 and A2), the compressive strength of the masonry prisms was used instead. For the cohesive interface law, the coefficient of friction is taken to be 0.7 for smooth surfaces (i.e., the interface between the wall and the foundation slab that had a smoothen surface), 1.2 for intentionally roughened surfaces, and 1.5 for crack surfaces in walls. These values are similar to those proposed by ACI 318-08 for concrete. The dilatation coefficient, ζ_{dil}, which controls the dilatation associated with shear sliding due to surface asperities, is assumed to remain constant at 0.3 for rough surfaces and 0.01 for smooth surfaces. For the rest of the material parameters, the values proposed by Koutromanos (2011) have been adopted and

are shown in Table 3.3. The yield and ultimate strengths, the Young's modulus, and the other strain parameters (ε'_{sh}, $\varepsilon'_{sh,1}$ and ε'_{u}) required by the steel model developed by Kim (2015) are determined with data from tensile tests.

The lap splices are modeled in the way shown in Figure 3.18 using the bond-slip/dowel action interface elements to connect the bars. The 180^{o} and 90^{o} hooks of the reinforcing bars are assumed to provide rigid anchorage and are thus modeled by connecting the nodes of the truss elements directly to the nodes of the shell elements without any interface in between.

The nonlinear analyses are conducted with a modified Newton-Raphson scheme using the initial stiffness matrices of the walls.

3.3. Comparison of experimental and numerical results

3.3.1. Flexure-dominated walls

The first validation analysis is performed on two cantilever walls, C2 and C3, which had an aspect ratio of 2, tested by Kapoi (2012). During test of C2, the opening of the mortar bed joints was observed. At the completion of the test, toes at both sides of the wall were crushed and the crushing extended up to the second course as shown in Figure 3.19. No rupture or buckling of the vertical reinforcement was observed. The wall was considered to be flexure dominated and its strength degradation can be attributed to the masonry crushing. Wall C3 exhibited a very complicated behavior, which was influenced by the dowel action of the vertical reinforcement. The No. 7 vertical bars caused vertical splitting cracks in the wall. The vertical splitting cracks were followed by the severe

crushing of masonry in the lower three courses as shown in Figure 3.20. Without the masonry cover, the extreme vertical bars lost the lateral support and buckled.

The discretization scheme proposed in Chapter 2 is used to model both walls C2 and C3, but with a refined mesh at the wall toes to better capture the strength of the walls. The coarse and fine meshes have different values of ε_u as mentioned in the previous section. To overcome the issue of the nodal location mismatch between the fine and coarse meshes shown in Figure 3.13, the cohesive interface elements are modified to have the same element formulation as the bond-slip elements presented in Section 2.6.1. Bar buckling is not modeled here.

The experimentally recorded and numerically computed force-vs.-displacement curves for the two walls are compared in Figure 3.21 and Figure 3.22. For wall C2, the model is able to reproduce well the hysteretic loops, and it captures the initial stiffness as well as the strength degradation. It underestimates the strength of wall C2 by 10% and 7% in the positive and negative directions, respectively. As shown in Figure 3.19, the mesh indicates severe crushing in the smeared-crack elements. The crushing shown in the figure is localized only in the first row of elements. However, the post-peak behavior is well captured due to the fact that the uniaxial compressive stress-strain relation specified for the elements compensates for the localization of the softening behavior by regularizing the fracture energy release. On the other hand, the analysis for wall C3 fails to capture the strength degradation associated with the buckling of the vertical reinforcement due to the fact that this phenomenon is not taken into account in the finite element model. However, the model describes very well the pre-peak behavior of the wall including the initial stiffness and the strength of the wall.

3.3.2. Shear-dominated walls

The second group of walls analyzed here were tested by Ahmadi (2012), Voon (2007) and Shing et al. (1991). They were shear dominated. Walls A1, A2 and Sp. 5 were cantilever walls, while wall UT-PBS-01 had fixed-fixed end conditions imposed by two vertical actuators as shown in Figure 3.5. All four walls had diagonal shear cracks, and in the case of UT-PBS-01, crushing was observed along the diagonal strut. Wall A1 had crushing at its toes. The damage patterns observed in the tests and the deformed meshes for the three walls are compared in Figure 3.23 through Figure 3.26. Although the crack patterns are very well duplicated, the deformed meshes for walls A2 and Sp. 5 indicate masonry crushing on the right side, which was not observed in the tests.

The tensile strength of the masonry governs the shear capacity of the walls prior to the development of diagonal cracks. After diagonal cracking, the shear resistance is provided by the horizontal reinforcement, the diagonal strut, the friction at the crack surfaces, and the dowel action of the vertical reinforcement. The model can simulate all these mechanisms and the strength degradation, providing a good agreement with the experimental results, as shown in Figure 3.27 through Figure 3.30.

3.3.3. Sliding-dominated walls

For the last validation analysis, wall UT-PBS-03, which exhibited significant sliding at its base, is considered. It is a cantilever wall with zero axial load and an aspect ratio of 1. The final failure mode of the specimen was a combination of sliding at the base and that along the bed joint between the second and the third masonry courses from the base. Furthermore, extensive crushing was observed at the right toe of the wall, and

diagonal cracks developed at the center of the specimen, as shown in Figure 3.31. The model is able to predict these damages and the sliding of the wall, as shown in Figure 3.1.

During the last two cycles, three vertical reinforcing bars at the two ends of the specimen fractured, causing sudden drops of the load capacity, as shown Figure 3.33. The steel material law used in the analysis does not account for bar fracture. Therefore, these load drops are not captured by the model.

3.3.4. Hysteretic energy dissipation

The model slightly underestimates the hysteretic energy dissipation in all analyses except in the case of wall C3, as shown in Figure 3.34 through Figure 3.40.

3.4. Influence of the bond-slip and dowel-action interface

To investigate the influence of the bond-slip and dowel-action behavior on the numerical results, the analyses of walls C2, A2 and UT-PBS-03 are repeated. For these analyses, the steel elements are directly connected to the concrete elements. The behavior of wall C2 becomes a little stiffer as shown in Figure 3.41b. Furthermore, the hysteretic energy dissipation increases as shown in Figure 3.41a. However, the strength of the wall is not greatly affected due to the fact that wall C2 is flexure dominated and its capacity does not depend on the dowel action. However, the behavior of walls A2 and UT-PBS-03 is significantly affected by the omission of the dowel action. For wall A2, which is shear dominated, the dowel action of the vertical reinforcement crossing the diagonal cracks provides some shear resistance. Without the dowel-action interfaces, only friction provides the shear resistance along the diagonal cracks. Hence, the strength of the wall and the hysteretic energy dissipation decrease, as shown in Figure 3.42. For wall UT-

PBS-03, which is dominated by base sliding, the omission of dowel action has a significant consequence as shown in Figure 3.43. The model overestimates the wall capacity in the positive direction but significantly underestimates the capacity in the negative direction. In the first few cycles, the frictional resistance at the base of the wall is sufficient to prevent sliding. However, in the subsequent cycles, when the wall is displaced towards the positive direction by a significant amount, the vertical steel elements on the left side of the wall have tensile strains exceeding the yield level. When the displacement is reversed towards the negative direction, the bars previously yielded in tension is in compression but retaining some residual tensile strains, which prevent the crack at the left side of the base from complete closing and thus reduces the shear friction. In the absence of the dowel mechanism of the vertical steel, the wall loses most of the sliding resistance. As sliding initiates in the negative direction, the vertical reinforcing bars on the right side cannot develop significant tension. Therefore, the crack at the right side of the base can be completely closed and the shear friction is retained when the wall displacement is reversed again towards the position direction.

3.5. Influence of steel modeling

The stress-strain relation of mild steel exhibits a plateau when yielding first occurs and then a strain hardening behavior afterwards. Under cyclic loading, steel also exhibits the Bauschinger effect. However, in many analyses, steel is simply treated as an elastic-perfectly plastic material. To examine the consequence of this simplification, walls C2 and A2 are analyzed again with the simplified steel law. Wall C2 is flexure dominated, while wall A2 is shear dominated. As shown in Figure 3.44, with the

simplified steel law, the model underestimates the flexural capacity of wall C2 because the elastic-perfectly plastic steel law does not account for the strain hardening. Furthermore, the unloading stiffness is not well simulated. As shown in Figure 3.45, the behavior of wall A2 is not significantly affected by the steel law. This is because the horizontal bars in the shear-dominated wall cannot develop significant strain hardening before significant load degradation occurs.

3.6. Influence of cohesive crack interfaces

Finally, the influence of the cohesive crack interfaces on the behavior of walls C2 and A2 under cyclic loads has been investigated. The results from the analyses of these two walls without the cohesive crack interfaces are presented in Figure 3.46 and Figure 3.47. It can be seen that the cohesive crack interfaces influence the behavior of both the flexure-dominated and the shear-dominated walls. More specifically, the analysis of wall C2 without the discrete cohesive interfaces overestimates the strength and stiffness of the actual specimen. For wall A2, the response becomes more ductile with very little strength degradation. The latter is associated with the stress-locking phenomenon, which is an inherent problem of the smeared-crack elements (Rots et al., 1989 and Lotfi and Shing., 1991).

Table 3.1 - Design details of wall specimens

Wall name	Tested by	Nominal length (in.)	Nominal height (in.)	Aspect ratio	Axial load (kips)	Vertical Reinf.	Horizontal Reinf.	Splice length (in.)	Thickness (in.)	Boundary conditions	Failure mechanism
C2	Kapoi (2012)	40	80	2	48	#4 @ 8 in.	#4 @ 8 in.	16 in. at the base	7.625	Cantilever	Flexure
C3	Kapoi (2012)	40	80	2	48	#7 @ 8 in.	#4 @ 8 in.	46 in. at the base	7.625	Cantilever	Flexure
PBS-01	Ahmadi (2012)	72	72	1	20	#6 @ 8 in.	#4 @ 8 in.	16 in. at mid-height	7.625	Fixed-ends	Shear
PBS-03	Ahmad (2012)	96	96	1	0	#4 @ 8 in.	#4 @ 8 in.	16 in. at the base	7.625	Cantilever	Sliding
A1	Voon (2007)	70. 87	70.87	1	0	5-D20	5-R6	No splices	5.51	Cantilever	Shear
A2	Voon (2007)	70. 87	70.87	1	0	5-D20	5-R6	No splices	5.51	Cantilever	Shear
Sp. 5	Shing et al. (1991)	72	72	1	43	#7 @ 16 in.	#3 @ 16 in.	No splices	5.625	Cantilever	Shear

Table 3.2 - Material properties of wall specimens

	Wall name						
	C2	**C3**	**PBS-01**	**PBS-03**	**A1**	**A2**	**Sp .5**
Average grout compressive strength (psi)	5,528	4,770	5,968	4,670	N/A	N/A	2,889
Average compressive strength of CMU prisms (psi)	3,038	2,279	3,113	4,447	2,550	2,550	2,637
Reinforcement size	No 4	No 4 / No 7	No 4 / No 6	No 4	D20/R6	D20/R6	No 3/ No 7
Average yield strength of steel (ksi)	66	66	62.4 / 63.2	61.4	45	45	65
Average tensile strength of steel (ksi)	N/A	N/A	100.5 / 102.7	98.7	67	57 / 72	82 / 105

Table 3.3 - Material parameters used for wall analyses

		Wall name						
Type of element	Material parameter	**C2**	**C3**	**PBS-01**	**PBS-03**	**A1**	**A2**	**Sp. 5**
Cohesive Interfaces at the base	Tensile strength, s_o (ksi)	0.2	0.2	0.2	0.2	0.2	0.2	0.2
	Initial and residual dilatation coefficient, $\zeta_{dil,o} / \zeta_{dil,r}$	0.01	0.01	0.01	0.01	0.3	0.3	0.3
	Initial and residual coefficient of friction, μ_o / μ_r	0.7	0.7	0.7	0.7	1.2[1]	1.2[1]	1.2[1]
	G_f^I (kip/in)	0.0004	0.0004	0.0004	0.0004	0.0004	0.0004	0.0004
	G_f^{II} (kip/in)	0.004	0.004	0.004	0.004	0.004	0.004	0.004
	r_o / r_r	0.05 /0.01	0.05 /0.01	0.05 /0.01	0.05 /0.01	0.05 /0.01	0.05 /0.01	0.05 /0.01
All other cohesive Interfaces	Tensile strength, s_o (ksi)	0.4	0.4	0.4	0.4	0.2	0.2	0.4
	Initial and residual dilatation coefficient, $\zeta_{dil,o} / \zeta_{dil,r}$	0.3	0.3	0.3	0.3	0.3	0.3	0.3
	Initial and residual coefficient of friction, μ_o / μ_r	1.5	1.5	1.5	1.5	1.5	1.5	1.5
	G_f^I (kip/in)	0.0004	0.0004	0.0004	0.0004	0.0004	0.0004	0.0004
	G_f^{II} (kip/in)	0.004	0.004	0.004	0.004	0.004	0.004	0.004
	r_o / r_r	0.05 /0.01	0.05 /0.01	0.05 /0.01	0.05 /0.01	0.05 /0.01	0.05 /0.01	0.05 /0.01
Smeared-crack Shell elements	Thickness (in.)	7.625	7.625	7.625	7.625	5.51	5.51	5.625
	Elastic modulus, E_c (psi)	3100	2800	3100	3700	2800	2800	2900
	Tensile strength, f_t (ksi)	0.4	0.4	0.4	0.4	0.4	0.4	0.4
	f_o (ksi)	0	0	0	0	0	0	0
	Compressive strength, f_c' (ksi)	3.1	2.4	3.1	4.4	2.55	2.55	2.7
	ε_u	0.02 / 0.05[2]	0.02 / 0.05[2]	0.02	0.02	0.02	0.02	0.02
	ε_1	0.003	0.003	0.003	0.003	0.003	0.003	0.0025
Steel bar	Size	No 4	No 4 / No 7	No 4 / No 6	No 4	D20 / R6	D20 / R6	No 3/ No7
	Yield strength, f_y (ksi)	66	66	62.4 / 63.2	66	45	45	57 / 72
	Tensile strength, f_u (ksi)	110	110	100.5 /102.7	98.7	67	67	82 / 105
	Elastic modulus, E_s (ksi)	29000	29000	29000	29000	29000	29000	29000
	ε_{sh}'	0.009	0.009	0.009	0.009	0.03	0.03	0.01
	$f_{sh,1}$ (ksi)	84	84	84	84	60	60	65 / 80
	$\varepsilon_{sh,1}'$	0.029	0.029	0.029	0.029	0.08	0.08	0.02
	Ultimate strain, ε_u'	0.15	0.15	0.15	0.15	0.17	0.17	0.15
Bond-slip/dowel action interface	Dowel strength, F_y (kips)	5.64	5.21 / 14.75	5.56 / 11.85	5.07	6.82 / 0.76	6.82 / 0.76	2.12 / 11.39
	Loading stiffness (kips/in)	902	835 / 1462	902 / 1545	1030	1315 / 394	1315 / 394	646 / 1501
	Unloading stiffness (kips/in)	4511	4179 / 7314	4511 / 7726	5151	6578 / 1972	6578 / 1972	3218 / 7509
	Grout compressive strength, f_c' (ksi)	5.5	4.8	5.6	4.6	2.55	2.55	2.9

[1] The surface at the base was intentionally roughened

[2] For the coarse mesh and fine mesh, respectively

Table 3.4 - Material parameters for smeared-crack model for masonry prism analyses

	Prism 1		Prism 2		Prism 3		Prism 4	
Mesh type	**Coarse**	**Fine**	**Coarse**	**Fine**	**Coarse**	**Fine**	**Coarse**	**Fine**
Thickness (in.)	7.625		7.625		7.625		7.625	
Elastic modulus (psi)	2400		2040		2040		2040	
Tensile strength, f_t (ksi)	0.4		0.4		0.4		0.4	
f_o (ksi)	0		0		0		0	
Compressive strength, f_c' (ksi)	2.5		2.0		2.33		2.55	
ε_u	0.02	0.05	0.02	0.05	0.015	0.04	0.02	0.05
ε_1	0.002		0.002		0.0018		0.0016	

Table 3.5 - Lateral load capacities from tests and analyses

	Wall Name	Positive direction	Negative direction
Experimental results (kips)	C2	32.5	-30.1
	C3	39.0	36.8
	PBS-01	196.1	-178
	PBS-03	82.3	-81.9
	A1	49.0	-45.4
	A2	39.6	-43.3
	Sp. 5	87.3	-83.2
Numerical results (kips)	C2	29.5	-28
	C3	38.5	39
	PBS-01	192.1	-181.9
	PBS-03	85.2	-85.5
	A1	44.2	-48.5
	A2	43.0	-48.1
	Sp. 5	86.6	-82.8
Error (%)	C2	-9.2	-7.0
	C3	-1.3	6.0
	PBS-01	-2.0	2.2
	PBS-03	3.5	4.4
	A1	-9.8	6.9
	A2	8.6	11.1
	Sp. 5	0.6	0.5

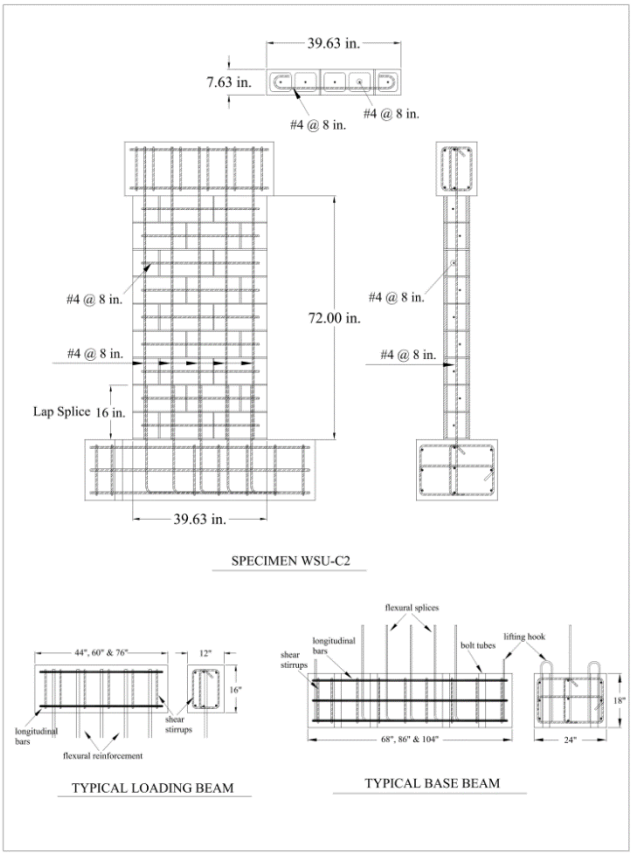

Figure 3.1 - Reinforced masonry wall C2 tested by Kapoi (2012)

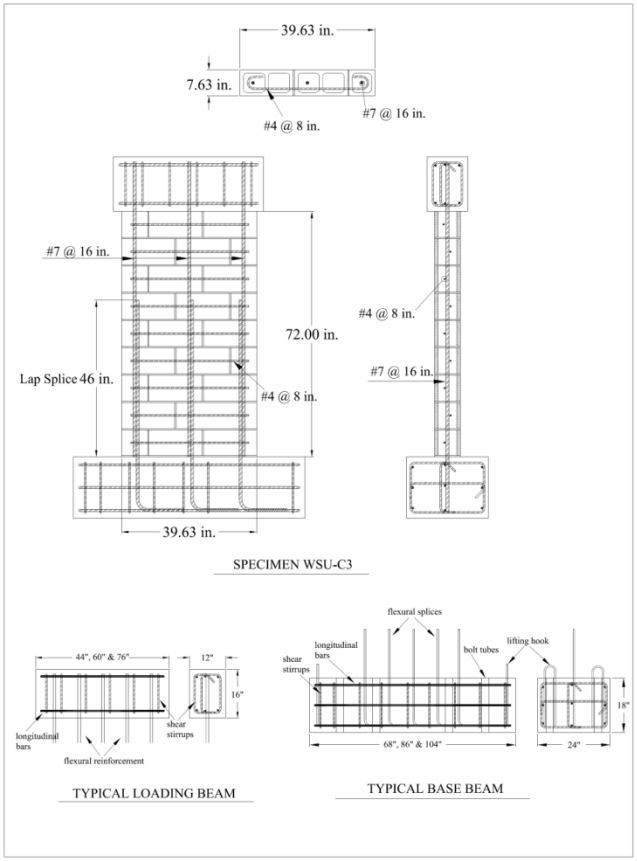

Figure 3.2 - Reinforced masonry wall C3 tested by Kapoi (2012)

Figure 3.3 - Test setup for walls C2 and C3 (Kapoi, 2012)

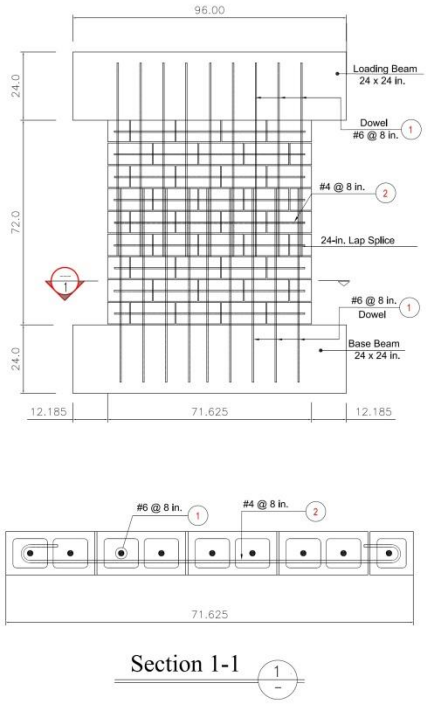

Figure 3.4 - Reinforced masonry wall UT-PBS-01 tested by Ahmadi (2012)

Figure 3.5 - Test setup for wall UT-PBS-01 (Ahmadi, 2012)

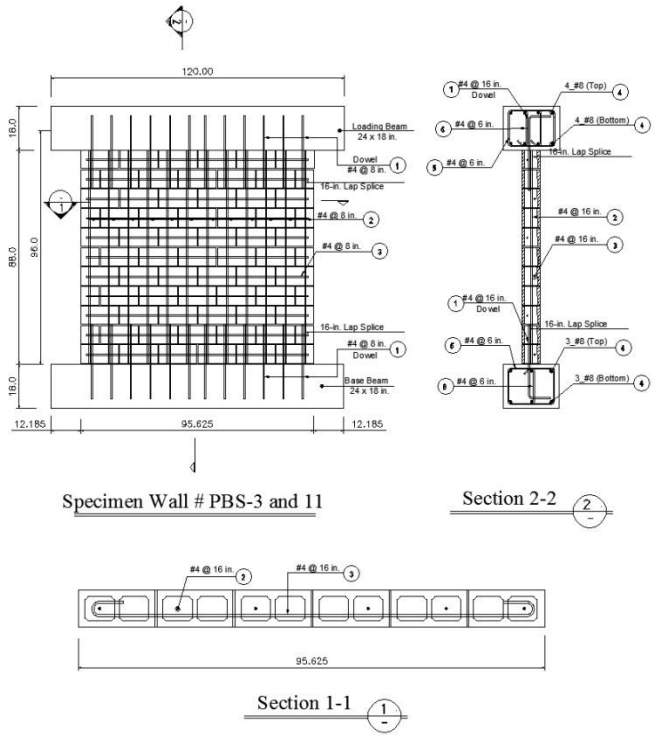

Figure 3.6 - Reinforced masonry wall UT-PBS-03 tested by Ahmadi (2012)

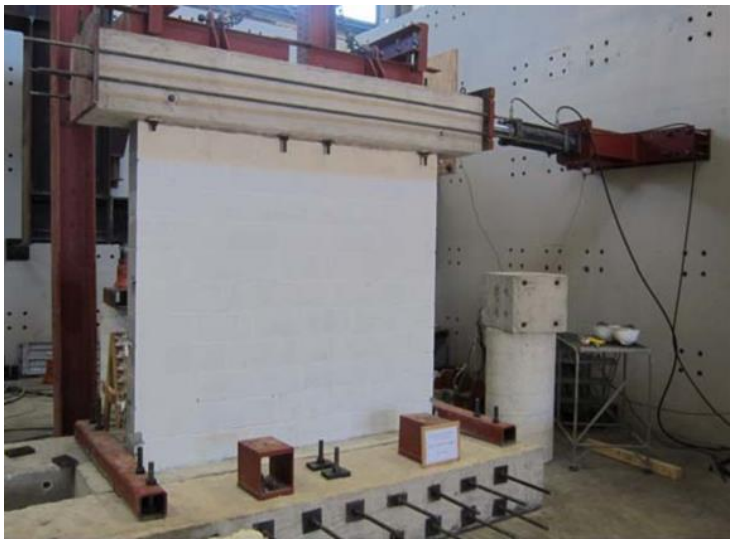

Figure 3.7 - Test setup for wall UT-PBS-03 (Ahmadi, 2012)

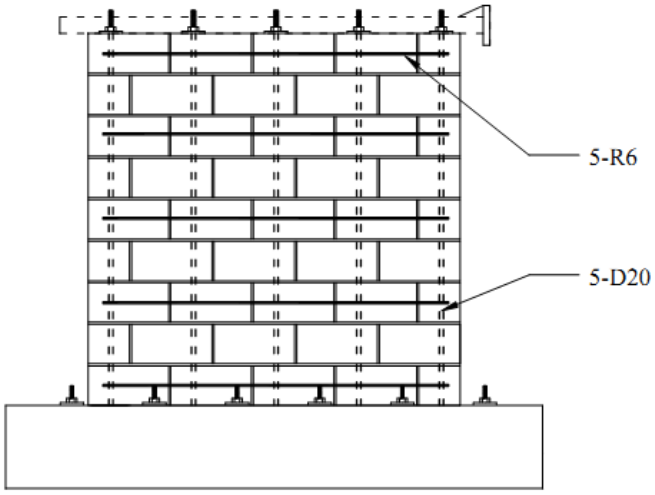

Figure 3.8 - Reinforced masonry wall A1 tested by Voon (2007)

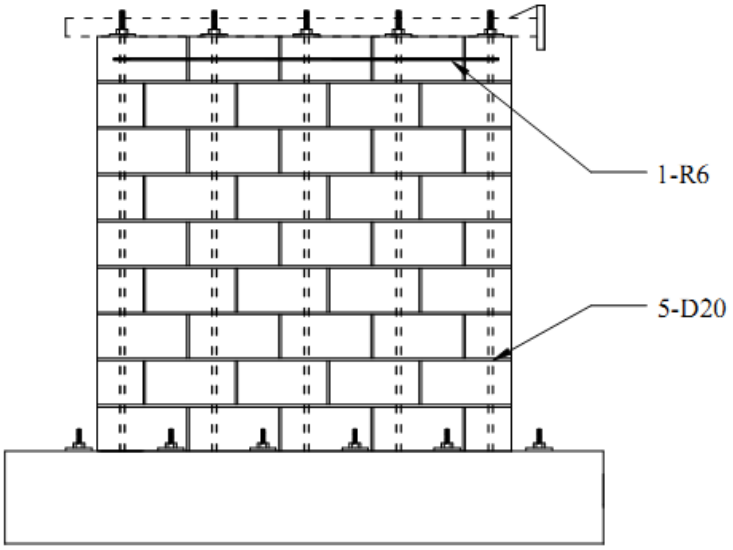

Figure 3.9 - Reinforced masonry wall A2 tested by Voon (2007)

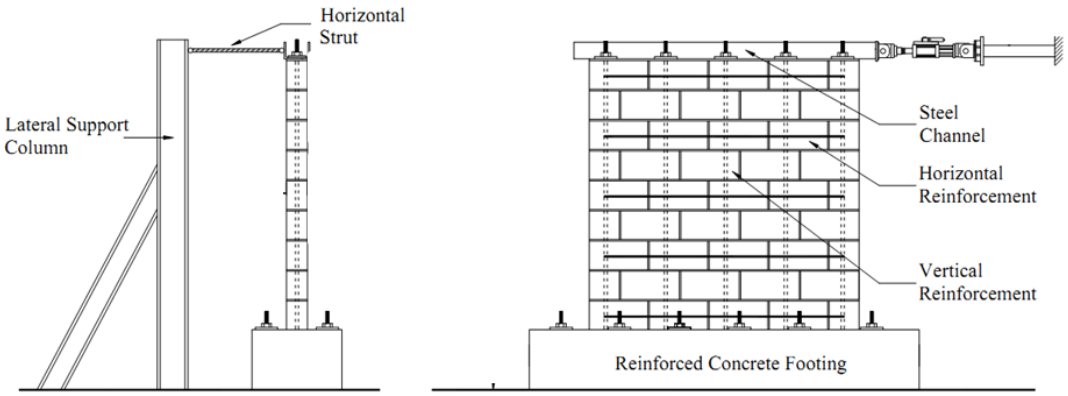

Figure 3.10 - Test setup for walls A1 and A2 (Voon, 2007)

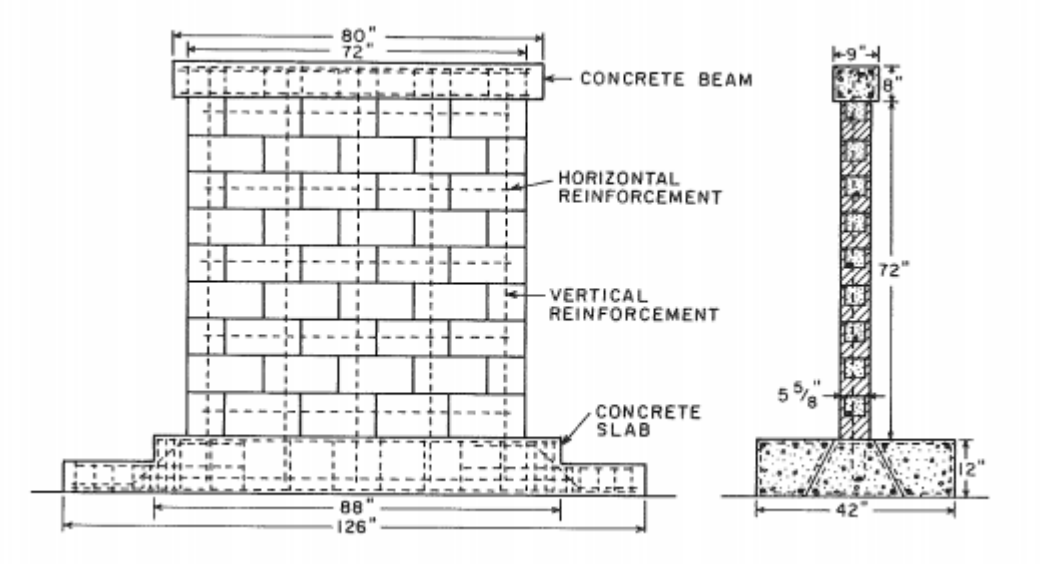

Figure 3.11 - Reinforced masonry wall Sp. 5 tested by Shing et al. (1991)

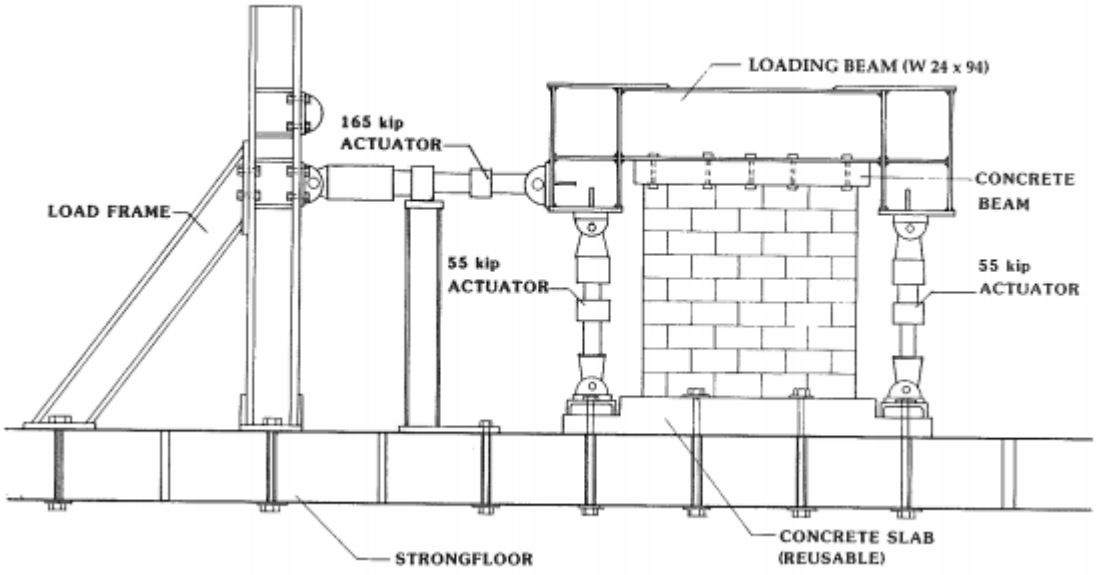

Figure 3.12 - Test setup for wall Sp. 5 (Shing et al., 1991)

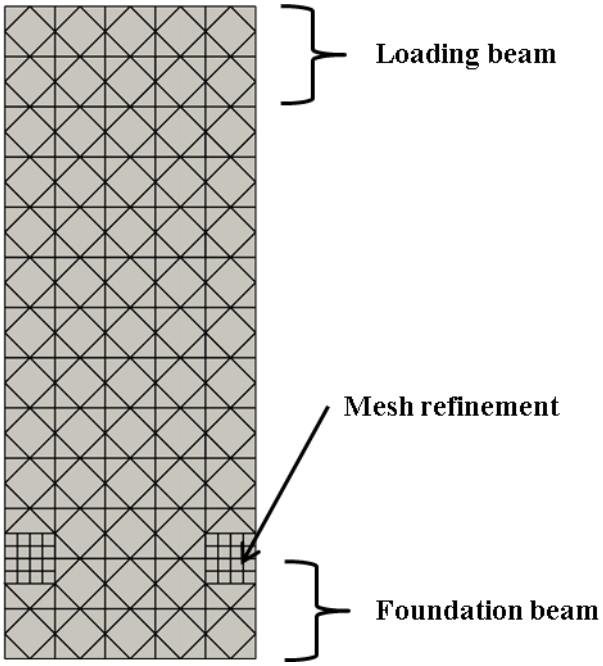

Figure 3.13 - Meshing scheme for walls C2 and C3

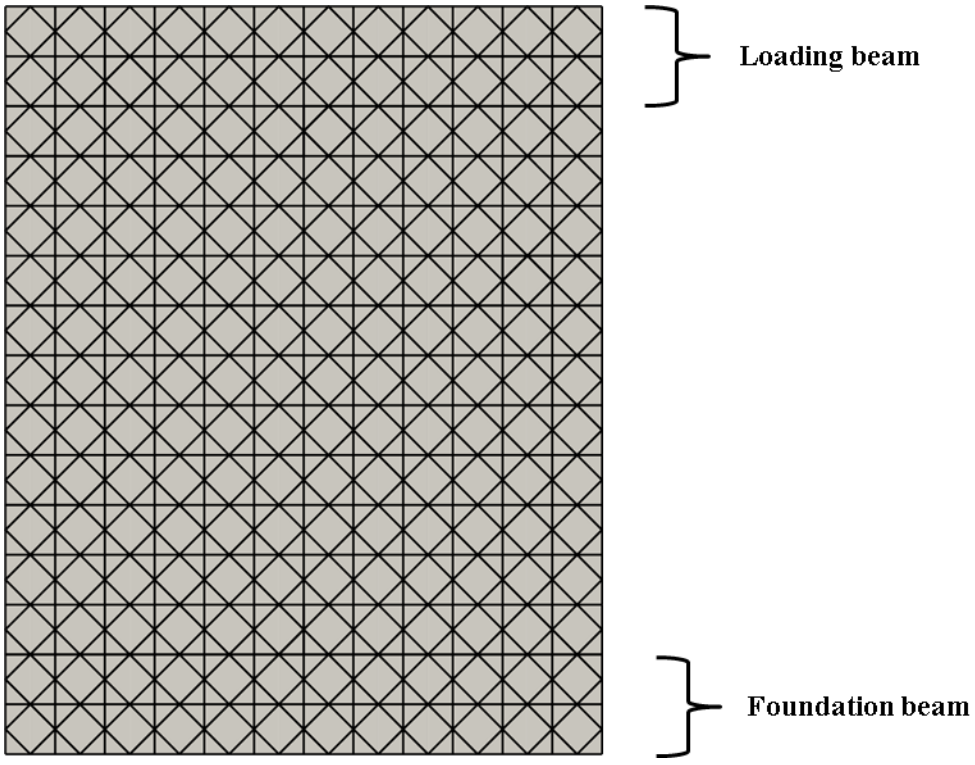

Figure 3.14 - Meshing scheme for wall UT-PBS-01

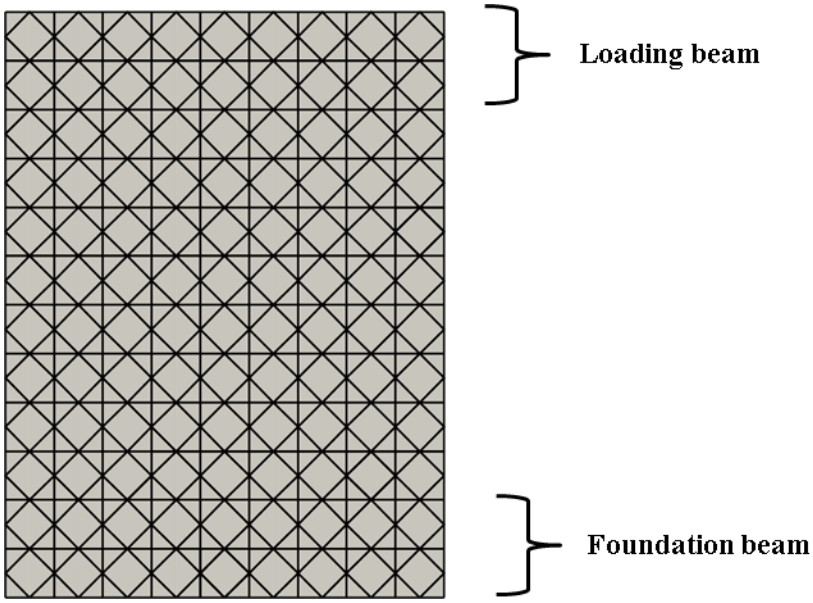

Figure 3.15 - Meshing scheme for walls A1, A2, UT-PBS-03 and Sp. 5

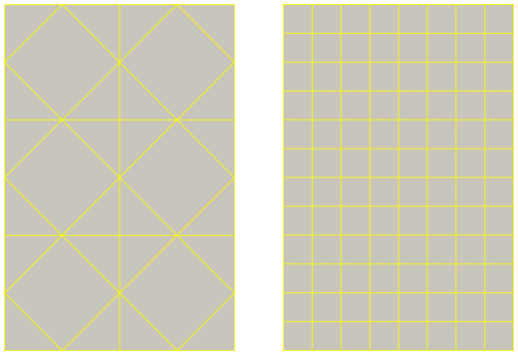

(a) (b)

Figure 3.16 - Prism test model: a) coarse mesh, b) fine mesh

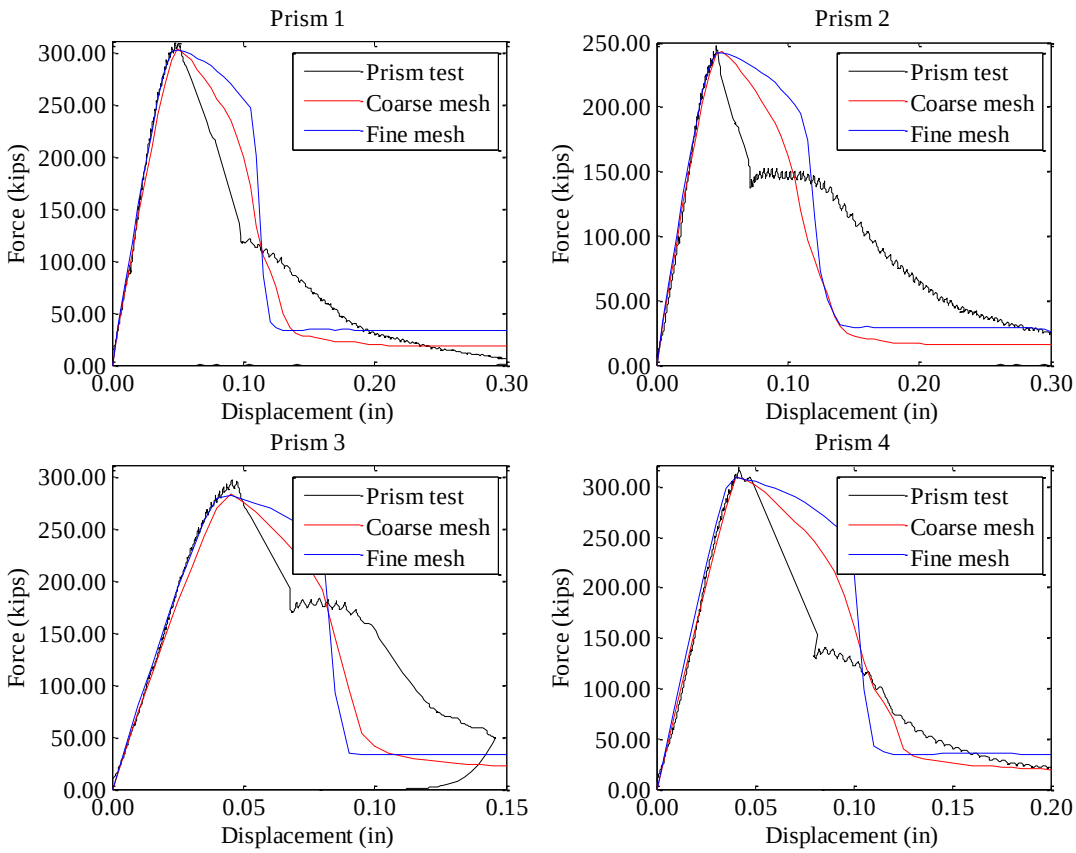

Figure 3.17 - Comparison of force-vs.-displacement curves from finite elements analyses and prism tests

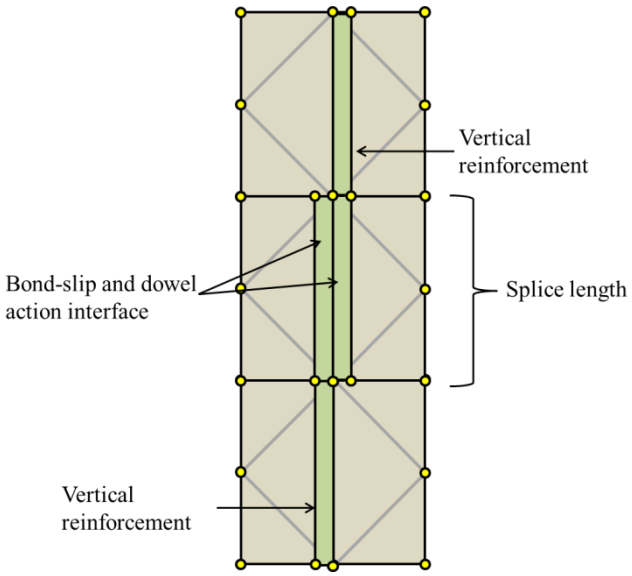

Figure 3.18 - Modeling of lap splices

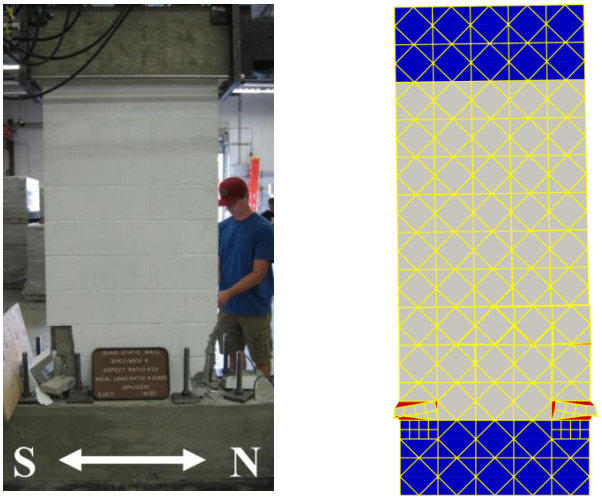

Figure 3.19 - Comparison of failure mechanisms from test and analysis for wall C2

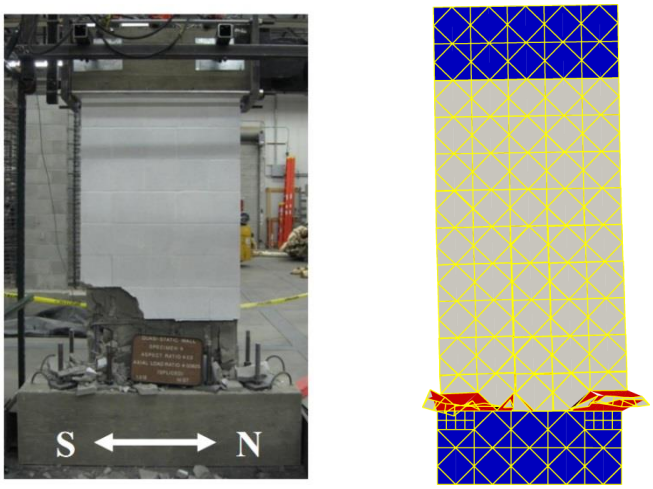

Figure 3.20 - Comparison of failure mechanisms from test and analysis for wall C3

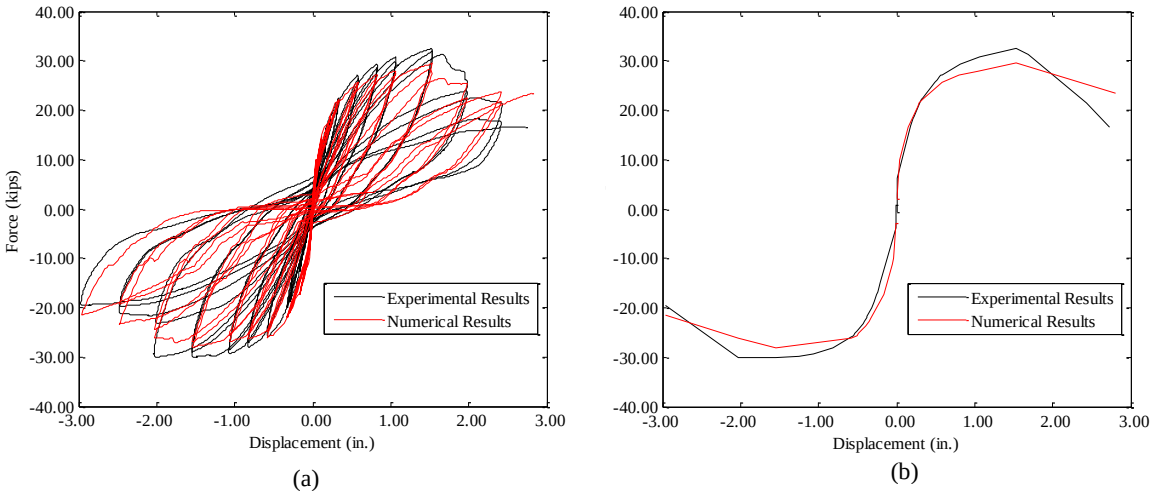

Figure 3.21 - Comparison of the force-vs.-displacement curves obtained from finite element analysis and test for wall C2: a) hysteretic curves, b) envelopes

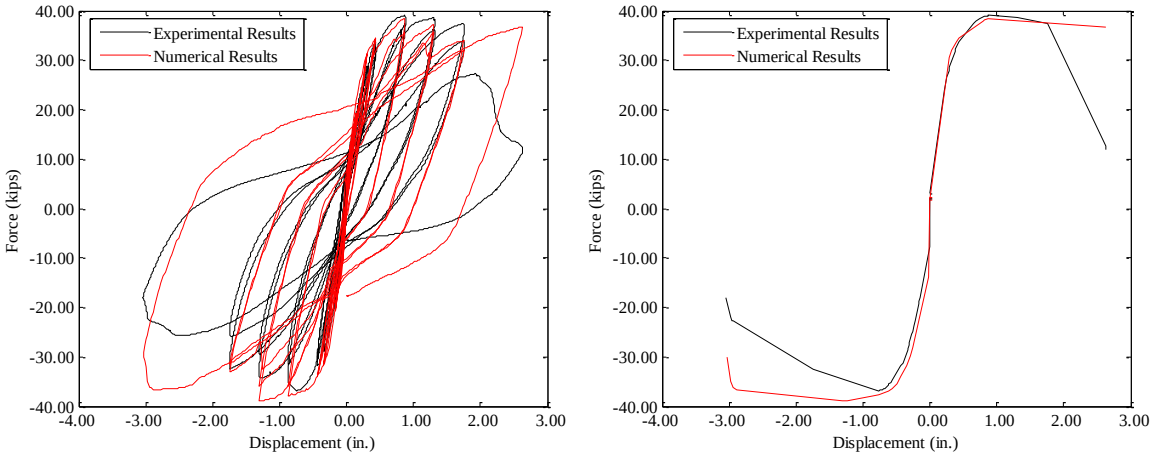

Figure 3.22 - Comparison of force-vs.-displacement curves from finite element analysis and test for wall C3: a) hysteretic curves, b) envelopes

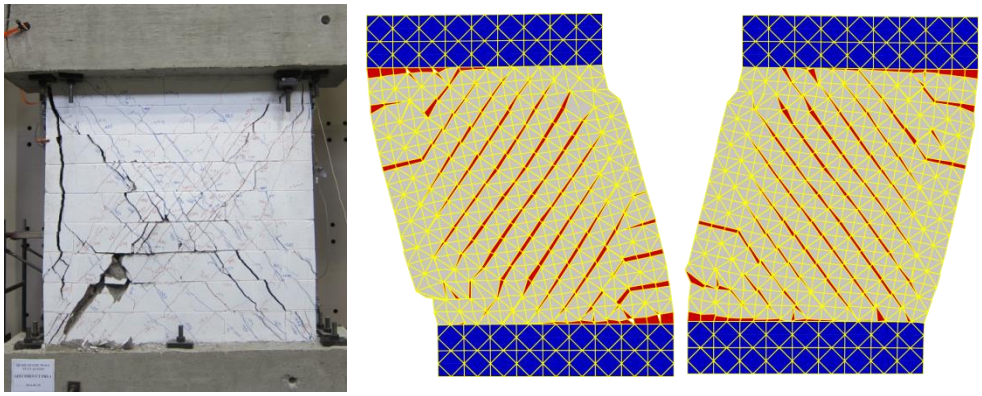

Figure 3.23 - Comparison of failure mechanisms from test and analysis for wall UT-PBS-01

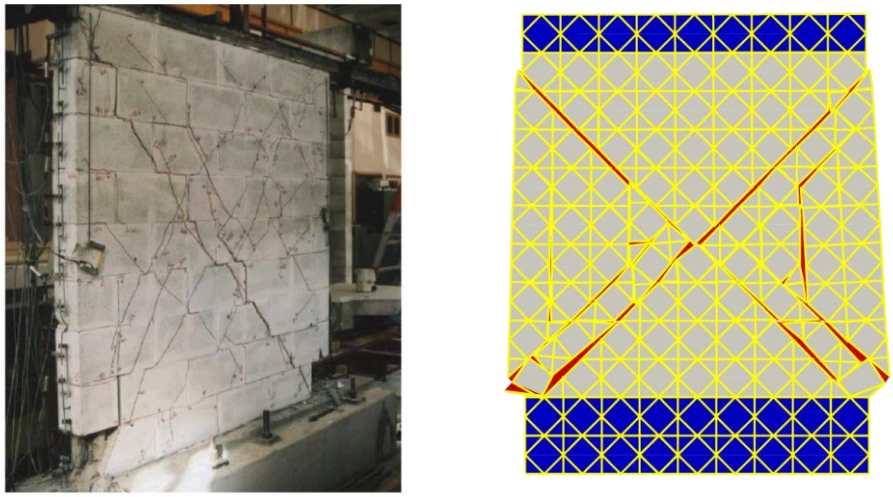

Figure 3.24 - Comparison of failure mechanisms from test and analysis for wall A1

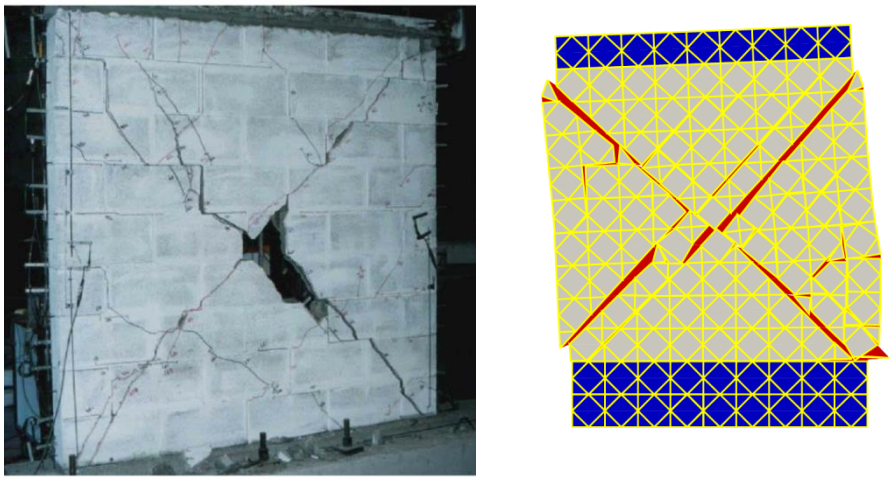

Figure 3.25 - Comparison of failure mechanisms from test and analysis for wall A2

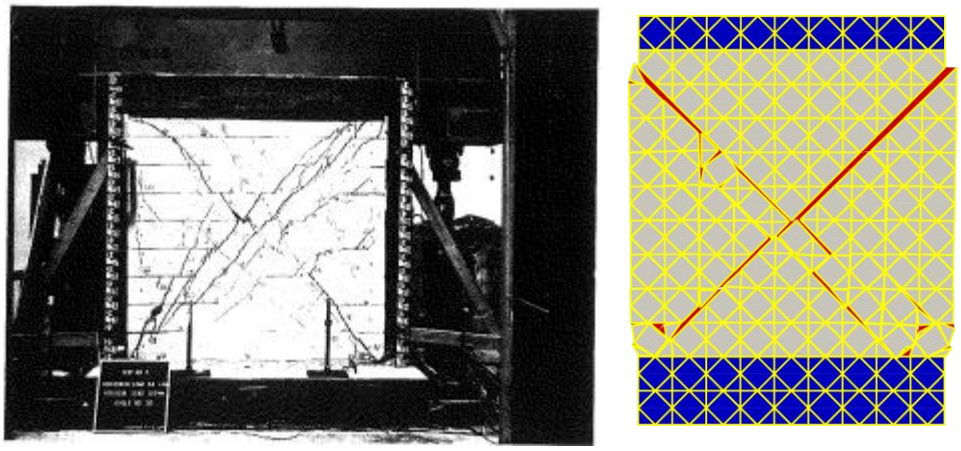

Figure 3.26 - Comparison of failure mechanisms from test and analysis for wall Sp. 5

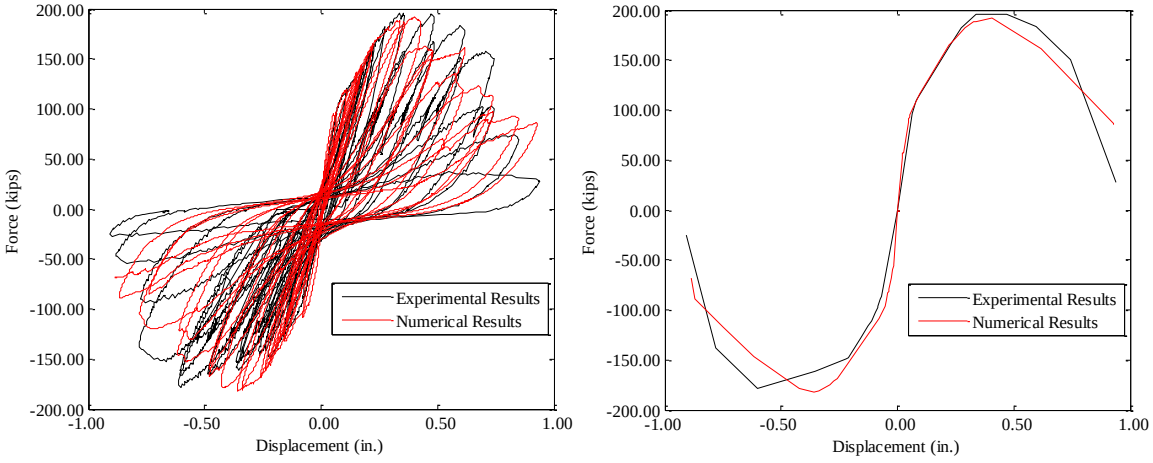

Figure 3.27 - Comparison of force-vs.-displacement curves from finite element analysis and test for wall UT-PBS-01: a) hysteretic curves, b) envelopes

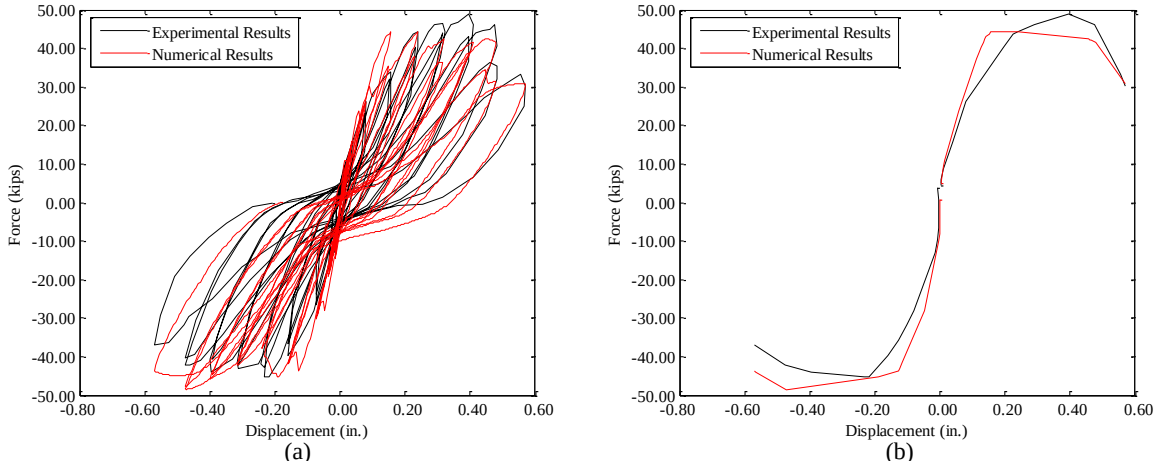

Figure 3.28 - Comparison of force-vs.-displacement curves from finite element analysis and test for wall A1: a) hysteretic curves, b) envelopes

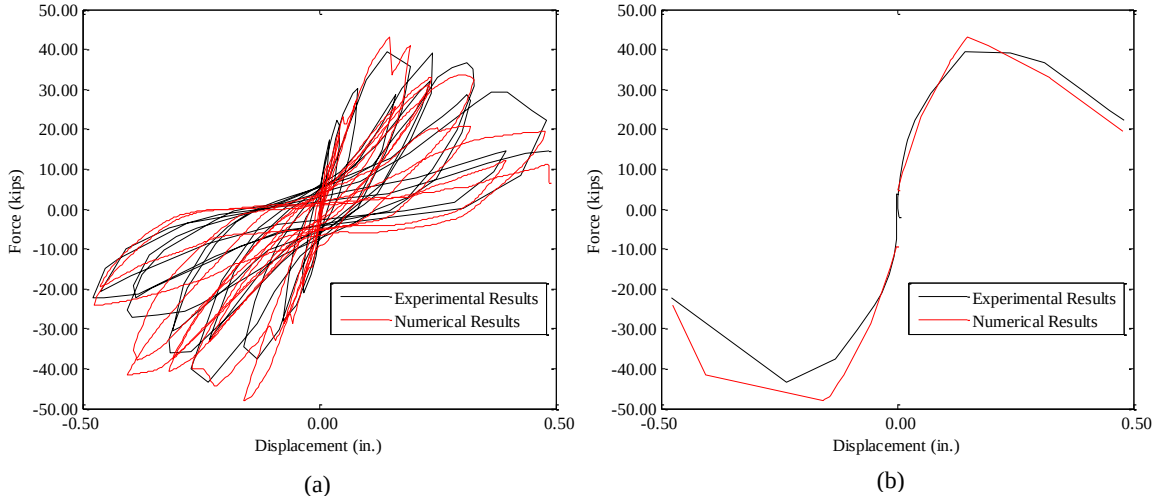

Figure 3.29 - Comparison of force-vs.-displacement curves from finite element analysis and test for wall A2: a) hysteretic curves, b) envelopes

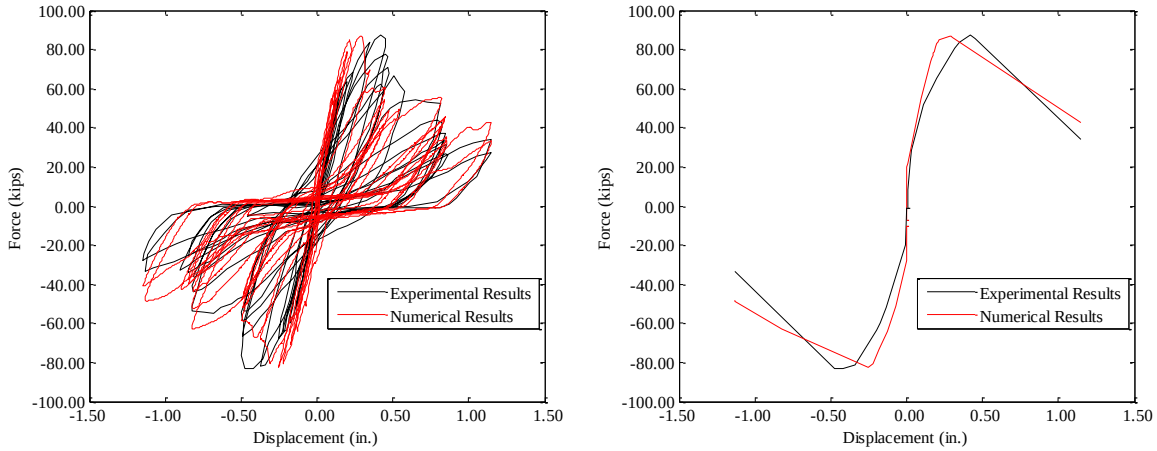

Figure 3.30 - Comparison of force-vs.-displacement curves from finite element analysis and test for wall Sp. 5: a) hysteretic curves, b) envelopes

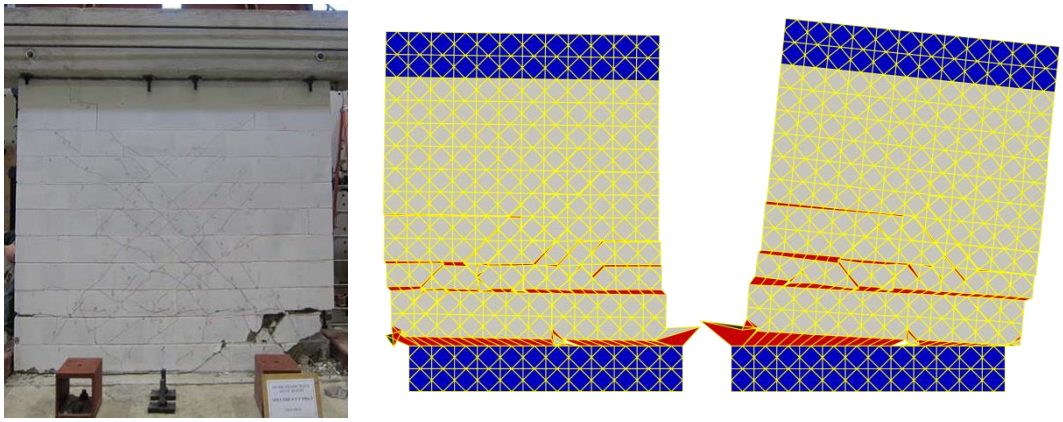

Figure 3.31 - Comparison of failure mechanisms from test and analysis for wall UT-PBS-03

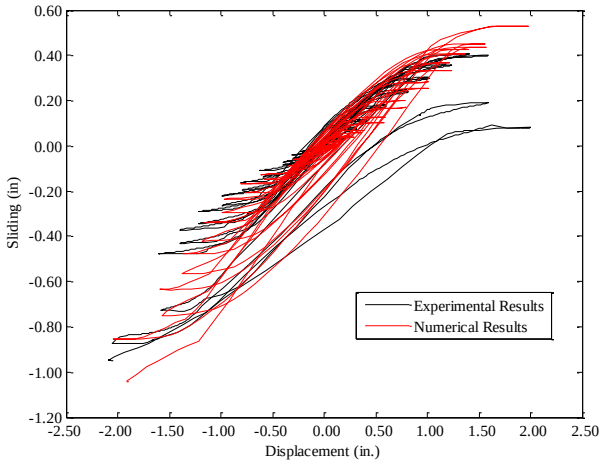

Figure 3.32 - Comparison of sliding-vs.-top lateral displacement curves from finite element analysis and test for wall UT-PBS-03

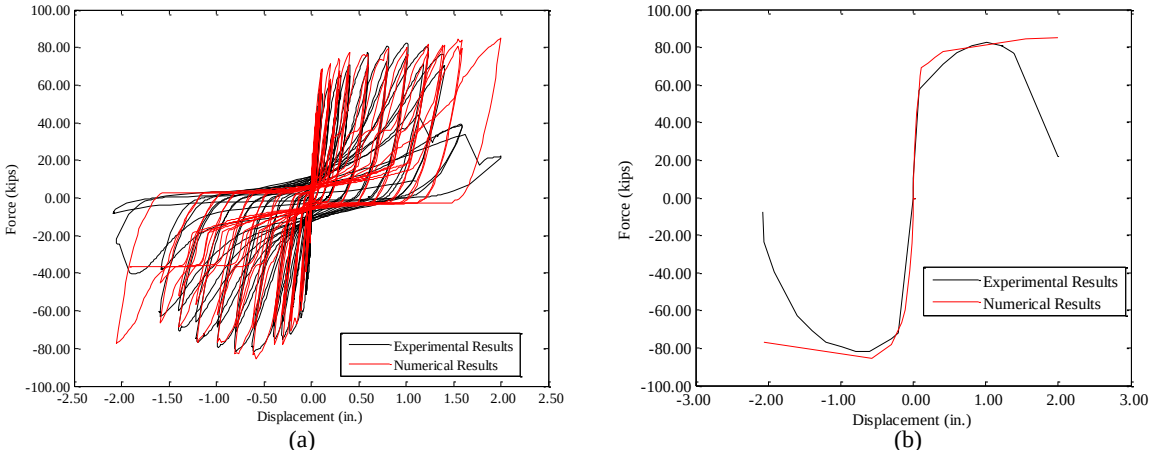

Figure 3.33 - Comparison of force-vs.-displacement curves from finite element analysis and test for wall UT-PBS-03: a) hysteretic curves, b) envelopes

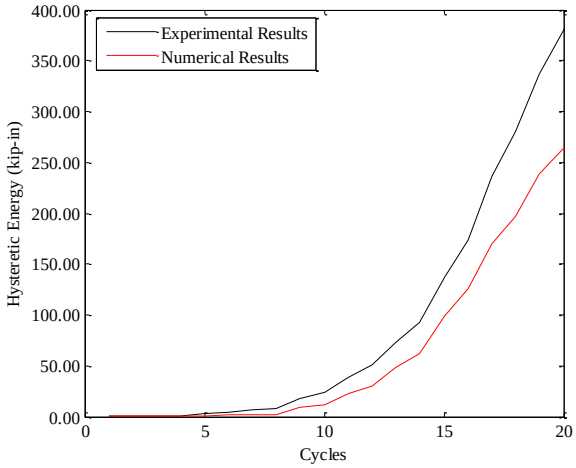

Figure 3.34 - Comparison of cumulative hysteretic energy dissipations from test and analysis for wall C2

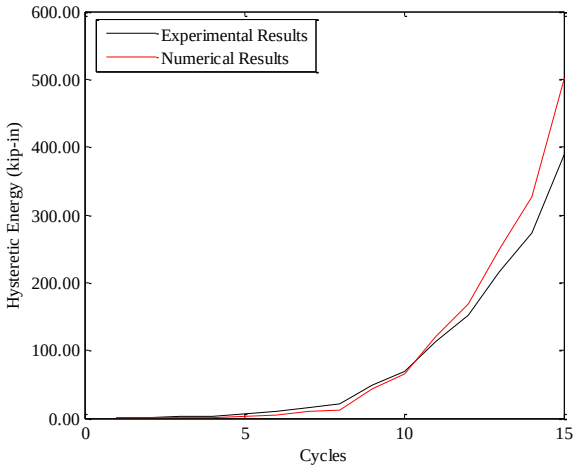

Figure 3.35 - Comparison of cumulative hysteretic energy dissipations from test and analysis for wall C3

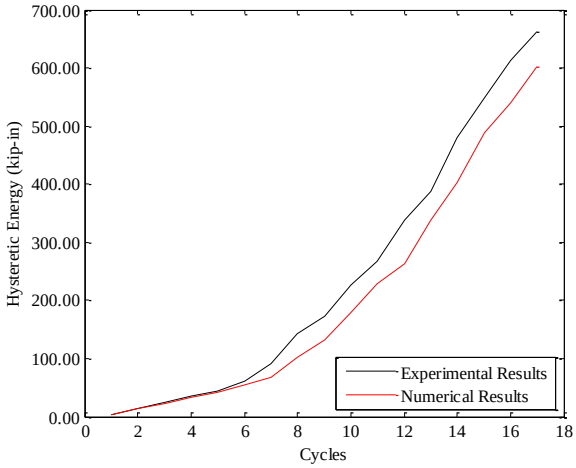

Figure 3.36 - Comparison of cumulative hysteretic energy dissipations from test and analysis for wall PBS-01

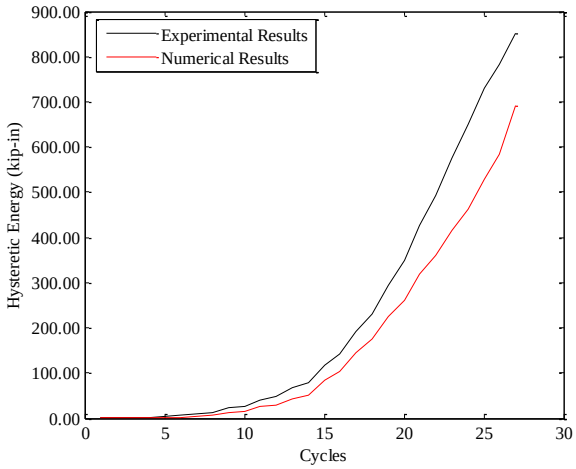

Figure 3.37 - Comparison of cumulative hysteretic energy dissipations from test and analysis for wall PBS-03

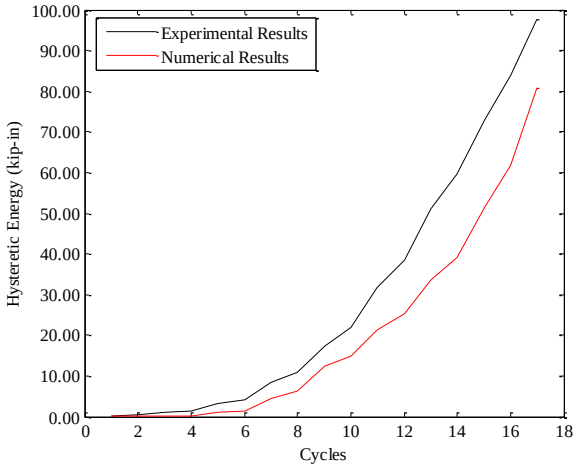

Figure 3.38 - Comparison of cumulative hysteretic energy dissipations from test and analysis for wall A1

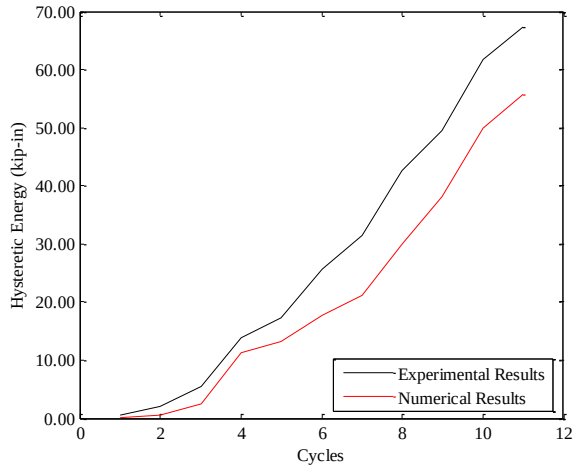

Figure 3.39 - Comparison of cumulative hysteretic energy dissipations from test and analysis for wall A2

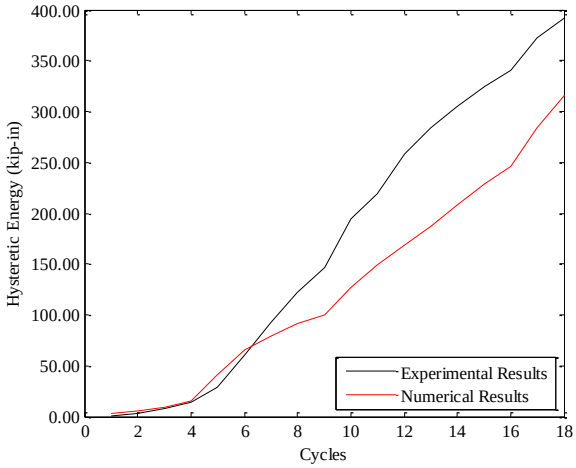

Figure 3.40 - Comparison of cumulative hysteretic energy dissipations from test and analysis for wall Sp. 5

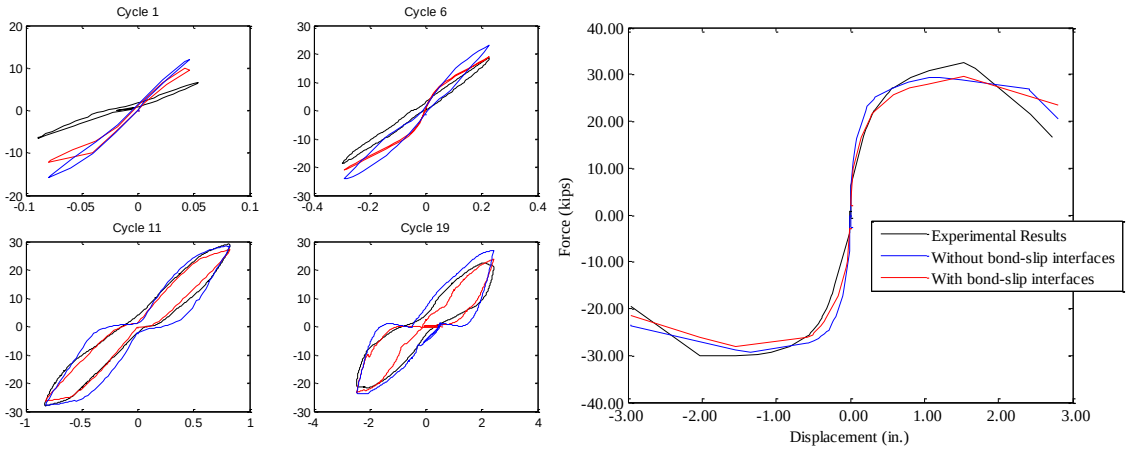

Figure 3.41 - Influence of bond-slip and dowel action interface elements on numerical results for wall C2: a) selected force-displacement hysteretic curves, b) force-vs.-displacement envelopes

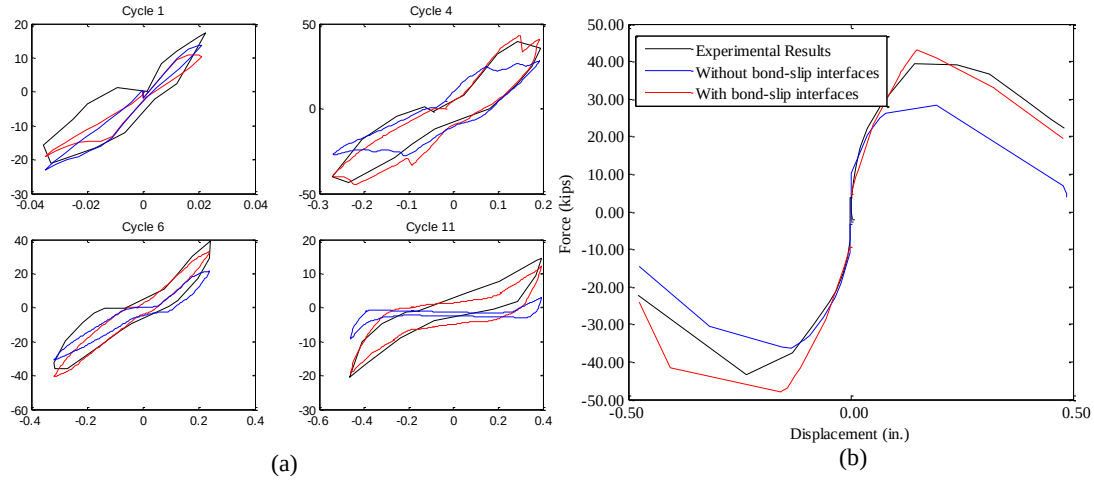

Figure 3.42 - Influence of bond-slip and dowel action interface elements on numerical results for wall A2: a) selected force-displacement hysteretic curves, b) force-vs.-displacement envelopes

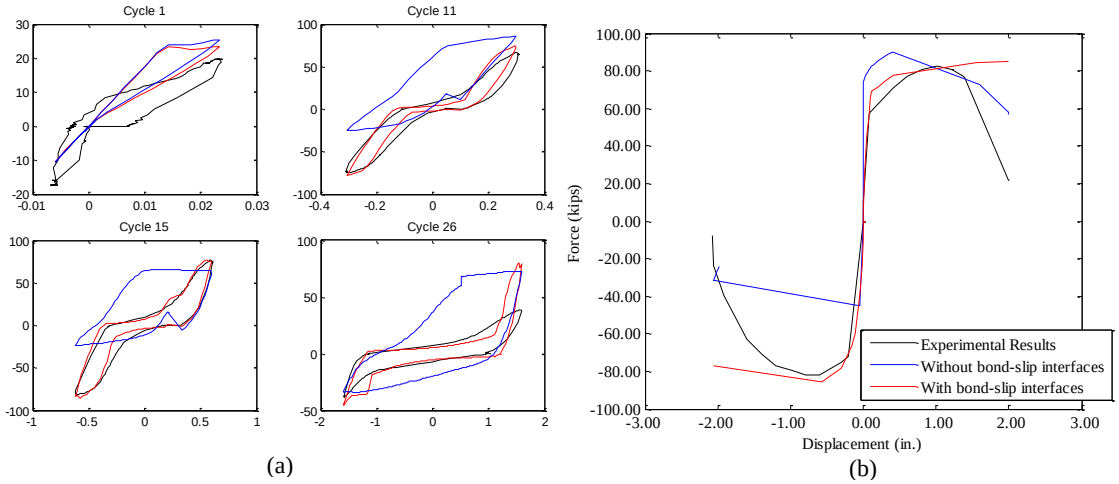

Figure 3.43 - Influence of bond-slip and dowel action interface elements on numerical results for wall UT-PBS-03: a) selected force-vs.-displacement hysteretic curves, b) force-vs.-displacement envelopes

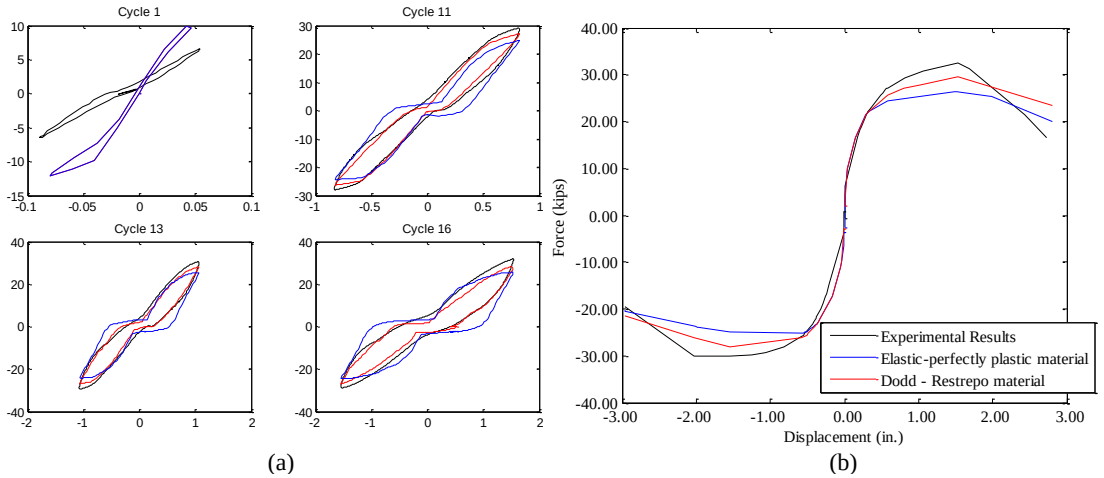

Figure 3.44 - Influence of steel material behavior on numerical results for wall C2: a) selected force-vs.-displacement hysteretic curves, b) force-vs.-displacement envelopes

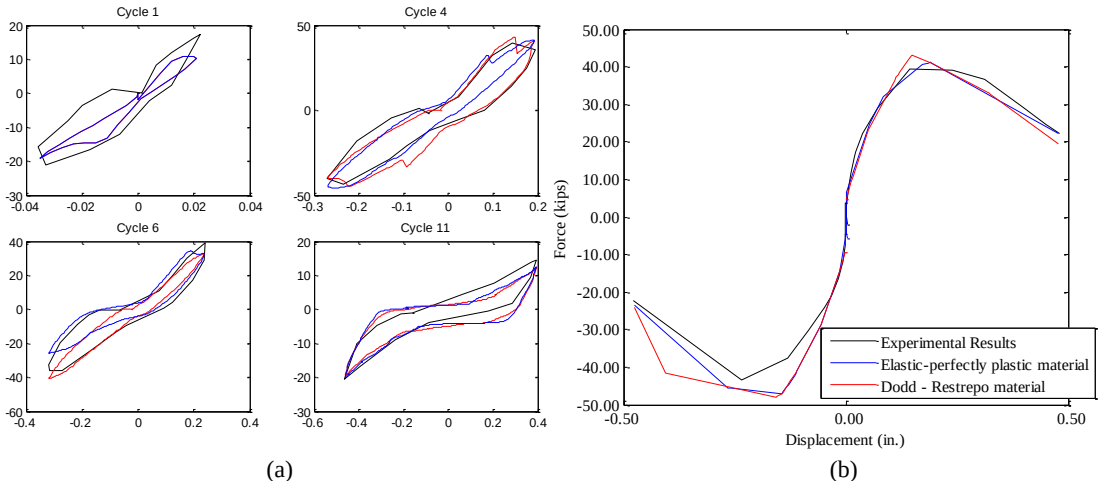

Figure 3.45 - Influence of steel material behavior on numerical results for wall A2: a) selected force-vs.-displacement hysteretic curves, b) force-vs.-displacement envelopes

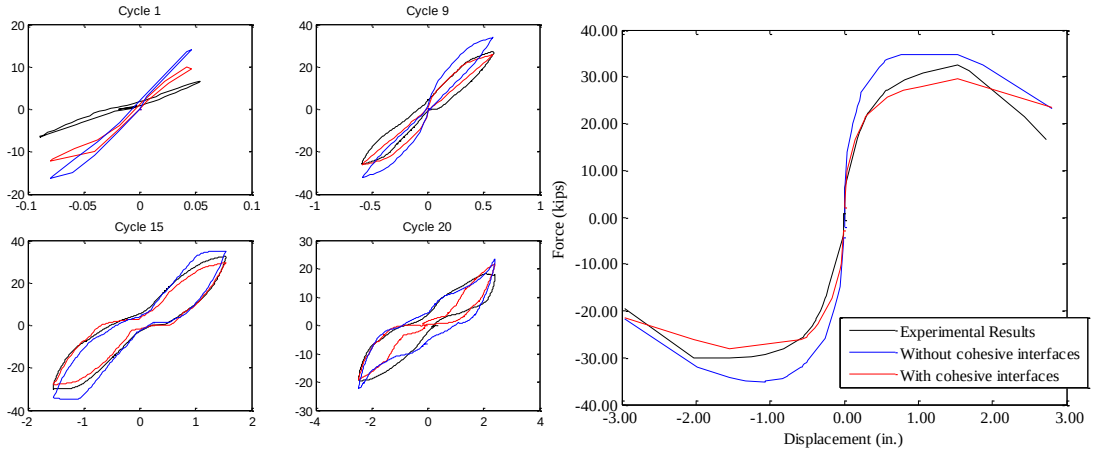

Figure 3.46 - Influence of cohesive interface elements on numerical results for wall C2: a) selected force-vs.-displacement hysteretic curves, b) force-vs.-displacement envelopes

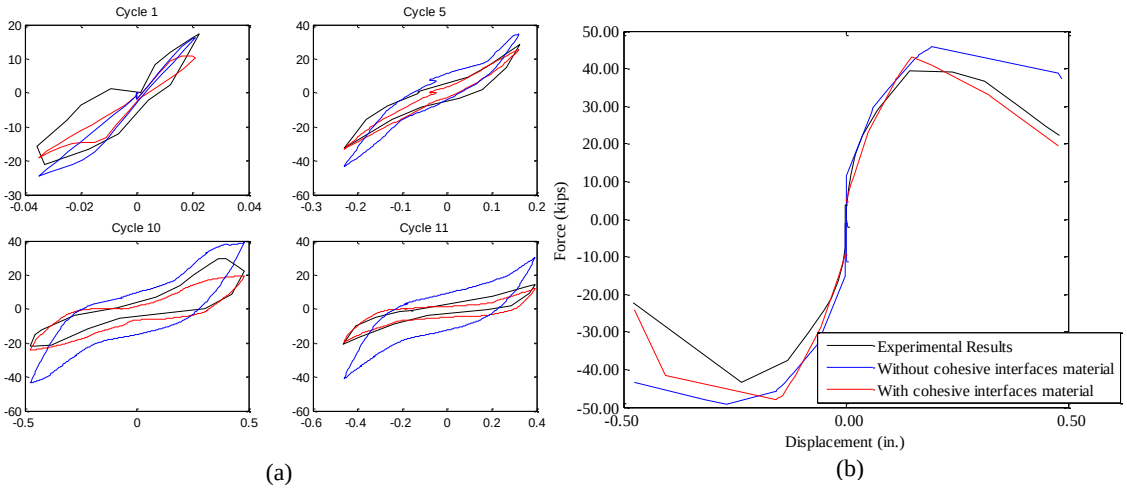

Figure 3.47 - Influence of cohesive interface elements on numerical results for wall A2: a) selected force-vs.-displacement hysteretic curves, b) force-vs.-displacement envelopes

4. SHAKE – TABLE TESTS OF A TWO – STORY STRUCTURE

This chapter presents detailed results and findings from the shake-table tests conducted on a full-scale, two-story, reinforced masonry shear-wall structure designed by a displacement-based method (Ahmadi et al. 2013a, 2013b). The test structure had two T-sectioned and one rectangular-sectioned wall components along the direction of the table motion, and four rectangular-sectioned wall components in the orthogonal direction. The structure was subjected to a series of dynamic tests with a historical ground motion record scaled to intensity levels up to that of the maximum considered earthquake (MCE). The structure formed a soft-story mechanism during the last test. The recorded displacements were within the target limits for the design earthquake-level table motion but exceeded the target limits for the MCE level. Although the structure experienced severe damage and incurred diagonal cracking in wall components with low aspect ratios, it did not collapse.

Besides the validation of the displacement-based design method, the shake-table tests provided useful information on the behavior of a shear-dominated reinforced masonry wall structure under dynamic loading, and in particular, the system-level ductility capacity and strength, the influence of the walls orthogonal to the direction of shaking, the evolution of structural damage, and the final failure mechanism. This chapter also compares the displacement-based design to code-based design to illustrate the shortcoming of the latter.

Small-scale shake-table tests and large-scale quasi-static tests have been conducted on reinforced masonry wall systems by a number of researchers. For example,

Abrams and Paulson (1991) studied the performance of two ¼-scale, three-story, reinforced masonry buildings with shake-table tests, including the distribution of story shear to individual piers. Leiva and Klingner (1991) tested quasi-statically six full-scale, low-rise, reinforced masonry shear wall structures with openings to examine the influence of wall openings and floor diaphragms on the in-plane seismic resistance of these walls. Later, Seible et al. (1994a, 1994b) tested a full-scale, five-story reinforced masonry building with the pseudo-dynamic method to examine the influence of wall flanges and floor diaphragms on the seismic performance. Nevertheless, structures examined in these studies were designed with a force-based approach and had wall geometries and reinforcement inductive to flexure-dominated behavior, which is not always achievable for perforated walls. The performance of shear-dominated wall segments was studied by Shing et al. (1989) and Voon et al. (2006). Both studies have shown that while the shear strength of a wall will increase with the increase of axial load, its shear deformation capacity will decrease. Nevertheless, little studies have been conducted on the performance of a wall system with shear-dominated wall components. Shake-table tests conducted by Wight et al. (2007) on posttensioned masonry walls with openings have shown that the behavior of a three-dimensional wall system is more complicated than that of a planar wall in that the former can have the uplift of out-of-plane walls due to the rocking of in-plane walls.

The study reported here focused on the performance of a full-scale three-dimensional reinforced masonry structure that was designed with a displacement-based approach and had shear-critical wall components. The test data presented allow a better understanding of the influence of out-of-plane walls on the performance of a wall system.

4.1. Specimen design

The full-scale reinforced masonry structure tested on the shake table represented a segment of a two-story prototype building with a configuration representative of a typical commercial or school building. The building has masonry load-bearing walls and reinforced concrete columns to carry gravity loads, but only the masonry walls resist seismic forces. The tributary seismic mass for the test structure was 1.7 times the gravity mass.

The plan view and elevation view of the test structure are presented in Figure 4.1 and Figure 4.2. The structure was subjected to unidirectional table motions. The interior wall, which was parallel to the direction of table motion, had one window opening and one door opening in each story (Figure 4.2a), while each of the two exterior walls had two door openings in each story (Figure 4.2b). For each story, wall components separated by openings are identified as W-1 through W-9, as shown in Figure 4.1. With respect to the direction of the seismic force induced by the table, wall components W-1 and W-5 formed the web and the flange of a T-wall, and the same is true for W-3 and W-8. Wall components W-2, W-4, W-6, W-7, and W-9 had rectangular sections. For the convenience of discussion in this chapter, W-1 and W-3 denote the entire T-walls that included W-5 and W-8.

The structure was assigned to Seismic Design Category (SDC) D with a hazard level corresponding to the San Diego area. It was designed with a displacement-based method and had reinforcement details satisfying the limit design requirements of Appendix C of the 2013 MSJC Code (MSJC 2013), but not all the prescriptive

requirements for special walls in Chapter 7 of the code. The displacement response spectrum used for the design was obtained from the pseudo-spectral acceleration determined in accordance with ASCE/SEI 7-10 (ASCE 2010) for the targeted hazard level The spectral acceleration values at short period (S_{DS}) and at 1-sec period (S_{D1}) were 1.0g and 0.6g, respectively. The tributary seismic weights of the 1st story and the roof were 124 and 104 kips, respectively.

Wall components W-2 and W-3 in this structure were expected to be shear-dominated. Hence, the maximum allowable drift at each story was limited to 0.3% of the story height for the Design Earthquake (DE) and 0.6% for the Maximum Considered Earthquake (MCE), which approximately corresponded to local drift ratios of 0.5% and 1.0% with respect to the clear height of wall components W-2 and W-3. These displacement limits were based on data obtained from quasi-static tests conducted on shear-dominated wall segments as reported in Ahmadi (2012) and are consistent with the data of Voon et al. (2006). The detailed design procedure and considerations for the 2-story specimen are given in Ahmadi et al. (2013a and 2013b). As shown in Figure 4.3 and Figure 4.4, all the walls had No. 4 bars spaced at 16 in. (406.4 mm) on center for the vertical and horizontal reinforcement. However, the vertical bars in the flanges of W-1 and W-3 had a spacing of 8 in. (203.2 mm). This corresponds to a reinforcement ratio of 0.22% for W-1 and W-3, and 0.15% for W-2. The bar spacing for all walls except the flanges of W-1 and W-3 exceeded the maximum spacing of 13.3 in. (337.8 mm) (which is 1/3 of the wall length in this case) that is allowed by the prescriptive requirements in the code. However, the quantities of vertical and horizontal reinforcement did exceed 0.1% of the gross cross-sectional areas of the walls, which is the minimum amount

required by the Limit Design Method in Appendix C of the MSJC Code for shear-dominated wall components whose deformation may reach 0.5% of the component length. The vertical bars had 16-in. (406.4 mm) lap splices at the wall base in each story. Control joints were introduced on both sides of each door opening at the ends of the lintel. The horizontal reinforcing bars in the lintel were debonded over a length of 16 in. (406.4 mm) on each side of a control joint to reduce the coupling action on the vertical wall components. As discussed later in this chapter, the amount of reinforcement in this structure was higher than what would have been needed if it were designed with the conventional force-based approach.

The walls were constructed of 8 x 8 x 16-in. (203.2 x 203.2 x 406.4-mm) double open-end hollow concrete masonry units (except for the end units and bond-beam units in the lintels) conforming to ASTM C90 specifications, Type S cement-lime mortar, coarse grout with a specified compressive strength of 2.5 ksi (17.24 MPa), and ASTM A615 Grade 60 steel reinforcement. The floor and roof diaphragms had 6 precast, prestressed, 8-in. (203.2-mm) thick, hollow-core concrete planks covered with 3-in. (76.2 mm) cast-in-place concrete toping reinforced with Grade 60 No. 4 bars at 16-in. (406.4 mm) on center in each direction. The planks were 22-ft. (6.71-m) long and 40-in. (1016 mm) wide, and were supported on the exterior walls. The diaphragms were connected to the interior and exterior walls with L-shaped tie bars. The gravity mass was accurately represented in the test structure, but not the seismic mass. The missing seismic mass was accounted for in the tests by scaling up the ground acceleration with a factor of 1.7 and compressing the time by a factor of 0.77. The scaling factors used to satisfy dynamic similitude requirements are presented in Table 5.1.

4.2. Test setup and instrumentation scheme

4.2.1. Test setup

The test structure is shown in Figure 4.5. The shake table moved in the east-west direction, and the structure was oriented so that the interior wall was parallel to the direction of shaking. The door openings in the wall were on the west side and the window openings on the east. Steel towers, not in contact with the structure, were placed on the east and west sides and fitted with cables to prevent the structure from collapsing on the shake table. The footing of the structure was attached to the table platen with post-tensioned rods. The construction of the 2-story specimen took four weeks, and material samples (mortar cylinders, grout cylinders and grout prisms) and masonry prisms were prepared during construction.

4.2.2. Instrumentation

A total of 409 sensors, including strain gages, linear potentiometers, string potentiometers, and accelerometers, were mounted on the specimen to measure strains in the reinforcing bars, and displacements and accelerations of the structure at various locations. Moreover, 12 video cameras were deployed to record the behavior of the structure during shaking. Figure 4.6 shows the locations and directions of the accelerometers located on each floor. Accelerometers were also mounted on the footing with a similar scheme but a smaller number. Strain gages were installed on the reinforcing bars at locations where yielding could occur. The locations of the strain gages are shown in detail later when the strain data are discussed (see Figure 4.21and Figure 4.22). Most of the strain gages were installed on the vertical bars at locations near the top

and bottom of the first story. Furthermore, some of the horizontal bars in wall components W-1, W-2, and W-3, which would be subjected to in-plane shaking, were instrumented with strain gages at locations close to potential diagonal cracks. The locations and orientations of the linear potentiometers and string potentiometers mounted on the interior wall are shown in Figure 4.7. They were used to measure story drifts; possible sliding along bed joints in the wall components next to the top and bottom of the openings, and between the wall and the footing; and the opening of the control joints above the door in the bottom story. Drift at each story, defined as the relative displacement between two adjacent floors, was measured by a string potentiometer mounted on a very stiff aluminum frame that was secured on the footing or floor slab. Linear potentiometers were also used to obtain readings that would be used to calculate the shear and flexural deformations of the wall components. String potentiometers were mounted to measure the axial deformation of the exterior walls. The sign convention for the accelerations and displacements is defined according to the X-Y-Z coordinate system shown in Figure 4.6 and Figure 4.7.

4.2.3. Material properties

Compression tests were conducted on 3 x 6-in. (76.2 x 152.4-mm) mortar cylinders, 6 x 12-in. (152.4 x 304.8- mm) grout cylinders, 8 x 4 x 4-in. (203.2 x 101.6 x 101.6- mm) grout prisms, and three-course grouted concrete masonry unit (CMU) prisms prepared during the construction of the test structure. The compression tests were conducted 28 days after the material samples were prepared. Additional tests were conducted on three masonry prisms on the day the test structure was subjected to the first

design earthquake (DE). Table 4.2 and Table 4.3 summarize the compressive strengths and other important properties of the material samples. The properties of the reinforcing bars obtained by tension tests are presented in Table 4.4

4.3. Ground motion and testing sequence

4.3.1. Ground motion

The El Centro station (USGS Station 952) record obtained in the 1979 Imperial Valley Earthquake was selected for the shake-table tests. This ground motion was selected because the shape of its acceleration response spectrum resembles the design spectrum for the period range of 0 to 0.25 sec. Furthermore, this record only needs to be scaled by a factor of 85% to match the design spectral acceleration at the fundamental period of the intact structure. As shown in Figure 4.8, the original unscaled record has peak ground acceleration (PGA) of 0.51g. The motion was scaled in time and amplitude to satisfy dynamic similitude requirements with the scale factors shown in Table 5.1.

4.3.2. Testing sequence and base excitation intensity

The structure was subjected to a series of 17 dynamic tests over 5 days. The tests included 9 earthquake ground motion tests using scaled El Centro records of increasing intensity and 8 white-noise excitation tests to identify the dynamic properties of the structure before and after each earthquake ground motion test. The white-noise excitation had a root-mean-square (RMS) acceleration of 0.03 g. All the motions were unidirectional. Table 4.5 summarizes the sequence of the applied earthquake records, including the acceleration scaling of the input records, the actual PGA measured at the

footing of the structure, the fundamental period of the test structure obtained by the white-noise test (which is not listed) before each earthquake motion test, and the corresponding period of the prototype structure obtained from the time scale factor. The acceleration scaling of the input records shown in the table was applied to the original record that had been scaled in time and amplitude to meet the dynamic similitude requirements.

Figure 4.9 shows the response spectra (with 5% damping) of the ground motions recorded by the accelerometers located on the footing of the test structure together with the spectra of the design earthquake (DE) and maximum considered earthquake (MCE). The El Centro 30% and 43% shown in the figure represent the last motions at these levels. As shown in the figure, based on the fundamental period of the structure measured right before each test, the records with the acceleration scaled to 30%, 43% and 86% of the original record are below the DE level, 108% of the El Centro is at the DE level, 145% of the El Centro is between the DE and MCE levels, and 160% is at the MCE level. In all cases, the actual table motion recorded was not exactly the same as the input motion because of table-structure interaction.

4.4. Test observations

4.4.1. Low-level tests

In the first phase, six tests with ground motions below the design earthquake level were conducted. The input accelerations were scaled to 30%, 43%, and 86% of the 1979 El Centro record, respectively. The initial fundamental period of the structure was 0.077 sec, as identified from a white-noise excitation test, and it changed to 0.084 sec after the

last run at the 43% level. This change could be caused by the development of micro-cracks in the walls. The maximum recorded drifts of the first and second stories were 0.036 in. (0.91 mm) and 0.021 in. (0.53 mm), respectively. These values correspond to drift ratios (relative displacement between the top and bottom of a story divided by the story height) of 0.04% and 0.02%. After the structure had been subjected to the 86% level motion, a few fine cracks were observed at the control joints of wall components W-1 and W-2. Furthermore, flexural cracks were visible at the top and bottom of W-2, and diagonal cracks radiated from the two bottom corners of the window opening, as shown in Figure 4.10. The period of the structure changed to 0.090 sec. During this test, the maximum drifts of the first and second stories were 0.131 in. (3.33 mm) and 0.066 in. (1.68 mm), respectively. These values correspond to drift ratios of 0.14% and 0.07%.

4.4.2. DE level test

One test was conducted with 108% of the El Centro motion, which corresponds to the design earthquake, as shown in Figure 4.9. The new cracks that developed were simply extensions of those developed during the 86% El Centro, as shown Figure 4.11. Both the length and width of the cracks increased. Hairline cracks were observed at the second story in wall components W-2 and W-3 close to the window corners. The fundamental period of the structure increased to 0.113 sec after this test. The maximum drifts of the first and second stories during the 108% El Centro were 0.206 in. (5.23 mm) and 0.084 in. (2.13 mm), respectively. These values correspond to drift ratios of 0.21% and 0.09%. After this test, the structure could be considered still operational and the damage easily reparable.

4.4.3. Between DE and MCE level test

The first ground motion that was above the DE level but below the MCE level was the 145% El Centro. During this test, significant damage occurred to the structure. The existing cracks propagated further, the widths of the cracks increased, and diagonal shear cracks were observed in wall components W-1 and W-3, as shown in Figure 4.12. One shear crack propagated below W-2 from the window corner. Sliding became a little more severe at the base of W-1 and top W-2 (see Table 4.6), and flexural cracks became more obvious in the flanges of W-1 and W-3. Horizontal cracks appeared at the top of all the exterior walls orthogonal to the direction of shaking. Minor cracks developed at the second story close to the window corners, at the control joints, and at the top of W-1 and W-2. The period of the structure changed to 0.218 sec after this test. The maximum drifts of the first and second stories were 0.404 in. (10.26 mm) and 0.219 in. (5.56 mm), respectively, occurring in the negative direction, while for the previous motions, they were in the positive direction. They correspond to drift ratios of 0.42% and 0.23%.

4.4.4. MCE level test

The response spectra of the table motions corresponding to the 145% and 160% El Centro, as shown in Figure 4.9, look similar in spite of the different magnitude scaling of the input record. This is due to the table-structure interaction, which was affected by the nonlinearity of the test structure. Nevertheless, because of the significant shift of the fundamental period of the structure after the 145% El Centro as damage increased, the last test with the 160% El Centro had the spectral intensity of the MCE at the shifted period, as shown in Figure 4.9. During this last test, the structure was heavily damaged.

Severe diagonal shear cracks developed in the short wall components W-2 and W-3 in the bottom story, and major diagonal cracks also occurred in W-1 but to a lesser extent as shown in Figure 4.13. In W-1 and W-3, diagonal cracks propagated into the flanges. Significant masonry crushing occurred in W-2 and W-3. Increased horizontal sliding was recorded at the top of W-2 (at the height of the window opening) as indicated in Table 4.6. The final structural period, which was estimated from the free-vibration response of the structure during the tail end of the table motion, was 0.880 sec., about 11 times the initial period. The maximum first- and second-story drifts were 1.83 in. (46.48 mm) and 0.28 in. (7.11 mm), respectively. They correspond to drift ratios of 1.9% and 0.29%. Table 4.6 summarizes the peak values of selected response quantities.

4.5. Detailed test results

Data from the last five tests with the El Centro record scaled to 43%, 86%, 108%, 145%, and 160% are presented and discussed here. For displacement values, the positive direction is towards the east as defined in Figure 4.5.

4.5.1. Global response

Figure 4.14 shows the time-history plots of the bottom-story drifts for the 108%, 145%, and 160% El Centro motions. These are the displacements at the top of the bottom-story wall with respect to the base. To examine changes in the structural period and the response characteristics clearly, the drift is normalized so that the peak value is unity in each motion. It can be observed that major changes in response characteristics occurred in the 160% El Centro motion, especially after 2.5 sec. of shaking.

Figure 4.15 shows the maximum drift ratios developed at each story in each direction during the last five motions. The maximum drift for one story would not necessarily occur at the same time instance as that for the other story. It can be observed that until the 160% El Centro motion, the story drift ratios were less than 0.5%. During the 160% El Centro, which was at the MCE level, the maximum bottom-story drift in negative and positive directions jumped to 1.1% and 1.9%, respectively, indicating the development of a soft-story mechanism. Figure 4.16 shows the normalized deflected shape of the structure developed at the instant the maximum roof displacement was reached during each ground motion.

Figure 4.17 shows the shear force in each story divided by the total seismic weight of the structure, W, (which is 228 kips) occurring at the instant the maximum base shear was developed for each direction during an earthquake motion. As damage occurred, the ratio of the base shear to the shear force in the second story increased due to the change of the deflected shape and thereby the distribution of the inertia forces along the height of the structure. As shown in Figure 4.16, when the soft-story mechanism developed, the structural deformation changed from one with a linear shape to one in which the second story approached like a rigid-body behavior.

The normalized base shear is plotted against the first-story drift ratio in Figure 4.18. The hysteresis curves indicate that the structure reached its shear capacity during the 160% El Centro motion. Although there was significant hysteretic energy dissipation during that motion, the hysteresis curves became pinched in later cycles because of the severe diagonal shear cracks developed in wall components W-2 and W-3. The hysteresis curves also show that the structure had higher strength and displacement ductility

capacity in the positive (east) direction. Moreover, the drift of the first story was more severe in the positive direction for the majority of the ground motions, which is consistent with the strong direction of the table motions in all tests.

4.5.2. Deformation mechanisms

Figure 4.19 and Figure 4.20 show the maximum local drift ratios attributed to the flexural and shear deformations of wall components W-1, W-2 and W-3 during the last three tests. The local drift ratio is calculated as the relative displacement between the top and bottom of the wall segment between openings divided by the corresponding clear height. The maximum drift values associated with flexure and shear might not occur simultaneously. The flexural deformation was calculated with readings from linear potentiometers mounted at the two sides of each wall component (Figure 4.7). The average curvature over each gage length was first calculated from the potentiometer data and then integrated with respect to the vertical distance to obtain the displacement. For W-2 and W-3, data from potentiometers outside the wall segment defined by the clear height are also considered so that the rigid-body rotation of the wall segment caused by the deformation of the masonry below is included in the measurement. The shear deformation was calculated with the method proposed by Massone and Wallace (2004) using the measurements from the diagonal, vertical, and horizontal potentiometers mounted on the surface of each wall component. As shown in Figure 4.19 and Figure 4.20, the wall components had their deformations dominated by flexure with hardly any shear deformation during the 108% and 145% El Centro motions, except that W-3 had quite noticeable shear deformation in the negative direction during the 145% El Centro.

Wall component W-1, which had the highest aspect ratio, had the least amount of shear deformation. Wall components W-2 and W-3 had local drift ratios contributed by shear close to 1.5% during the 160% El Centro. However, W-1 had more significant shear deformation in the negative direction than in the positive direction during the 160% El Centro. This can be explained by the fact that the flange of wall component W-1 enhanced the shear resistance of the wall in the positive direction by arresting the opening of the diagonal crack running from the top west corner to the bottom east corner of the wall.

4.5.3. Yielding of reinforcement

The sequence of yielding of the reinforcing bars in the interior and exterior walls, as detected by strain gages, is shown in Figure 4.21 and Figure 4.22. For conciseness, only the exterior wall components (W-4, W-5, and W-6) on the west side are shown. Those on the east side showed similar behavior. No yielding was detected up to the 43% El Centro. As shown in Figure 4.21a, the first yielding in tension was detected in the vertical reinforcing bars at the two extreme sides of the wall component W-1 in the bottom story during the 86% El Centro, which was slightly below the DE level. The locations of the gages that showed yielding indicate that the wall component was subjected to double curvature with the top and bottom restrained from free rotation. Yielding occurred in all the bars in the flange (designated as W-5) at the base of the wall component. Furthermore, yielding was registered at the top of wall component W-2 and also at the base of wall component W-3, next to the window corner, during the 86% El Centro as shown in Figure 4.21a. During the 108% El Centro, which is at the DE level,

additional vertical bars yielded in tension at the top and bottom of wall components W-1, W-2, and W-3 in the bottom story, and also at the bottom of W-4, a west exterior wall component. Interestingly, yielding occurred immediately above the footing in the extreme vertical bar next to the door in W-2 and in two vertical bars in the flange of W-3, indicating that the masonry panel below the window opening deformed significantly.

During the 108% El Centro, all the vertical bars in W-1 had yielded at the base. A few bars in the second story yielded as indicated by the strain gages mounted on the vertical bars in the exterior wall components and on the horizontal bar in the interior wall close to the window corners. During the 145% El Centro, almost all the vertical bars in the exterior walls in the bottom story yielded and a few more bars in the second story yielded. During the 160% El Centro, yielding in the vertical bars in W-1 extended from the top and bottom of the wall component toward the interior, and the vertical bars in W-2 and W-3 started to yield in tension at the elevations of the top and bottom of the window opening indicating the short pier effect. In addition, some horizontal bars in W-1, W-2, and W-3 yielded in tension due to the opening of diagonal cracks. As shown in Figure 4.21b and Figure 4.22b, the reinforcement in the out-of-plane wall components started yielding in the 86% El Centro, and all the dowels at the base yielded during the 145% El Centro.

4.5.4. Axial deformations of in-plane walls

The axial deformations of wall components W-1, W-2, and W-3 were obtained by averaging the axial displacements measured by the two lines of vertical linear potentiometers mounted along the edges of each wall component over the entire story

height. This axial deformation was caused by two mechanisms. One was the rocking of a wall component as flexural cracks and shear cracks developed, and the other was the axial force introduced by the coupling actions of the lintels and floor slabs. Figure 4.23 shows the axial deformation of each wall component plotted against the story drift. The V-shaped curves indicate the dominance of the rocking mechanism. However, the axial deformations in W-1 and W-3 were higher in one drift direction than the other by a significant amount, while those in W-2 appeared to be quite symmetrical. This difference can be attributed to the upward and downward axial forces exerted on W-1 and W-3 by one-sided coupling actions from the lintels. When the structure displaced toward the positive direction, the coupling force was upward on W-1 and downward on W-2. The opposite is true for the other drift direction. Wall component W-2 did not experience such axial force because it had coupling elements on both sides whose effects more or less offset each other.

4.5.5. Contribution of out-of-plane walls to lateral resistance

Figure 4.24 shows the average strains measured in the vertical bars at the bottom of wall components W-4 and W-6 during the 145% El Centro. These exterior walls were orthogonal to the direction of shaking. It should be noted that the pre-compression due to the gravity load is not shown in the strain plots (i.e., the strain value starts at zero before testing). The curves have a V shape like those in Figure 4.23 and that the strains were always in tension. However, the strain plots are not symmetrical about the zero-drift position, with the east and west walls showing opposite biases. This was caused by the overturning moment introduced to the structure by the lateral seismic forces. The tensile

strains were induced by two mechanisms. The first mechanism, as illustrated in a simplified diagram with one in-plane wall in Figure 4.25, is the uplift forces introduced by the rocking of the in-plane wall components, W-1, W-2, and W-3, as discussed previously. This mechanism introduced tensile forces to the out-of-plane walls and compressive forces to the in-plane walls. The second mechanism is the out-of-plane bending of the exterior wall components during the sidesway of the structure. The reinforcement layer at the middle plane of the wall components would be subjected to tension regardless of the direction of the bending curvature. Both mechanisms result in the V-shaped strain-vs.-story drift.

The exterior walls could contribute to the lateral load resistance of the structure through both aforementioned mechanisms. However, the first mechanism, which introduced axial compression on the in-plane walls, had a much greater contribution. The increase of the axial compressive force on the in-plane wall components enhanced their flexural and shear resistances. This is supported by the following analysis in which the base shear capacity of the structure is calculated with two scenarios. First, the flexural and shear strengths of each in-plane wall component in the bottom story were calculated according to the specifications in Sections 9.3.2 and 9.3.4.1.2 of the MSJC Code (MSJC 2013) without the strength reduction factors, using the actual material properties shown in Table 4.3 and Table 4.4, and the strength is determined according to the governing mechanism. For the flexural strength, it is assumed that plastic hinges developed at the top and bottom of the wall segment defined by the clear height of each wall component. In this calculation, the axial load in each wall component is assumed to be contributed by the gravity load only according to the tributary floor area. The axial forces due to the

lateral seismic forces are ignored assuming that the effect of the additional axial tension in one of the two outer wall components, W-1 and W-3, would be offset by the axial compression in the other. The axial forces exerted by the out-of-plane wall components are also ignored. The results are shown in Table 4.7, under "Axial load distribution 1". The calculated base shear capacity is lower than that deduced from the experimental results (as shown in Figure 4.18) by a factor of 1.4. Moreover, all three wall components appear to be flexure-dominated, and the flexural strengths of the out-of-plane wall constitute 14% of the total lateral resistance of the structure.

In the second scenario, the axial compression exerted by the out-of-plane walls and transmitted through the horizontal diaphragms and lintels to the in-plane walls is considered. It is assumed that the maximum axial compression exerted is equal to the tensile yield force developed by all the vertical reinforcement in the out-of-plane walls (based on the actual yield strength shown in Table 4.4), because experimental results show that all these bars yielded in tension. It is inherent in this assumption that the same vertical reinforcement would not be able to provide the out-of-plane bending resistance. The compressive force was distributed to the in-plane wall components based on their relative axial stiffnesses. The flexural and shear strengths of the in-plane wall components are then calculated in the same way as in the first scenario. The results are shown in Table 4.7, under "Axial load distribution 2." This second calculated base shear capacity is closer to the experimental result. The second scenario also results in a failure mechanism close to that observed in the experiment, with the calculated strength values showing that W-2 and W-3 are shear dominated. Results in Table 4.7 show that the axial compression exerted by the out-of-plane walls through the horizontal diaphragms and

lintels could increase the base shear capacity of the structure by 47%. However, by comparing to the same in-plane wall system without out-of-plane walls, the increase would be 70%.

4.5.6. Displacement-based vs force-based design

For comparison purposes, the structure is redesigned using the conventional force-based method according to ASCE/SEI 7-10 (ASCE 2010) and the MSJC Code (MSJC 2013). Since the effect of the vertical ground motion was not considered in the displacement-based design, it is also ignored in the force-based design. Furthermore, the out-of-plane walls were not taken into consideration in the force-based design. Two cases are considered for the force-based design. Case 1 complies with the prescriptive reinforcement requirements for special walls in the MSJC Code, whereas Case 2 ignores the maximum spacing limit for the reinforcing steel. The reinforcement details for the three designs are presented in Table 4.8. Case 2 has the least vertical and horizontal reinforcement as compared to the other two designs. Case 1 has similar horizontal reinforcement but less vertical reinforcement than the displacement-based design. Table 4.9 summarizes the base shear capacities calculated for the two force-based design cases. Both cases have a lower base shear capacity than the displacement-based design. However, all three designs have similar failure mechanisms. Although the shear capacity design requirement of the code is satisfied in the force-based designs, wall components W-2 and W-3 will still be shear-dominated when the axial load combination 2 is considered (which is more realistic), as shown in Table 4.9. With the reduced base shear capacity and the same failure mechanism as the other two designs, Case 2 of the force-

based design is expected to have the worst seismic performance. Furthermore, the reduction of the vertical reinforcement can adversely affect the ductility capacity of the shear-dominated wall components.

Chapter 4, in part, is a reprint of material as it appears in Mavros, M., Ahmadi, F., Shing, P.B., Klingner, R., McLean, D., and Stavridis. A., "Shake-table Tests of a Full-scale Two-story Shear-dominated Reinforced Masonry Wall Structure," ASCE Journal of Structural Engineering (under review). The dissertation author was the primary investigator and author of this paper

Table 4.1 - Scale factors.

Quantity	Scaling Law	Scale Factor
Seismic Mass	S_{SM}	0.59
Length	S_L	1.00
Stress	S_σ	1.00
Force	$S_F = S_L^2 \cdot S_\sigma$	1.00
Seismic Acceleration	$S_{SA} = S_F / S_{SM}$	1.70
Gravity Mass	S_{GM}	1.00
Gravitational Acceleration	$S_{GA} = S_F / S_{GM}$	1.00
Time	$S_t = \sqrt{S_L / S_{SA}}$	0.77
Frequency	$S_f = 1 / S_t$	1.30
Strain	S_ε	1.00

Table 4.2 - Average 28-day compressive strengths of mortar and grout samples.

Story	Type of specimen	Average compressive strength
		ksi
1st story	3 in. x 6 in. mortar cylinders	5.55
	8 in. x 4 in. x 4 in. grout prisms	3.15
	6 in. x 12 in. grout cylinders	2.77
2nd story	8 in. x 4 in. x 4 in. grout prisms	3.92
	6 in. x 12 in. grout cylinders	3.25

Table 4.3 - Average masonry prism properties.

Story	Test day	Compressive strength	Modulus of elasticity	Strain at peak stress
		ksi	ksi	
1st story	28 days after grouting	2.17	1278	0.0022
2nd story	28 days after grouting	1.57	1034	0.0019
1st story	1st DE test (54 days after grouting)	2.26	1110	0.0023
2nd story	1st DE test (40 days after grouting)	1.62	1095	0.0018

Table 4.4 - Average tensile properties of No. 4 bars.

	Modulus of elasticity	Yield stress	Tensile strength	ε_y [1]	ε_{sh} [2]	ε_{su} [3]
	ksi	ksi	ksi			
Slab	29400	73.0	104	0.00249	0.0107	0.107
Wall	28600	65.0	98.4	0.00227	0.0108	0.136

[1]Yield strain
[2]Strain at initiation of strain hardening
[3]Strain at bar fracture

Table 4.5 - Testing sequence.

Test ID	Input level	PGA Measured from Table [g]	Period of test structure before test [sec]	Period of prototype structure before test [sec]
2	30% of El Centro 1979	0.236	0.077	0.100
3	43% of El Centro 1979	0.362	N/A	N/A
5	30% of El Centro 1979	0.264	0.083	0.108
7	43% of El Centro 1979	0.360	0.082	0.107
8	43% of El Centro 1979	0.379	N/A	N/A
10	86% of El Centro 1979	0.642	0.084	0.109
13	108% of El Centro 1979	0.752	0.090	0.118
15	145% of El Centro 1979	1.026	0.113	0.148
17	160% of El Centro 1979	0.919	0.218	0.284

Table 4.6 - Peak values of selected response quantities.

Test ID	Input level	Acceleration [g]		Drift [in./mm]		Base shear		Sliding in wall components[1] [in.]					
								W-1		W-2		W-3	
		2nd level	Roof	1st story	2nd story	[kips]	Normalized by the seismic weight	Top	Base	Top	Base	Top	Base
5	30% of El Centro 1979	0.39	0.44	0.03	0.01	58	0.26	N/A	0.00	0.00	0.00	0.00	0.00
8	43% of El Centro 1979	0.56	0.66	0.04	0.02	85	0.37	N/A	0.00	0.00	0.00	0.00	0.00
10	86% of El Centro 1979	1.10	1.28	0.13	0.07	156	0.68	N/A	0.00	0.00	0.00	0.00	0.00
13	108% of El Centro 1979	1.25	1.48	0.21	0.08	182	0.80	N/A	0.01	0.01	0.00	0.00	0.00
15	145% of El Centro 1979	1.49	1.87	0.40	0.22	215	0.94	N/A	0.06	0.02	0.00	0.00	0.00
17	160% of El Centro 1979	1.83	1.81	1.83	0.29	219	0.96	N/A	0.22	0.32	0.04	0.02	0.00

[1]The top and base of each wall component are defined with respect to the clear height

Table 4.7 - Calculated base shear capacity for the test structure

	Axial load distribution 1		Axial load distribution 2	
	Flexural strength (kips)	Shear strength (kips)	Flexural strength (kips)	Shear strength (kips)
W-1	38	67	71	90
W-2	34	55	76	72
W-3	64	67	120	91
Out-of-plane walls	22	-	0	-
Base shear capacity (kips /normalized by the seismic weight)	158 / 0.70		234 / 1.02	

Table 4.8 - Comparison of reinforcement layouts for displacement-based and force-based designs

Design method		**Wall segment**	**Wall cross-sections** (**Hollow circle = No. 3 bars Solid circle = No. 4 bars Solid triangle = No. 5 bars**)	**Vertical bars**	**Vertical reinforcement ratio**	**Horizontal bars**	**Horizontal reinforcement ratio**
Displacement-based design		W-1	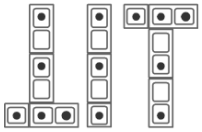	5 No. 4	0.22%	No. 4 @ 16 in.	0.16%
		W-2		3 No. 4	0.19%	No. 4 @ 16 in.	0.16%
		W-3		5 No. 4	0.22%	No. 4 @ 16 in.	0.16%
Force-based design	Maximum bar spacing requirement is applied (Case 1)	W-1	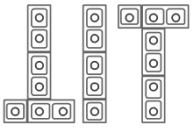	7 No. 3	0.17%	No. 3@ 8 in.	0.17%
		W-2		5 No. 3	0.17%	No. 3@ 8 in.	0.17%
		W-3		7 No. 3	0.17%	No. 3@ 8 in.	0.17%
	Maximum bar spacing requirement is not applied (Case 2)	W-1	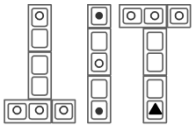	4 No. 3	0.10%	No. 3 @ 16 in.	0.09%
		W-2		2 No. 4 & 1 No. 3	0.16%	No. 4 @ 16 in.	0.16%
		W-3		3 No. 3 & 1 No. 5	0.14%	No. 4 @ 24 in.	0.10%

Table 4.9 - Calculated base shear capacities for the force-based designs

	Force-based design (Case 1)				**Force-based design (Case 2)**			
	Axial load distribution 1		Axial load distribution 2		Axial load distribution 1		Axial load distribution 2	
	Flexural strength (kips)	Shear strength (kips)	Flexural strength (kips)	Shear strength (kips)	Flexural strength (kips)	Shear strength (kips)	Flexural strength (kips)	Shear strength (kips)
W-1	32	68	66	92	23	61	60	84
W-2	32	56	73	73	30	55	73	72
W-3	54	68	112	92	50	63	109	86
Out-of-plane walls	22	-	0	-	22	-	0	-
Base shear capacity (kips /normalized by the seismic weight)	140 / 0.61		231 / 1.01		125 / 0.55		218 / 0.96	

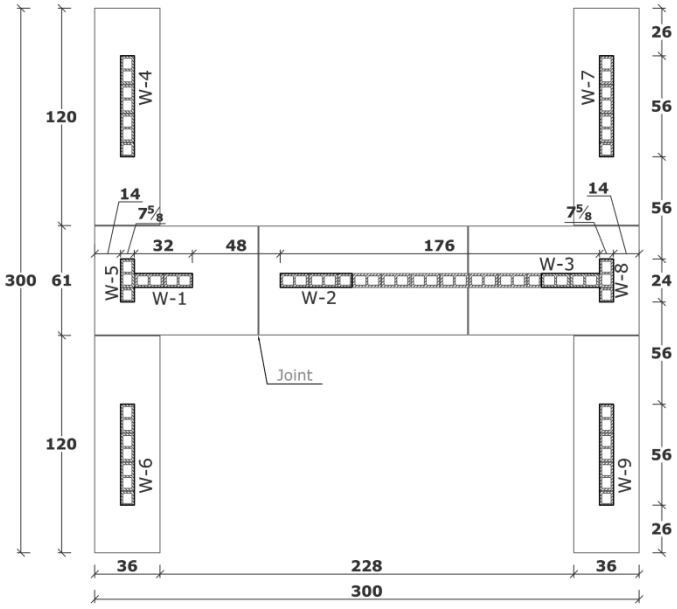

Figure 4.1 - Foundation plan and wall layout. All the dimensions are in inches (1 in. = 25.4 mm)

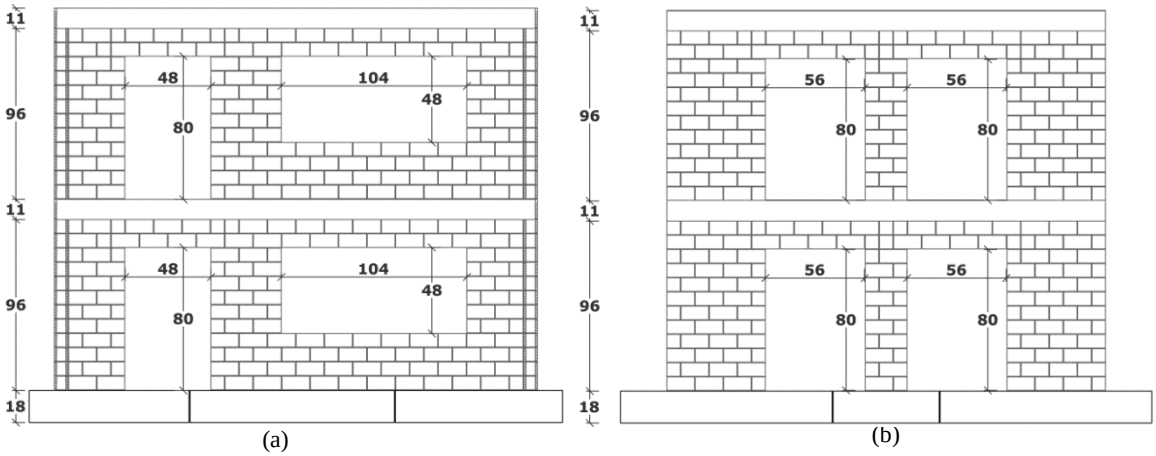

Figure 4.2 - Specimen configuration: a) Elevation view of the interior wall. b) Elevation view of an exterior wall. All the dimensions are in inches (1 in. = 25.4 mm)

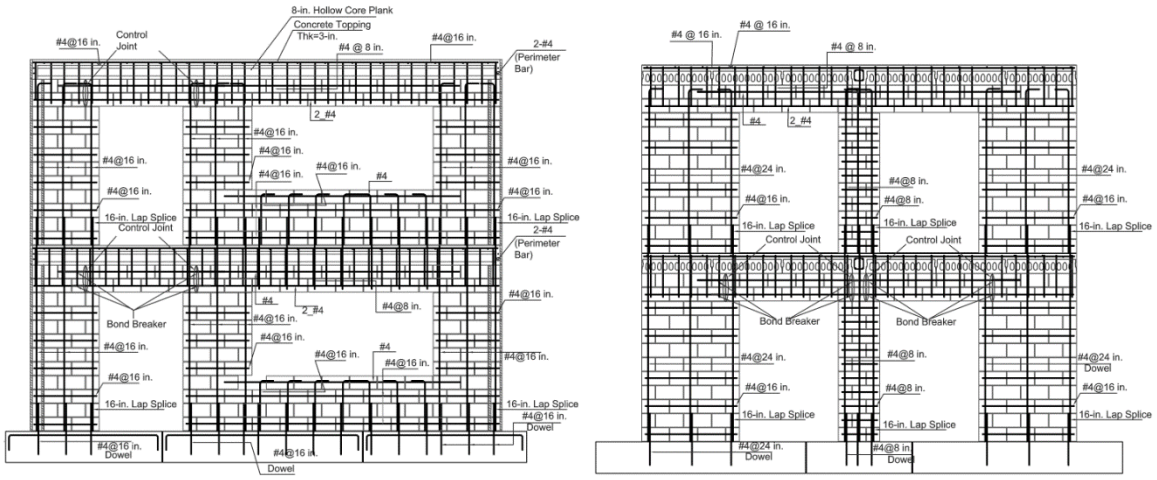

Figure 4.3 - Reinforcing details: a) Interior wall b) Exterior Wall. (1 in. = 25.4 mm)

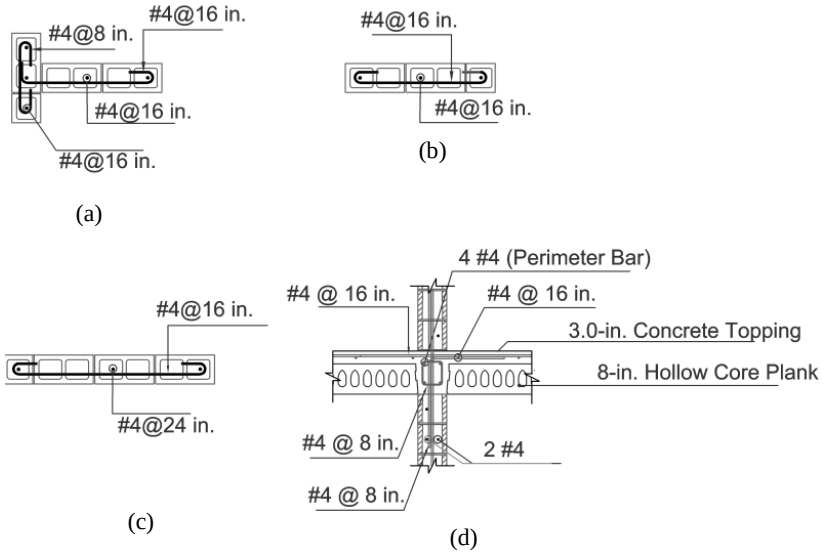

Figure 4.4 - Cross-sections and reinforcing details of a) W-1 and W-3, b) W-2, c) W-4, W-6, W-7 and W-8, d) Slab and beam. (1 in. = 25.4 mm)

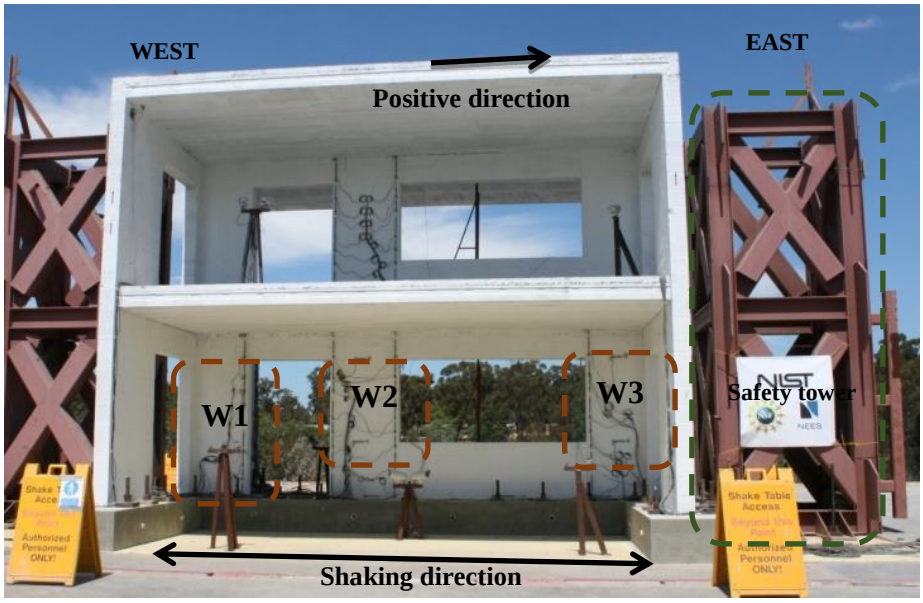

Figure 4.5 - Elevation view of the test structure.

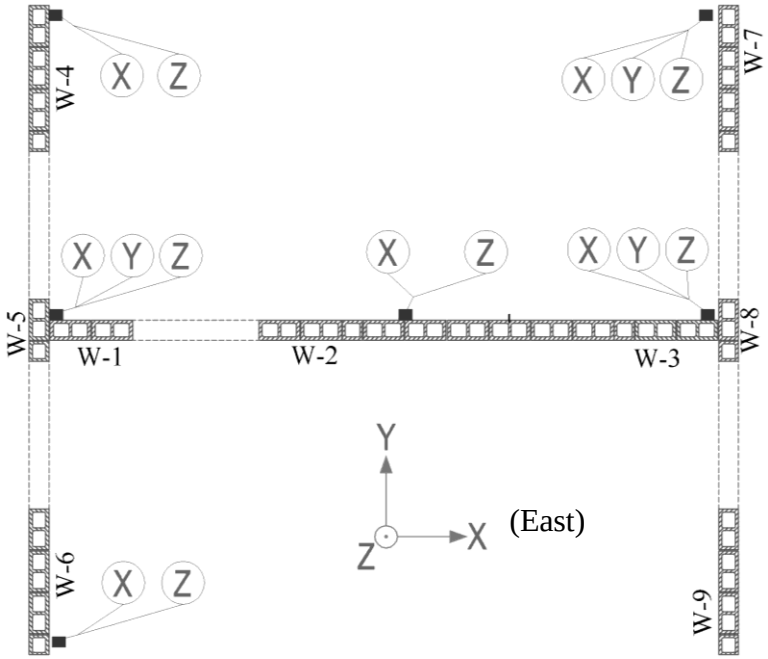

Figure 4.6 - Locations and directions of accelerometers on each floor.

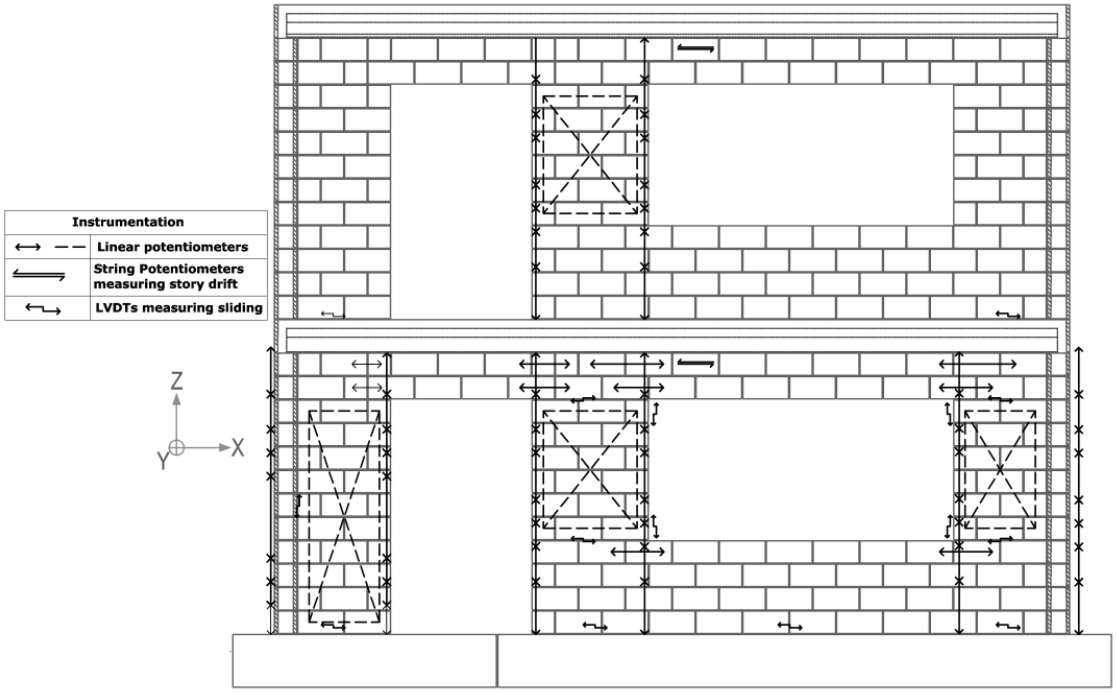

Figure 4.7 - Locations of linear and string potentiometers on the interior wall.

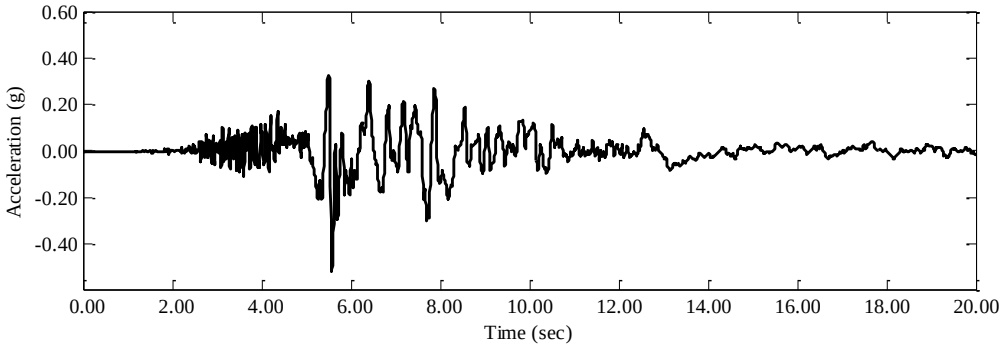

Figure 4.8 - Unscaled 1979 El Centro.

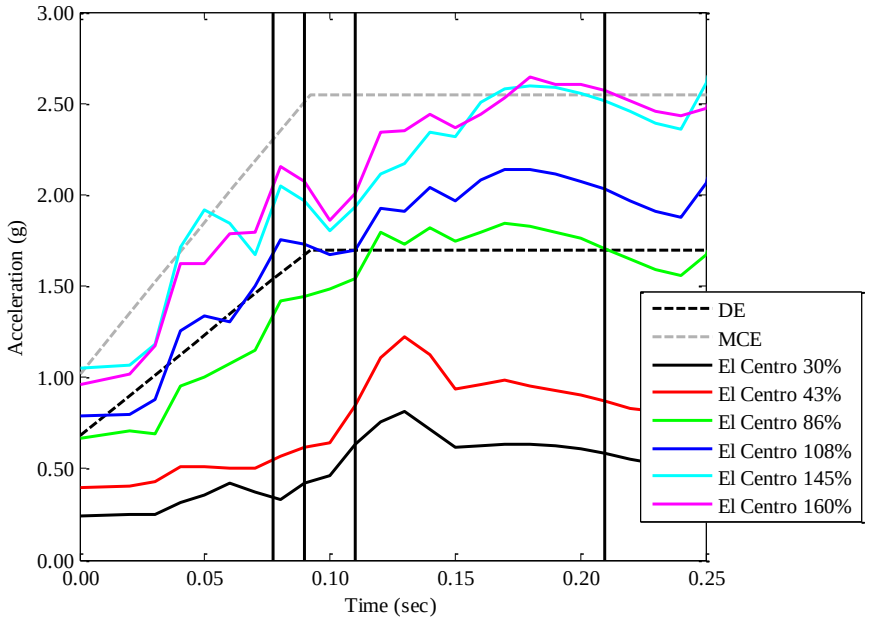

Figure 4.9 - Pseudo-spectral acceleration of table motions (5% damping)

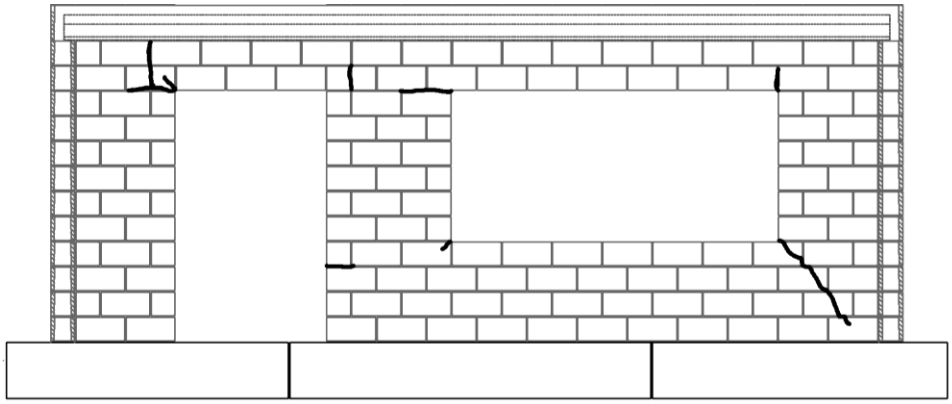

Figure 4.10 - Crack pattern in 1st story after 86% El Centro.

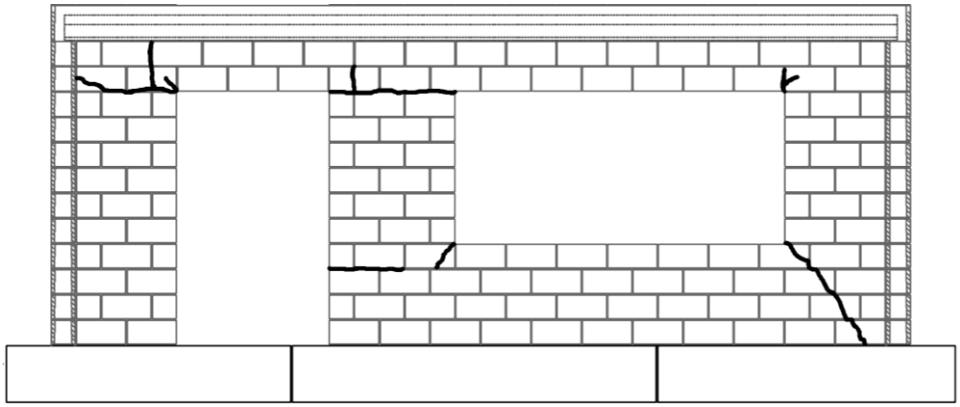

Figure 4.11 - Crack pattern in 1st story after 108% El Centro.

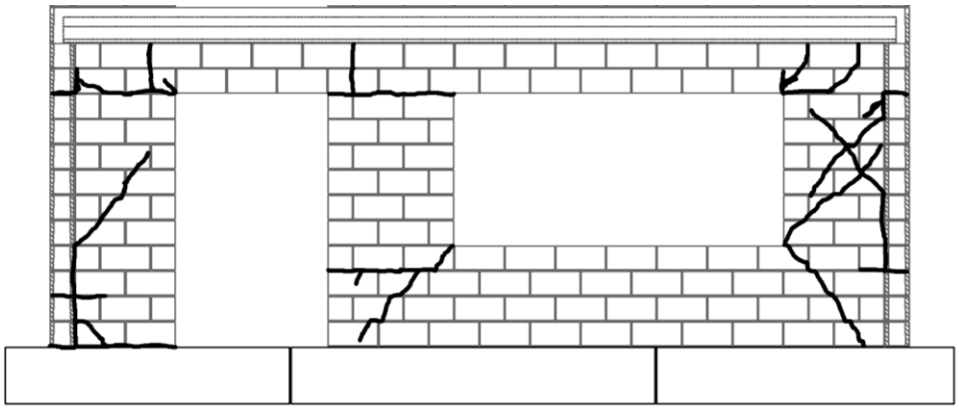

Figure 4.12 - Crack pattern in 1st story after 145% El Centro.

(a) Pier W-1 (b) Pier W-2 (c) Pier W-3

Figure 4.13 - Damage of interior wall after 160% El Centro.

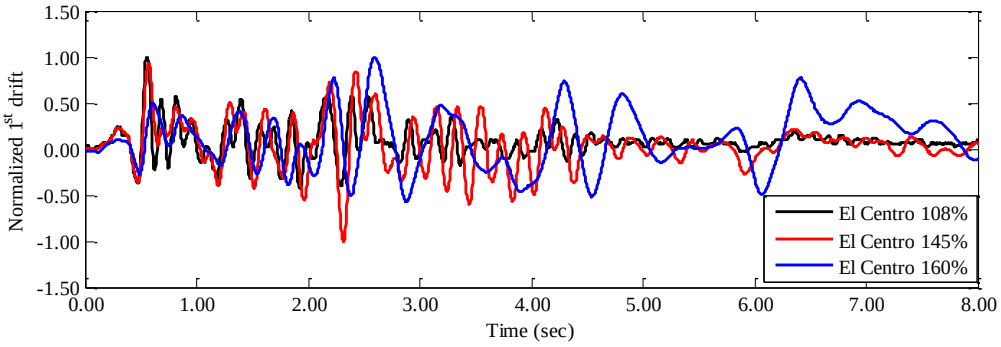

Figure 4.14 - Normalized drift time-history plots.

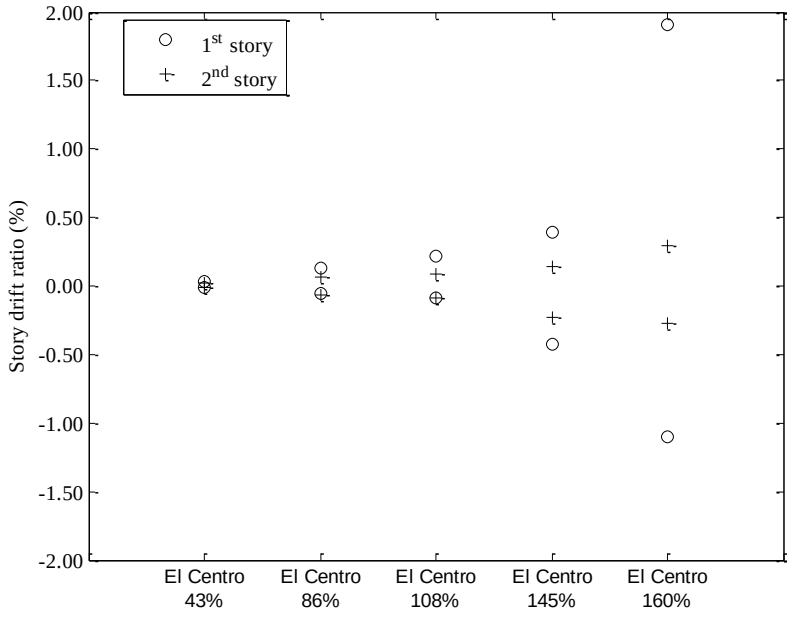

Figure 4.15 - Maximum story-drift ratios.

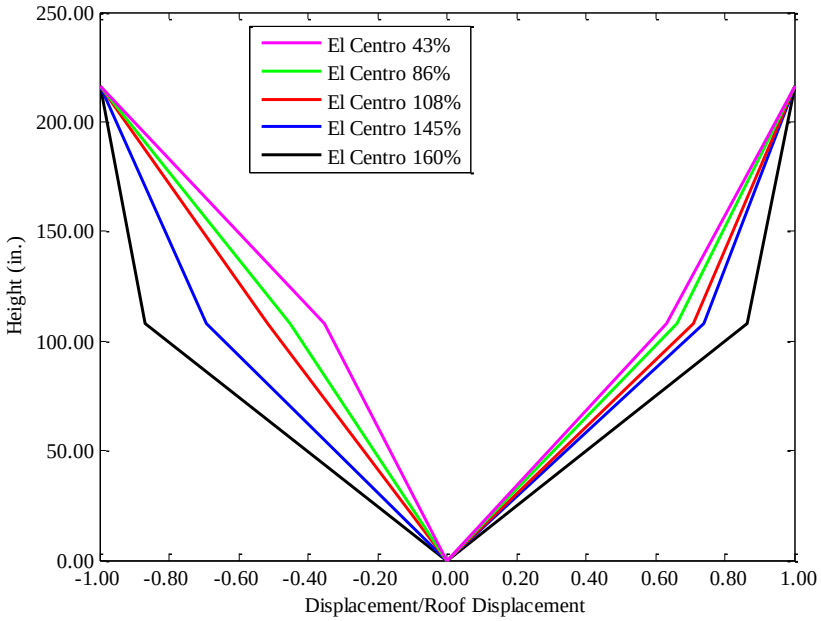

Figure 4.16 - Deflected shapes at maximum roof displacement.

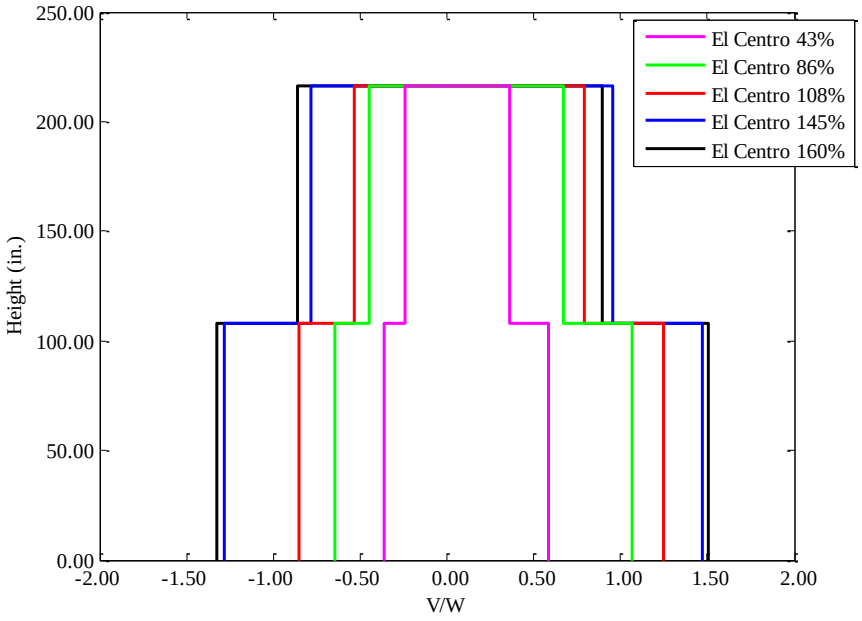

Figure 4.17 - Shear force variation at maximum base shear.

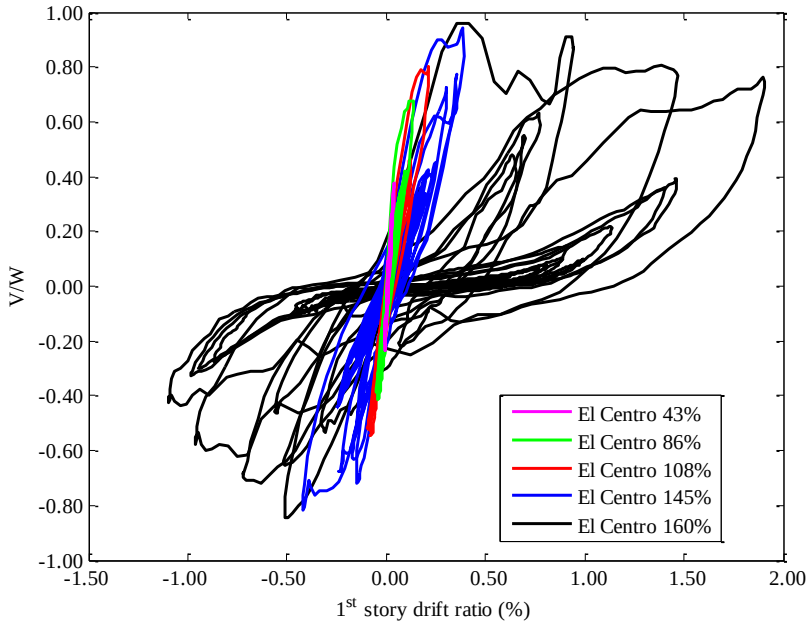

Figure 4.18 - Base shear-vs-first-story drift ratio.

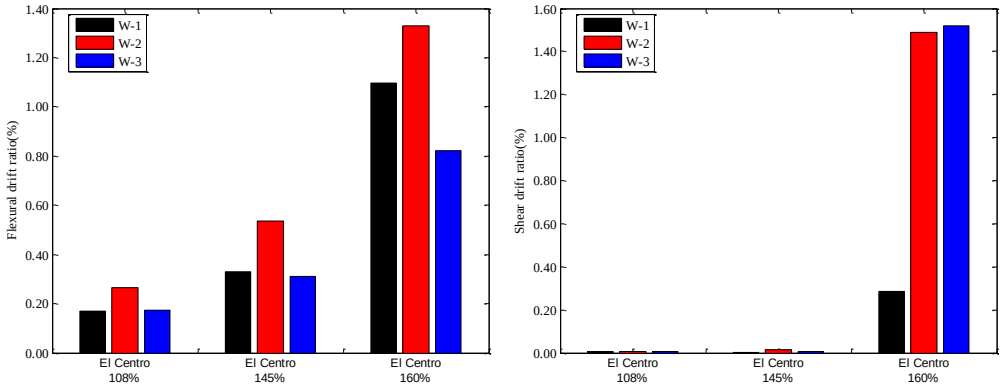

(a) Flexural deformation (b) Shear deformation

Figure 4.19 - Flexural and shearing deformations at the maximum drifts in the positive direction.

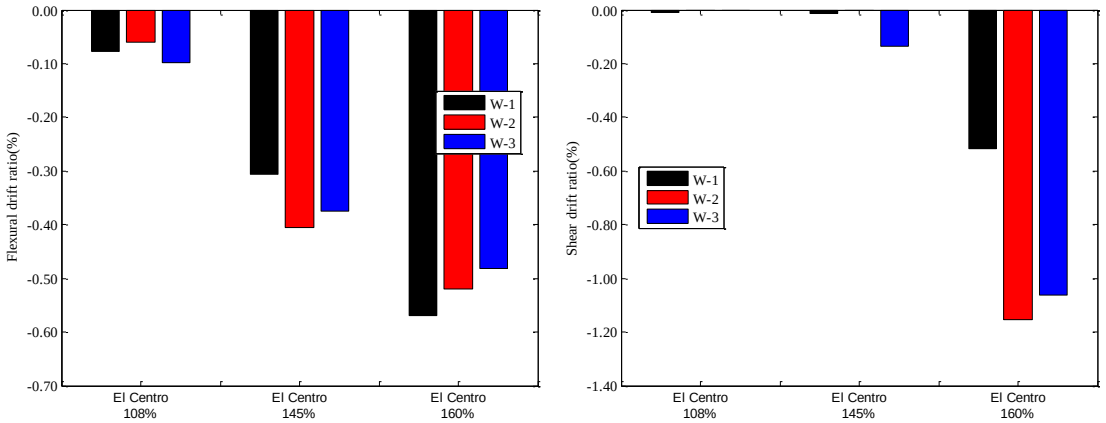

(a) Flexural deformation (b) Shear deformation

Figure 4.20 - Flexural and shearing deformations at the maximum drifts in the negative direction.

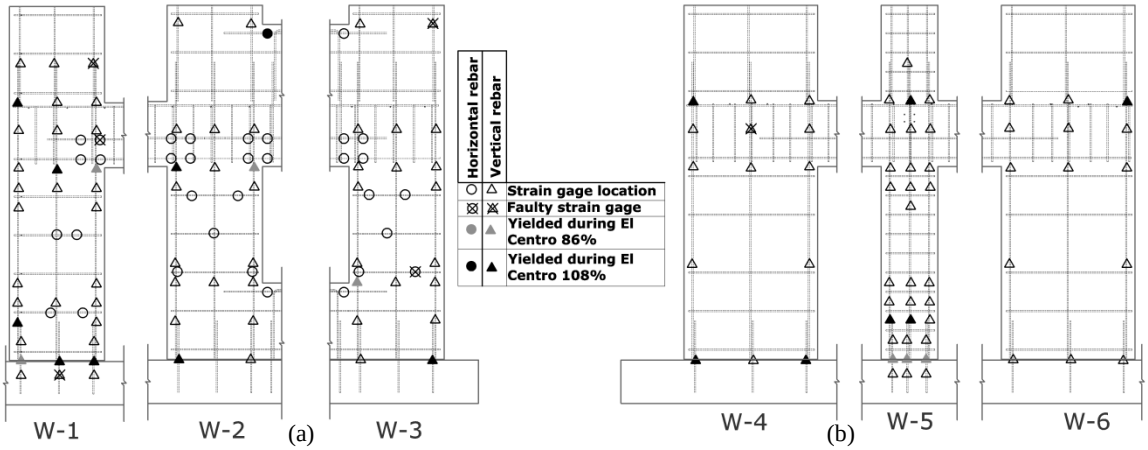

Figure 4.21 - Yielding of reinforcement for a) interior wall and b) west exterior wall up to 108% El Centro.

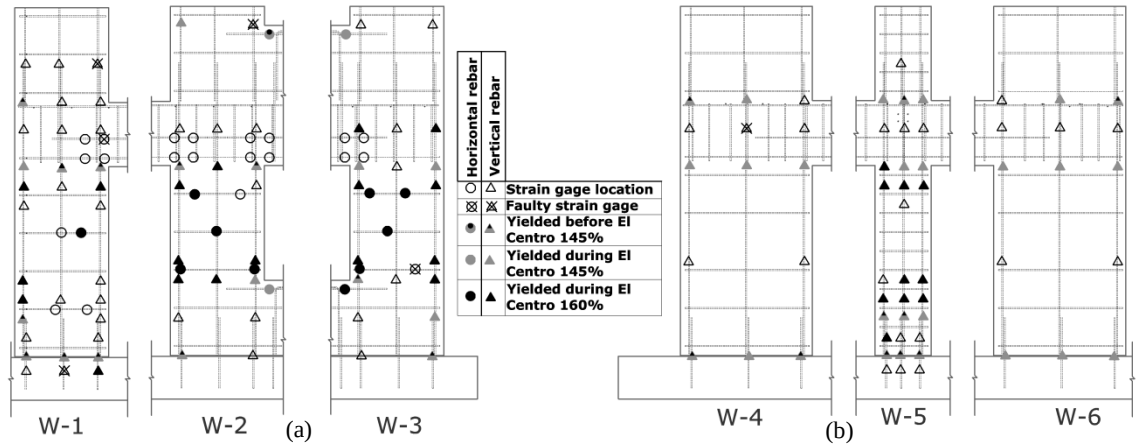

Figure 4.22 - Yielding of reinforcement for a) interior wall and b) west exterior wall up to 160% El Centro.

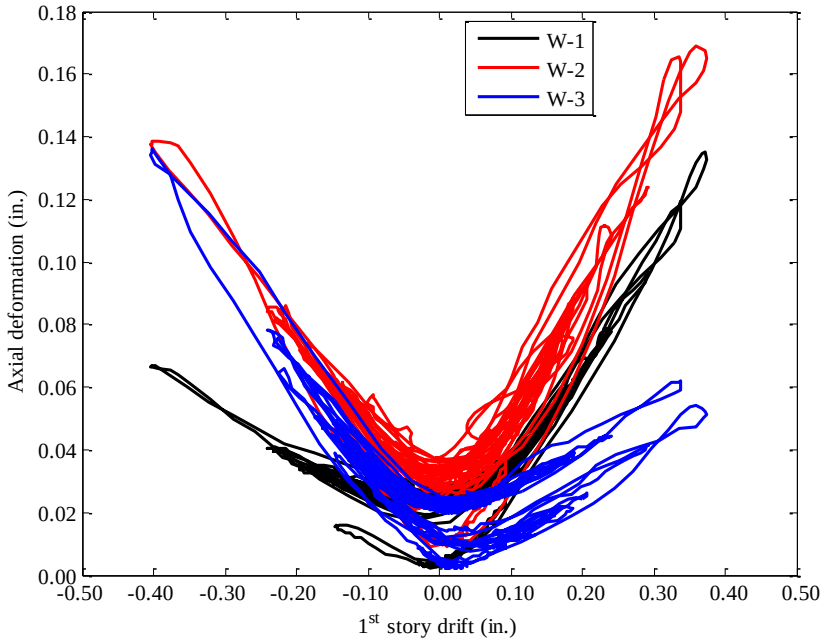

Figure 4.23 - Axial deformation of interior wall segments during 145% El Centro.

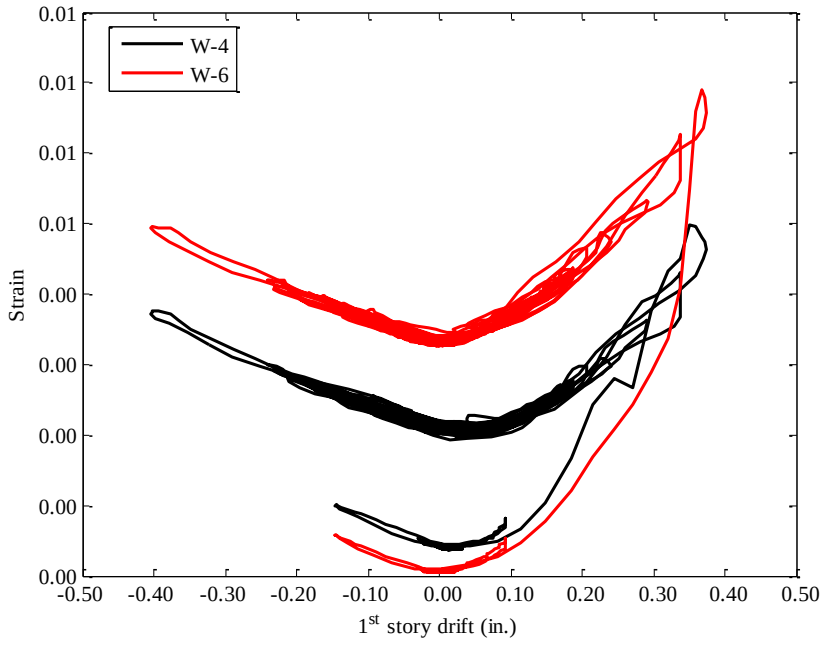

Figure 4.24 - Average strains in dowels at the bottom of west exterior wall segments during 145% El Centro

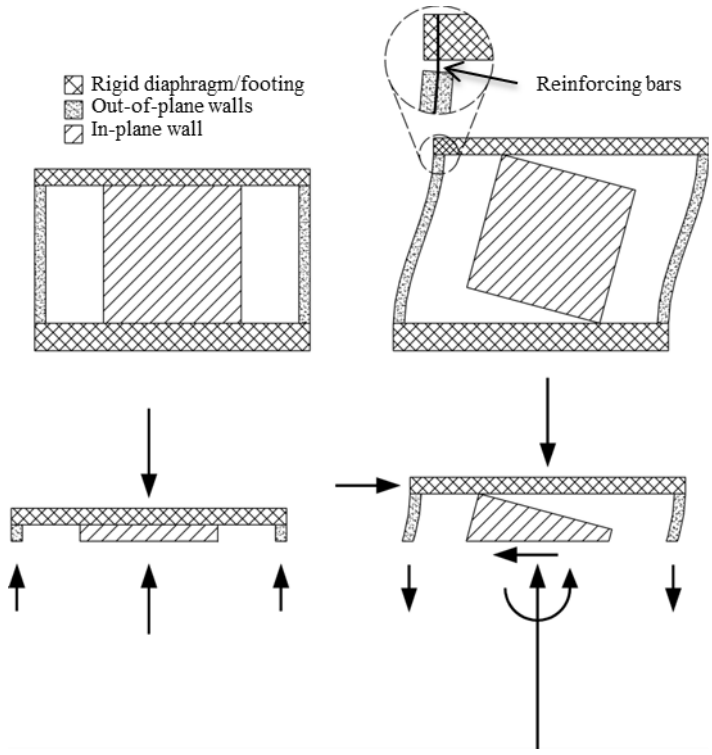

(a) Without lateral

(b) Tension in out-of-plane walls due to rocking of in-

Figure 4.25 - Deformation mechanims

5. NUMERICAL MODELING OF THE DYNAMIC RESPONSE OF THE TWO-STORY STRUCTURE

The modeling approach proposed in Chapter 2 and validated with wall segment tests in Chapter 3 has been applied to simulate the response of the two-story structure tested on the shake-table, as presented in Chapter 4. The model description, model calibration, and the comparison of selected experimental and numerical results are presented in this chapter. The close agreement between numerical and experimental results indicates that the proposed modeling method can accurately capture the response of reinforced masonry (RM) structural systems under dynamic loading. The numerical results also provide additional insight to the behavior of the tested structure. Additional dynamic and monotonic pushover analyses have been performed to investigate the influence of the out-of-plane walls on the seismic response of the structure, and the performance of a similar structure designed according to current code provisions using the force-based approach.

5.1. Modeling of the two-story structure

Since the 2-story test structure is symmetric about a vertical plane parallel to the direction of the base motion, only half of the structure is modeled, as shown in Figure 5.1. To enforce symmetry, all nodes of the in-plane wall are fixed from displacement in the *z*-direction and fixed from rotation about the *x*- and *y*-axes. The nodes along the base of the structure are restrained from translation and rotation in all directions. Different discretization schemes are used for the horizontal diaphragms, and the in-plane and out-of-plane walls. The two horizontal diaphragms are modeled with rectangular smeared-

crack shell elements, as they are not expected to experience severe cracking. The shell elements have a thickness of 11 in. representing the thickness of the precast planks plus the 3-in. topping. The reinforcing steel in the topping slab is modeled as a smeared overlay located 1.5 in. below the top surface of the slabs. No special considerations are given to the prestressing steel located at the bottom of the precast planks in that the prestressing force is ignore and the steel is modeled as a smeared overlay. Moreover, the hollow cores of the precast planks are not modeled. Given that the out-of-plane walls are not likely to be shear critical, a rectangular mesh is used with cohesive crack interfaces placed horizontally. The vertical reinforcing bars in the out-of-plane walls are modeled with truss elements, while the horizontal reinforcement is modeled with a smeared overlay at the mid-surface of the shell elements. The in-plane wall is modeled with the proposed meshing scheme, as discussed in Chapter 2 and Chapter 3, with cohesive interfaces oriented horizontally, vertically, and diagonally, as shown in Figure 5.1. Both the vertical and horizontal reinforcement of the in-plane wall is modeled with truss elements connected to the shell elements through bond-slip interfaces. The calibration of the material parameters is shown in Table 5.1.

The mass is distributed to all the nodes based on the tributary area of the elements that are connected to each node. A constant force equal to the mass times the acceleration due to gravity is applied to each node in the negative y-direction to simulate the gravity load on the specimen. Instead of applying base acceleration to the structural modal, a horizontal inertial force equal to the nodal mass times the negative ground acceleration are applied to each node. The Hilber-Hughes-Taylor (HHT) method (Hilber et al. 1977) is used for direct time integration, with a time step of 1/240 sec. The HHT method is an

implicit method that has numerical damping to suppress undesired higher-frequency modes. The values of the numerical parameters for the HHT method used in all the dynamic analyses for this study are

$$\begin{aligned} \alpha &= 0.94 \\ \beta &= 0.2809 \\ \gamma &= 0.56 \end{aligned} \tag{5.0}$$

Viscous damping is assumed to be zero.

5.2. Comparison of experimental and numerical results

In the shake-table tests, the structure was subjected to nine earthquake ground motions. In the analyses, the finite element model is subjected to the last five ground motions sequentially accounting for the cumulative damage incurred by each motion. Since the response of the test structure was in the linearly elastic range during the first four motions, these motions are not included in the simulations. The acceleration time histories, as recorded by the accelerometers mounted on the shake-table, are used in the analyses.

5.2.1. First-story drift and base-shear capacity

Figure 5.2 through Figure 5.6 compare the experimental and numerical results in terms of the first-story drift time histories, base shear time histories, and base shear-vs.-first-story drift hysteresis curves. The good match of the numerical and experimental results indicates that the model is able to capture the behavior of the three-dimensional structure well.

During the 43% El Centro record, in which the response of the structure was elastic, the model well captures the initial stiffness and drift levels. For the 86% El Centro, the model shows more or less elastic behavior, while the actual test structure started to develop nonlinear behavior, as shown in Figure 5.3. As it is mentioned in Section 3.3.4, the finite element models used here tend to underestimate the hysteretic energy dissipation during the first cycles. The reduced hysteretic energy dissipation results in the overestimation of the first-story drift in the negative direction as shown in Figure 5.3.

The analysis results for El Centro 108% and 145% are very similar to the experimental results (see Figure 5.4 and Figure 5.5). The model accurately predicts the maximum base shear and the first-story drift experienced by the test structure during those motions. Furthermore, the gradual stiffness degradation due to the damage accumulation is well captured. Finally, during the 160% El Centro record, in which severe damage occurred in the test structure with diagonal shear cracks, the model captures the response well but underestimates the base shear capacity by 13%. However, the maximum base shear capacity predicted by the model during El Centro 145% is 217.4 kips, which is very close to the actual base shear capacity of 219.2 kips developed in El Centro 160% during the test. Furthermore, the model underestimates the maximum first-story drift in the negative direction during El Centro 160%. Given the complexity of the structural system and the failure mechanism, the correlation of the numerical and experimental results can be considered excellent.

5.2.2. Crack pattern and failure mechanism

The deformed mesh of the finite element model can provide valuable information about the predicted failure mechanism of the structure. Figure 5.7 through Figure 5.10 show the deformed mesh of the model when the maximum first-story drifts are reached in the positive and negative directions as well as the observed crack pattern of the structure after El Centro 86%. Prior to that motion, no cracks developed in the analyses. The model captures very well both the location of the cracks and their evolution in time. However, the diagonal crack developed in wall component W-1 during the last earthquake motion is not reproduced in the analysis. Nevertheless, it should be mentioned that this diagonal did not open as severely as those in other wall components during the tests.

5.2.3. Strains in reinforcement

The ability of the model to capture local responses, such as the strains in the reinforcing bars, is also investigated. The locations where the strain values calculated in the analyses and recorded in the tests are compared are shown in Figure 5.11. In the locations where two strain gages were mounted on the opposite sides of the bar, the average of the two strain values are considered.

The comparisons of the strain time histories for the selected locations are shown in Figure 5.12 through Figure 5.23. The recorded strain values do not include the compressive strains due to the gravity load. Hence, the numerical computed strains after the application of the gravity load are subtracted from the numerical results. Recognizing the fact that the strain can vary rapidly along a reinforcing bar and that the strain value can be greatly affected by the proximity of the strain gage to a crack, the correlation

between the numerical and experimental results is reasonably good up to El Centro 145%. During El Centro 160%, many of the strain gages (or their wires) were damaged.

5.2.4. Sliding of wall components

During the tests, sliding along the bed joins of the in-plane wall was recorded at five locations, as indicated in Figure 5.24. Significant sliding was detected only in the last motion during the test, and it is compared to the computed values in Figure 5.25. It can be observed that the correlation of the numerical and experimental results is not very good. The sliding resistance of a wall component is controlled by a number of factors including the axial load, the friction along the sliding interface, and the dowel action of the vertical bars.

5.3. Validation of the displacement-based design

The test structure was designed with a displacement-based approach. Wall components W-2 and W-3 were expected to be shear dominated. Hence, the maximum allowable interstory drift was limited to 0.3% for the DE and 0.6% for the MCE. The maximum first-story drift recorded in the test during the 108% El Centro (DE level) was 0.22%, which is below the allowable drift limit. However, the maximum first-story drift experienced by the structure during the 160% El Centro (MCE level) was 1.91%, which is more than three times the allowable drift limit for that earthquake. This can be attributed to the damage accumulated in the structure during the prior ground motions. To investigate the performance of an undamaged structure during the DE and the MCE, analyses are performed by subjecting the structure to these motions independently. For this purpose, the original record of the 1979 El Centro was scaled by a factor of 85% and

128% to match the spectral accelerations of the DE and MCE at the initial fundamental structural period of the structure. Furthermore, since the seismic mass of the structure is different from its the gravity mass as discussed in Chapter 4, the motions are scaled in time and amplitude to satisfy dynamic similitude requirements, with the scale factors shown in Table 4.1. As shown in Figure 5.26 and Figure 5.27, the maximum first-story drifts for the DE and MCE from the analyses are 0.18% and 0.48%, respectively, meeting the design requirements.

5.4. Investigation of the force-based design

In Section 4.6.6, a comparison between the displacement-based and the force-based designs has been made. For the forced-based design, two cases have been considered. In Case 1, the design complies with the prescriptive reinforcement requirements for special walls in the MSJC Code, whereas in Case 2, the maximum spacing limit for the reinforcing steel is ignored. In this Section, the structure redesigned for Case 2 is modeled and analyzed. For comparison with the displacement-based design, the model is subjected to the DE and MCE motions independently as in Section 5.3, and the results are compared in Figure 5.28 and Figure 5.29.

The only difference between the two structures is in the reinforcement content, as shown in Table 4.8. Hence, as expected, the two models have similar responses for the DE. During the MCE, the reduction of the reinforcement content for the force-based design results in an increase of the first-story drift ratio from 0.48% to 0.60% (an increase of 20%). In spite of this, both designs are considered safe for the MCE.

5.5. Contribution of the out-of-plane walls

In Section 4.6.5, a qualitative study of how the out-of-plane walls contribute to the base shear capacity of the structure has been conducted with a simplified analysis approach. It is based on the experimental data and observations, as well as simple hand calculations, and it has revealed that the out-of-plane walls can contribute to the base shear capacity directly with their out-of-plane bending resistance and indirectly by increasing the axial load exerted on the in-plane walls as the latter rocks. This observation is now to be confirmed by nonlinear finite element analyses.

A displacement-controlled pushover analysis is performed with the finite element model. To perform this analysis, the lateral displacement is imposed through two elastic beam elements that are pin-connected to the slabs, as shown in Figure 5.30. The horizontal displacement is applied to a node that is located 2/3 of the inter-story height at the second story. This is equivalent to an inverted triangular acceleration distribution. Figure 5.31 shows the base shear carried by each of the seven wall segments calculated by the nonlinear pushover analysis. The contribution of each wall to the base shear capacity is shown in columns 2 and 3 of Table 5.2. The direct contribution of the bending resistance of the out-of-plane walls to the base shear capacity is less than 5% of the total base shear capacity. The same analysis is repeated without the out-of-plane walls, and the results are shown in Figure 5.32 and in columns 4 and 5 of Table 5.2. The in-plane walls in the analysis without the out-of-plane walls carry the same load as the in-plane walls in the analysis with the out-of-plane walls. Consistent with the expectation, the capacity of the structure without the out-of-plane walls is less than that with the out-of-plane walls.

This difference is much more significant than the direct contribution of the bending resistance of the out-of-plane walls, and is mainly due to the reduction of the base-shear capacities of the in-plane walls as shown in Figure 5.31and Figure 5.32. The decrease of the in-plane walls capacities in the absence of the out-of-plane walls can be attributed to the decrease of their axial compressive loads, as discussed in Section 4.6.5. The out-of-plane walls restrained the rocking of the in-plane walls, and exerted axial compressive loads on the in-plane walls as they rocked. This is confirmed by the finite element analyses. As shown in Figure 5.33 and Figure 5.34, and summarized in Table 5.3, the axial compressive loads on the in-plane walls are a lot higher when the out-of-plane walls are present. The increase of the compressive axial loads lead to an increase of the bending moment, diagonal shear, and sliding shear capacities of the in-plane wall segments. However, the structure without the out-of-plane walls is more ductile as shown in Figure 5.32 because the wall segments have lower axial loads and thus become flexural dominated. This is supported by the crack patterns shown in Figure 5.35 and Figure 5.36.

Table 5.1 - Calibration of material parameters for the analysis

Type of the element	Material parameter	In-plane walls	Out-of-plane walls	Slabs
Cohesive Interfaces at the base	Tensile strength, s_o (ksi)	0.2	0.2	N/A
	Initial and residual dilatation coefficient, $\zeta_{dil,o} / \zeta_{dil,r}$	0.01	0.01	N/A
	Initial and residual coefficient of friction, μ_o / μ_r	0.7	0.7	N/A
	G_f^I (kip/in)	0.0004	0.0004	N/A
	G_f^{II} (kip/in)	0.004	0.004	N/A
	r_o / r_r	0.05 /0.01	0.05 /0.01	N/A
All other cohesive Interfaces	Tensile strength, s_o (ksi)	0.4	0.4	N/A
	Initial and residual dilatation coefficient, $\zeta_{dil,o} / \zeta_{dil,r}$	0.3	0.3	N/A
	Initial and residual coefficient of friction, μ_o / μ_r	1.5	1.5	N/A
	G_f^I (kip/in)	0.0004	0.0004	N/A
	G_f^{II} (kip/in)	0.004	0.004	N/A
	r_o / r_r	0.05 /0.01	0.05 /0.01	N/A
Smear cracked shell	Thickness (in.)	3.8125	7.625	11
	Elastic modulus E_c (psi)	1500	1500	3200
	Tensile strength, f_t (ksi)	0.4	0.4	0.4
	f_o (ksi)	1.0	1.0	2.7
	Compressive strength, f_c' (ksi)	2.5	2.5	4
	ε_u	0.02	0.02	0.02
	ε_1	0.0025	0.0025	0.0025
Steel truss	Size	No 4	No 4	smeared
	Yield strength, f_y (ksi)	63.2	63.2	68
	Tensile strength, f_u (ksi)	102.7	102.7	N/A
	Elastic modulus, E_s (ksi)	29000	29000	29000
	ε_{sh}'	0.01	0.01	N/A
	$f_{sh,1}$ (ksi)	80	80	N/A
	$\varepsilon_{sh,1}'$	0.02	0.02	N/A
	Ultimate strain, ε_u'	0.15	0.15	N/A
Bond-slip/dowel action interface	Dowel strength, F_y (kips)	2.1	4.2	N/A
	Loading stiffness (kips/in)	523	523	N/A
	Unloading stiffness (kips/in)	2615	2615	N/A
	Grout strength, f_c' (ksi)	3.5	3.5	N/A

Table 5.2 - Contribution of each wall to the base shear capacity

	Base Shear (kips)				**Base shear difference (kips)**	
	With out-of-plane walls		Without out-of-plane walls			
	Positive direction	Negative direction	Positive direction	Negative direction	Positive direction	Negative direction
W-1	35.58	84.14	5.85	71.21	29.73	12.93
W-2	79.30	55.86	68.94	43.23	10.37	12.63
W-3	99.09	60.15	83.85	32.21	15.24	27.94
W-4/5	1.92	8.03	0.00	0.00	1.92	8.03
W-6/7	8.02	2.35	0.00	0.00	8.02	2.35
total	223.91	210.53	158.63	146.65	65.28	63.88

Table 5.3 - Axial load distibution

	Axial load (kips)				**Axial load difference (kips)**	
	With out-of-plane walls		Without out-of-plane walls			
	Positive direction	Negative direction	Positive direction	Negative direction	Positive direction	Negative direction
W-1	5.34	-143.83	75.56	-102.37	-70.23	-41.46
W-2	-84.82	-58.94	-51.22	-17.07	-33.60	-41.87
W-3	-132.54	-29.62	-96.52	47.00	-36.02	-76.62
W-4/5	83.98	1.59	0.00	0.00	83.98	1.59
W-6/7	-13.33	89.77	0.00	0.00	-13.33	89.77
total	-141.36	-141.03	-72.17	-72.44	-69.19	-68.59

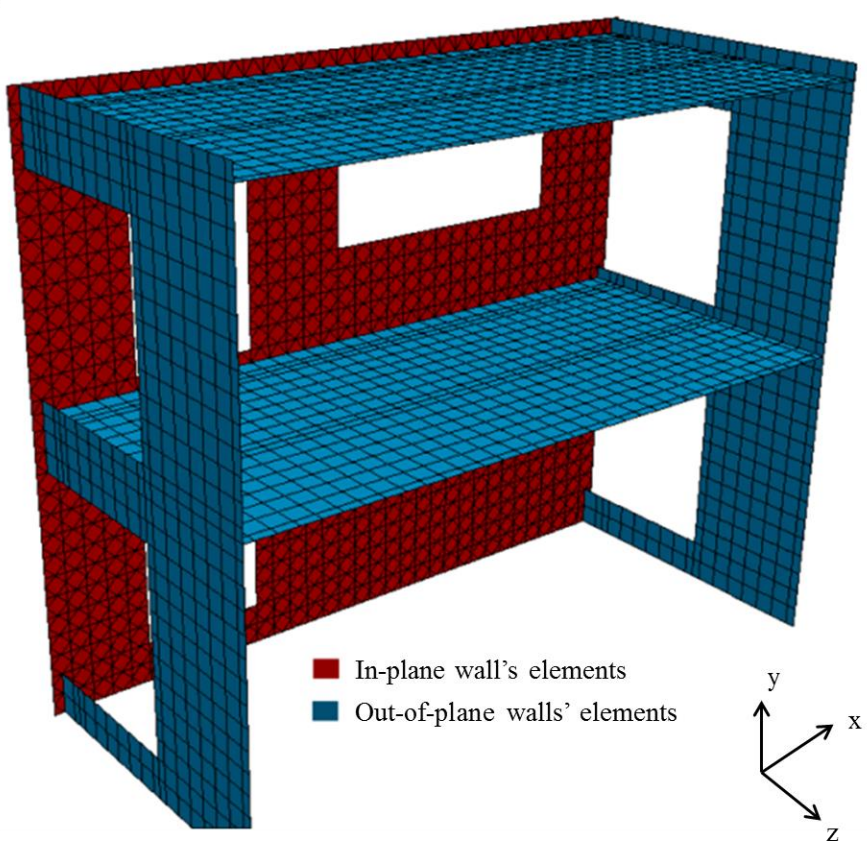

Figure 5.1 - Discretization of the model

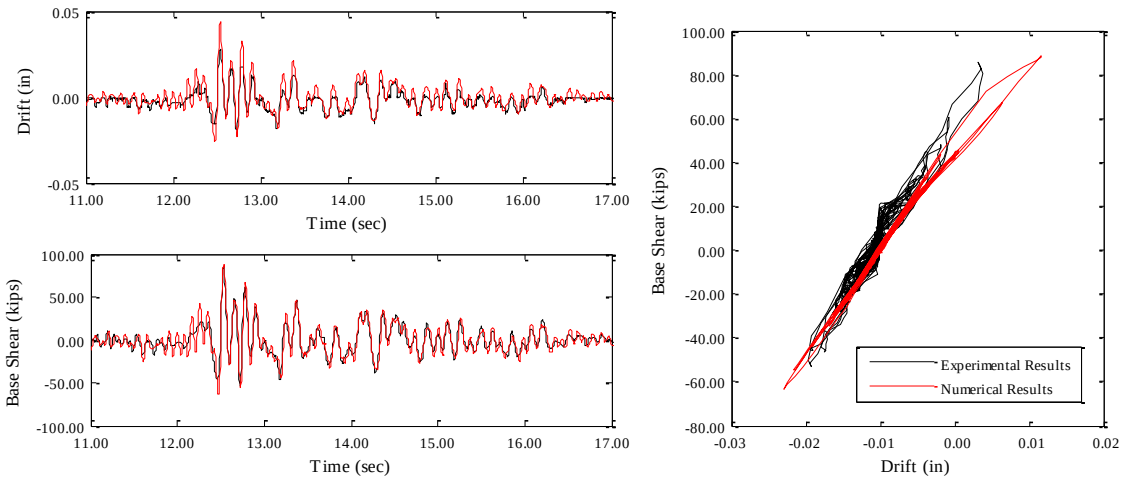

Figure 5.2 - Comparison of the experimental and numerical results on the first-story drift time history, base shear time history and base shear vs first-story drift for El Centro 43%

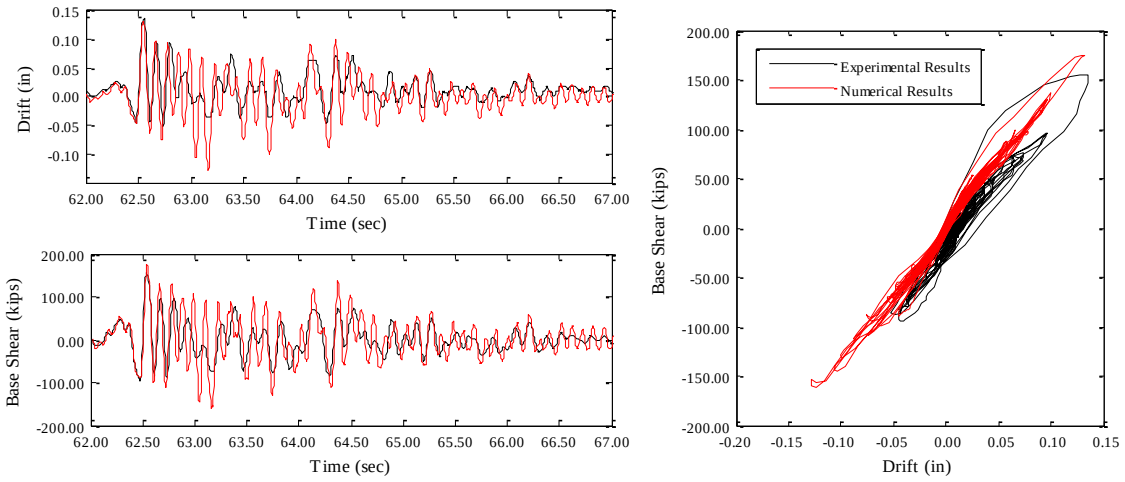

Figure 5.3 - Comparison of the experimental and numerical results on the first-story drift time history, base shear time history and base shear vs first-story drift for El Centro 86%

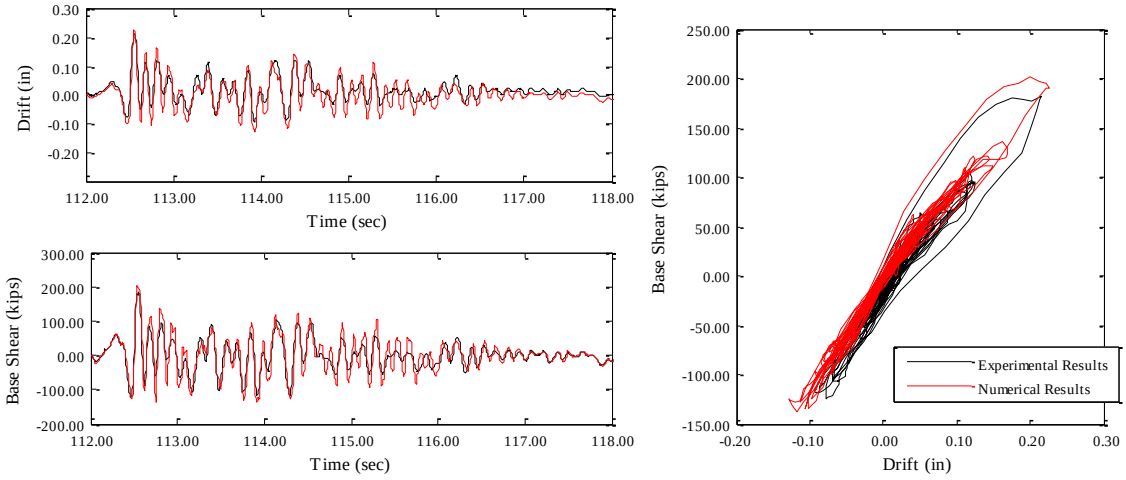

Figure 5.4 - Comparison of the experimental and numerical results on the first-story drift time history, base shear time history and base shear vs first-story drift for El Centro 108%

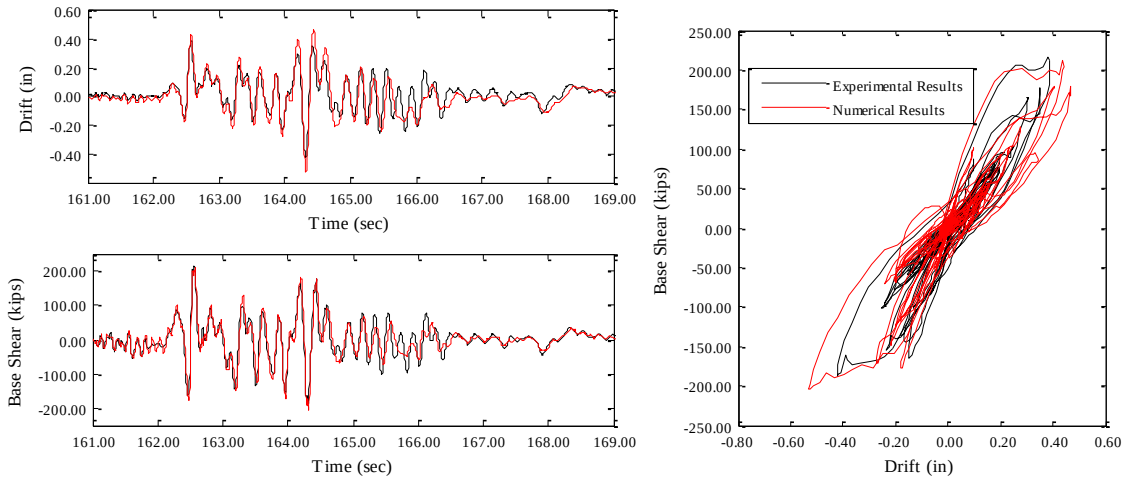

Figure 5.5 - Comparison of the experimental and numerical results on the first-story drift time history, base shear time history and base shear vs first-story drift for El Centro 145%

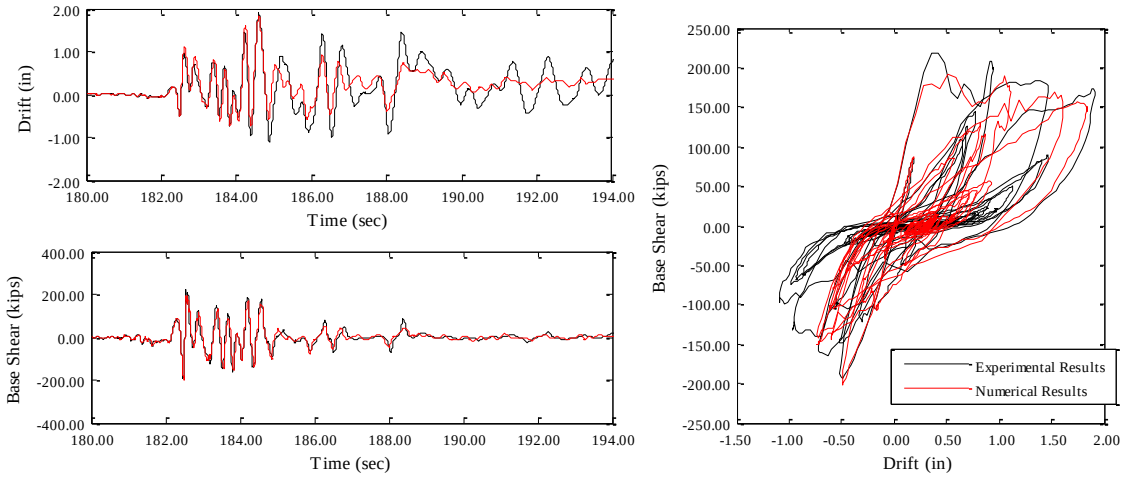

Figure 5.6 - Comparison of the experimental and numerical results of the first-story drift time history, base shear time history and base shear vs first-story drift during El Centro 160%

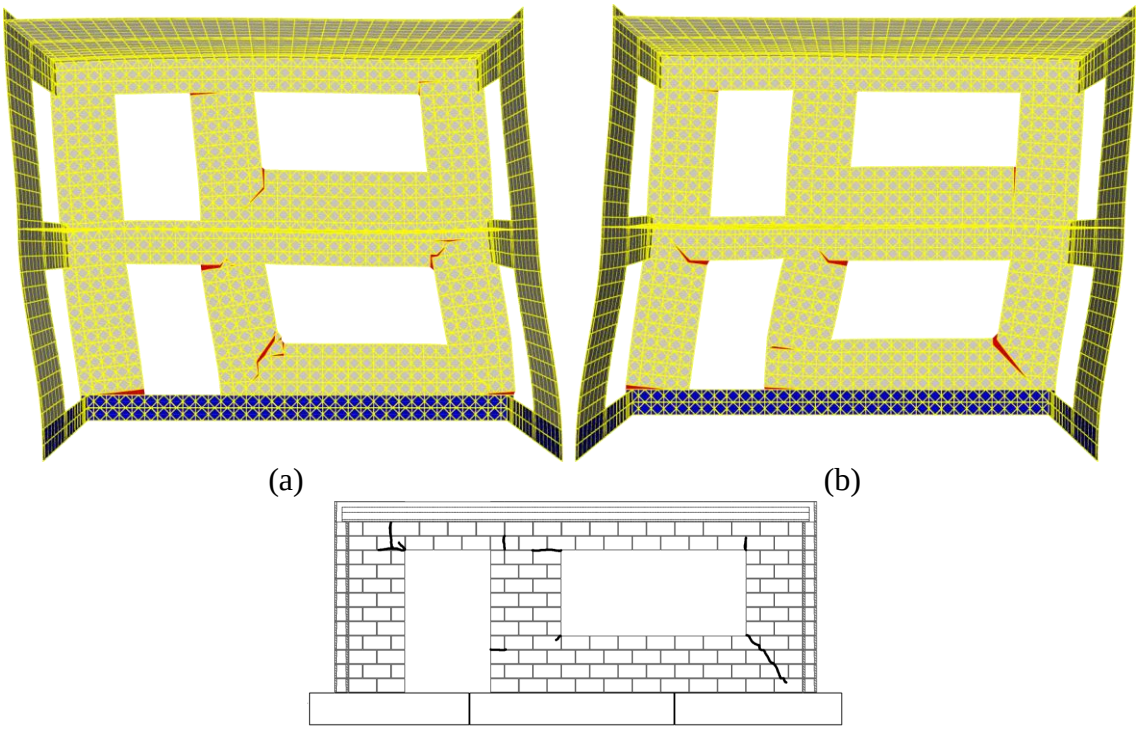

Figure 5.7 - Deformed mesh for a) negative drift, b) positive drift (the displacements are amplified by 100 times for illustration purposes); and c) actual crack pattern for the 1st story during El Centro 86%

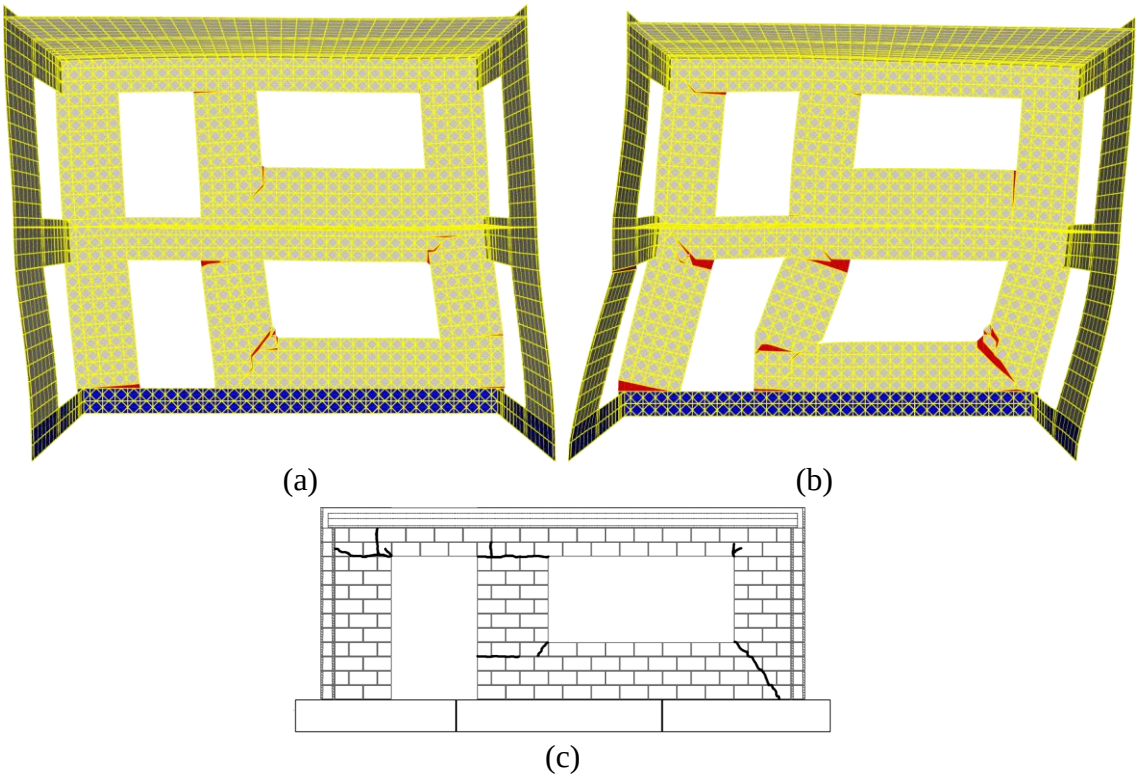

Figure 5.8 - Deformed mesh for a) negative drift, b) positive drift (the displacements are amplified by 100 times for illustration purposes); and c) actual crack pattern for the 1st story during El Centro 108%

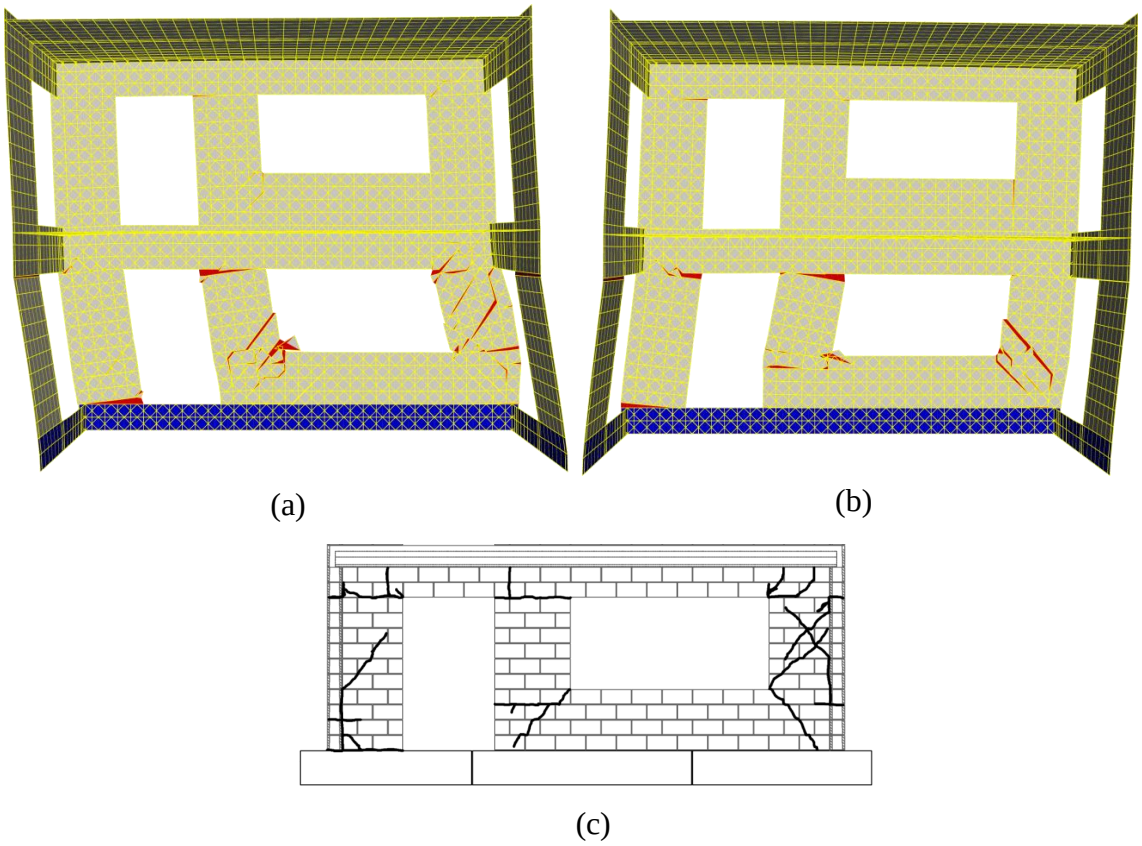

Figure 5.9 - Deformed mesh for a) negative drift, b) positive drift (the displacements are amplified by 30 times for illustration purposes); and c) actual crack pattern for the 1st story during El Centro 145%

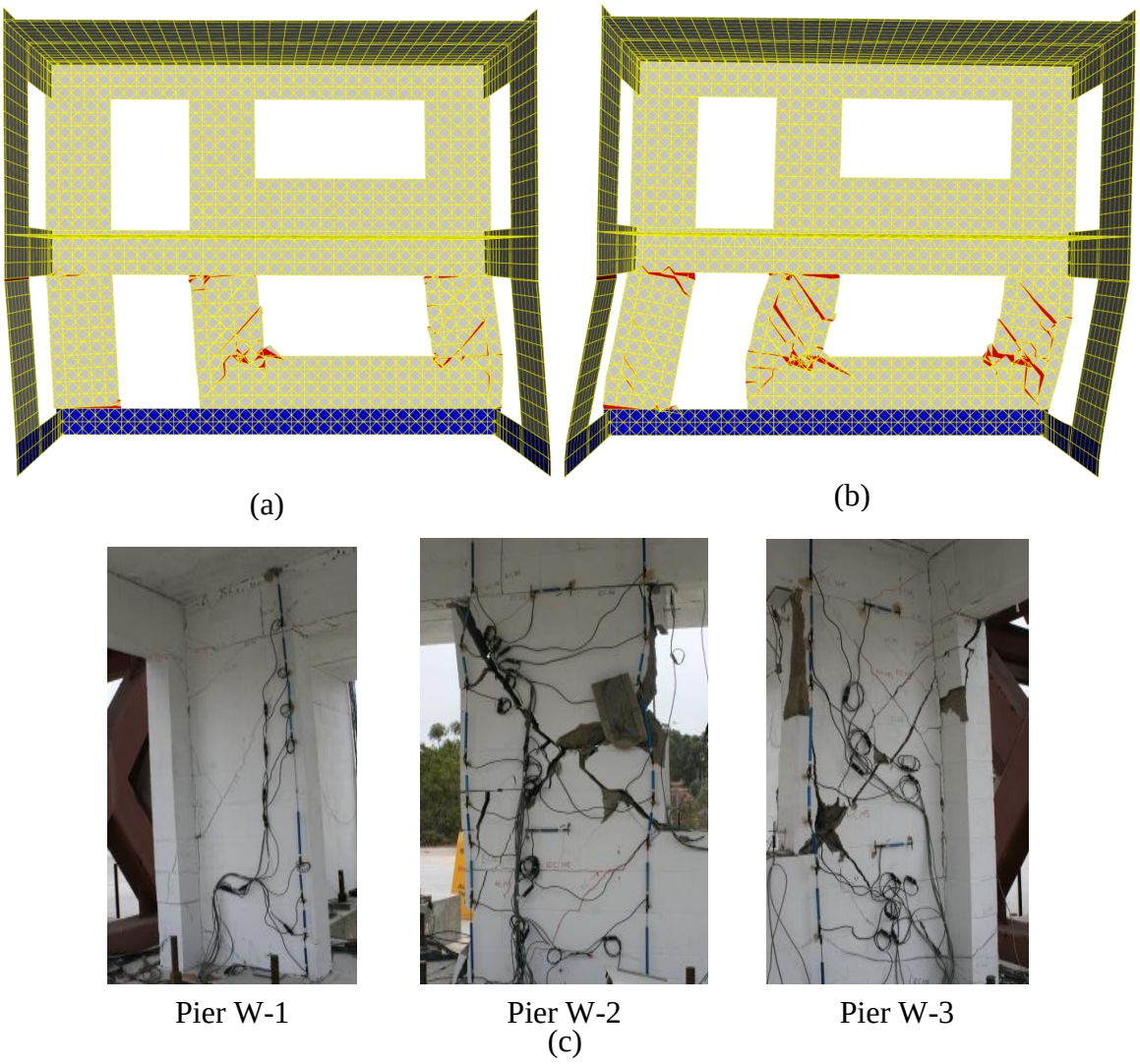

Figure 5.10 - Deformed mesh for a) negative drift, b) positive drift (the displacements are amplified by 10 times for illustration purposes); and c) actual crack pattern for the 1st story during El Centro 160%

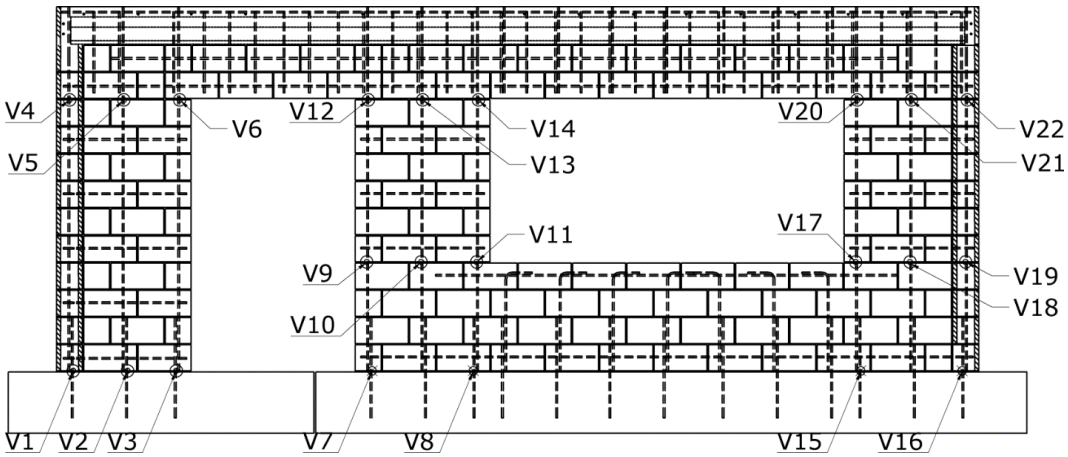

Figure 5.11 - Locations where the numerically computed and experimentally recorded strains are compared.

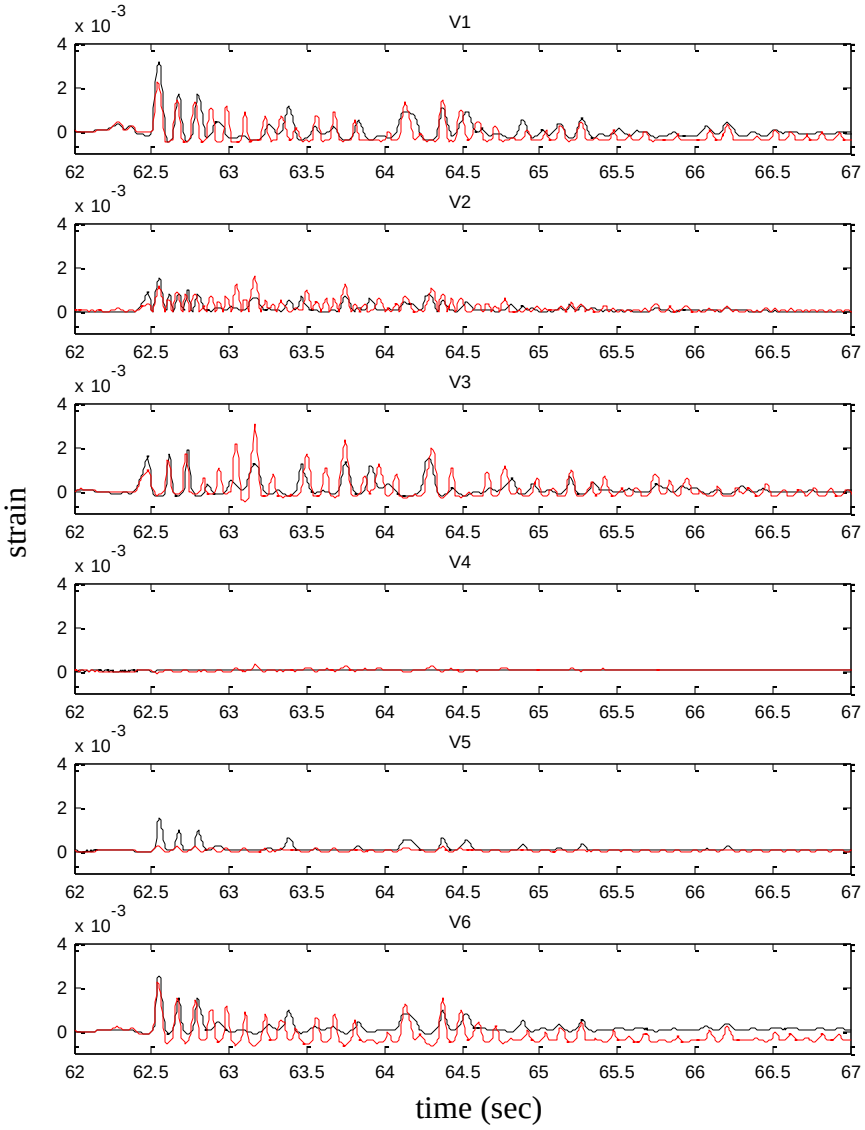

Figure 5.12 - Comparison of the experimentally recorded and numerically computed strain time histories for W-1 vertical reinforcing bars during El Centro 86% (black=experiment, red=analysis)

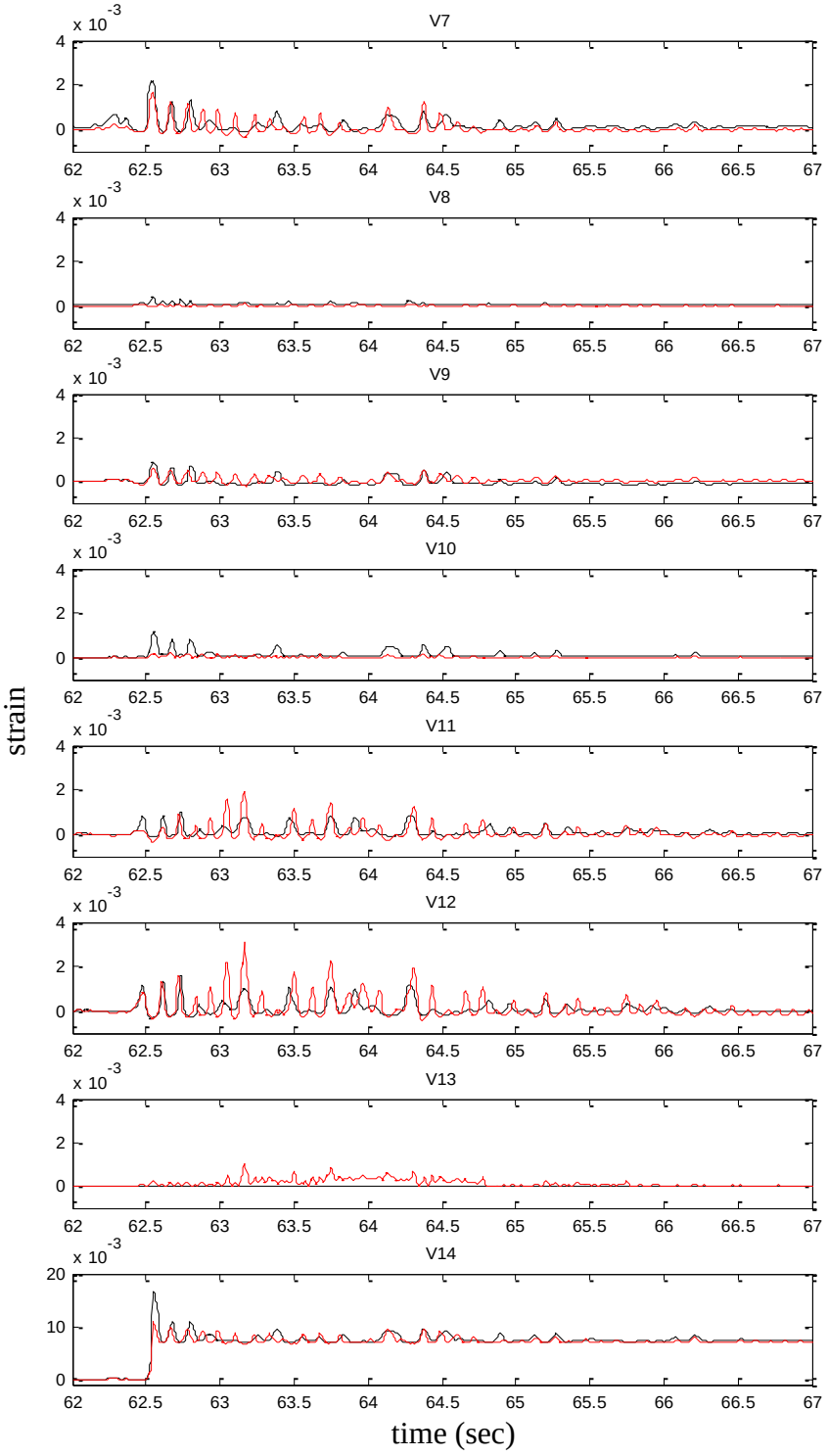

Figure 5.13 - Comparison of the experimentally recorded and numerically computed strain time histories for W-2 vertical reinforcing bars during El Centro 86% (black=experiment, red=analysis)

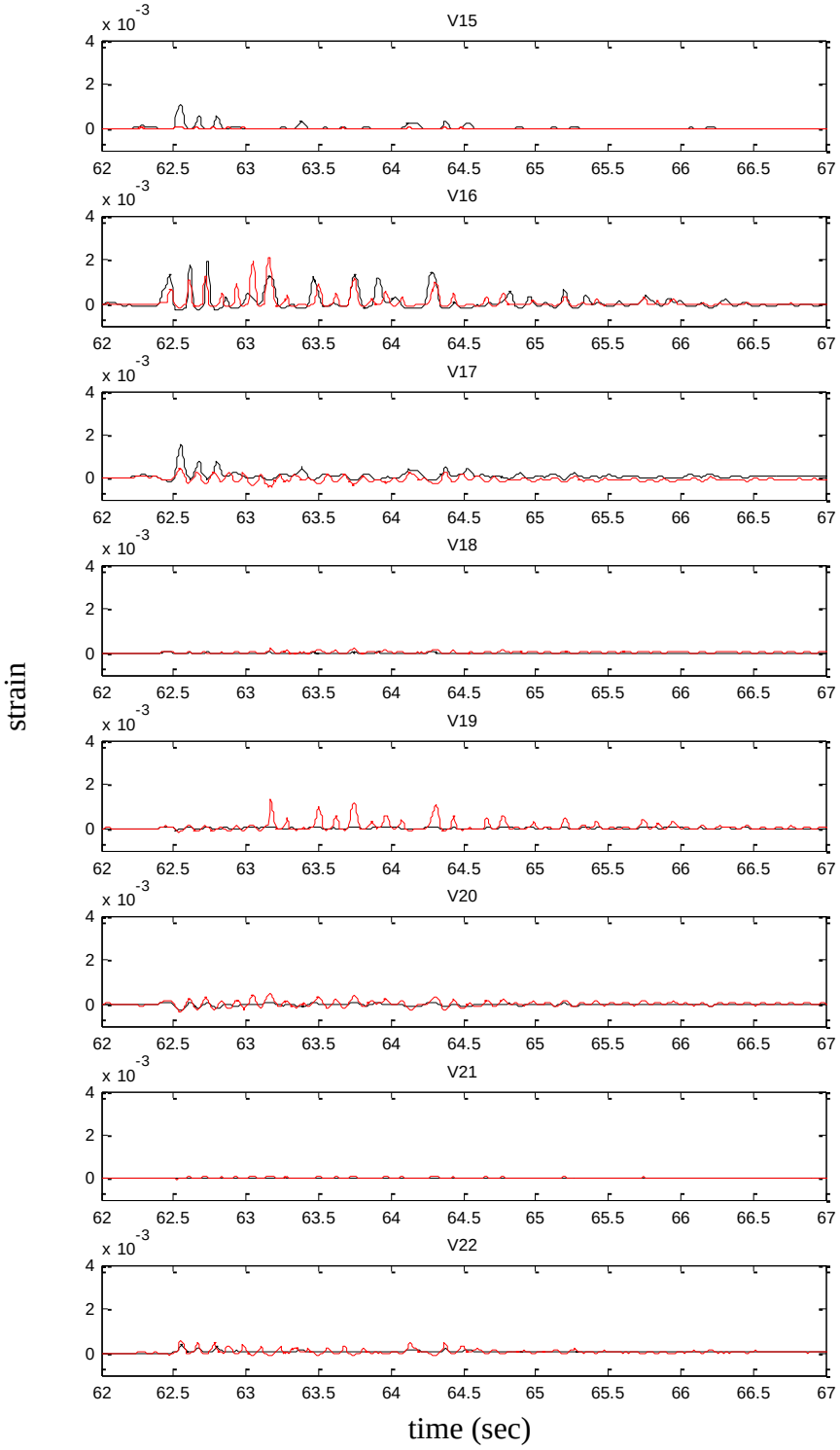

Figure 5.14 - Comparison of the experimentally recorded and numerically computed strain time histories for W-3 vertical reinforcing bars during El Centro 86% (black=experiment, red=analysis)

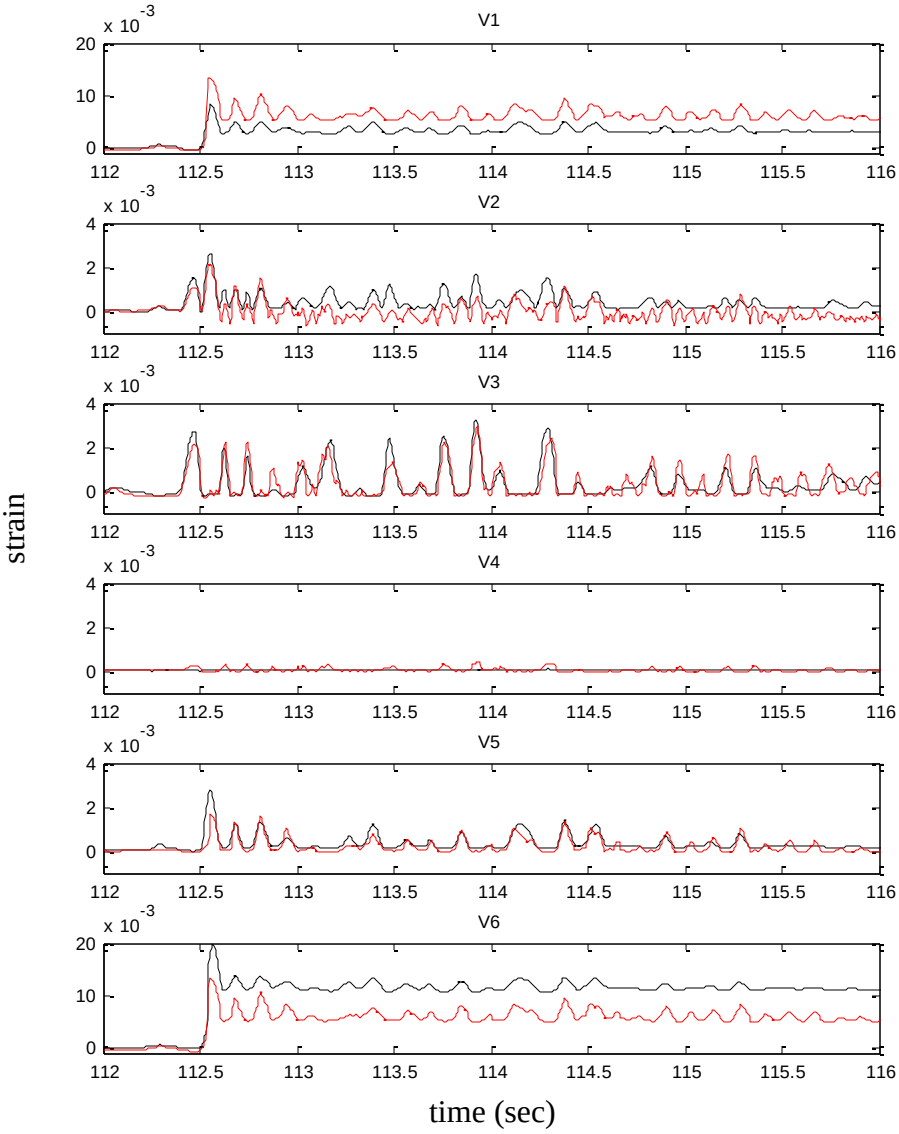

Figure 5.15 - Comparison of the experimentally recorded and numerically computed strain time histories for W-1 vertical reinforcing bars during El Centro 108% (black=experiment, red=analysis)

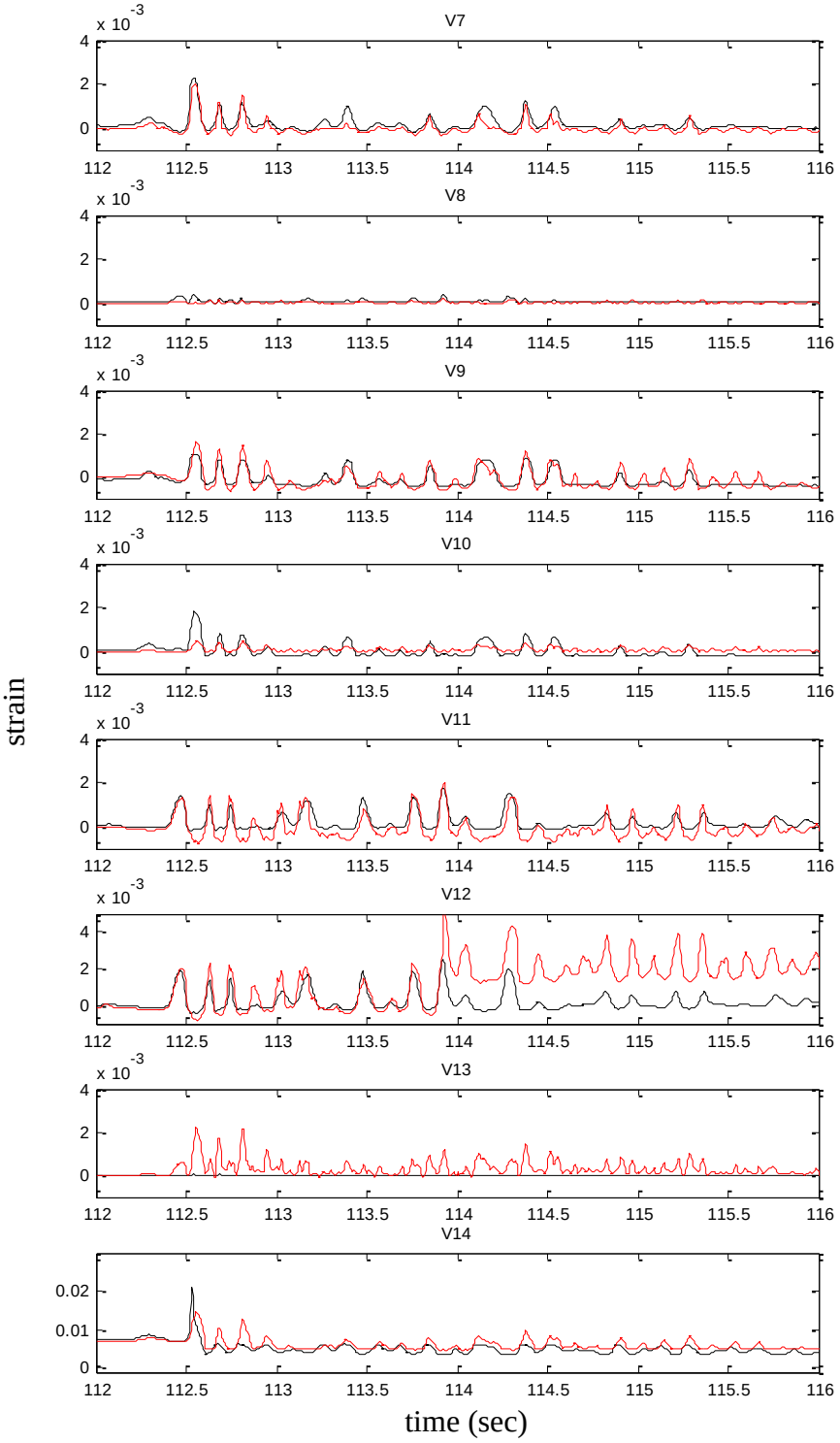

Figure 5.16 - Comparison of the experimentally recorded and numerically computed strain time histories for W-2 vertical reinforcing bars during El Centro 108% (black=experiment, red=analysis)

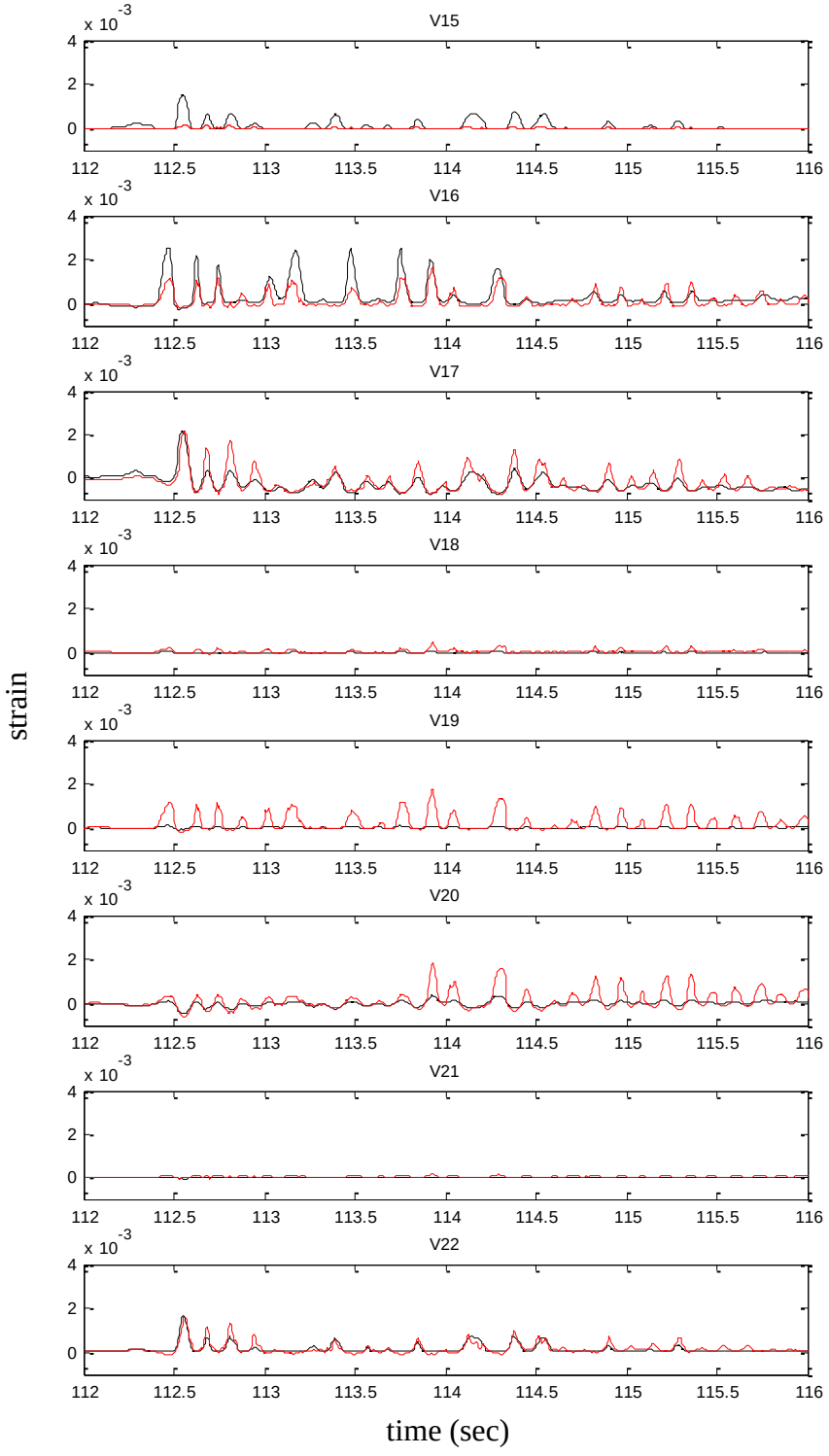

Figure 5.17 - Comparison of the experimentally recorded and numerically computed strain time histories for W-3 vertical reinforcing bars during El Centro 108% (black=experiment, red=analysis)

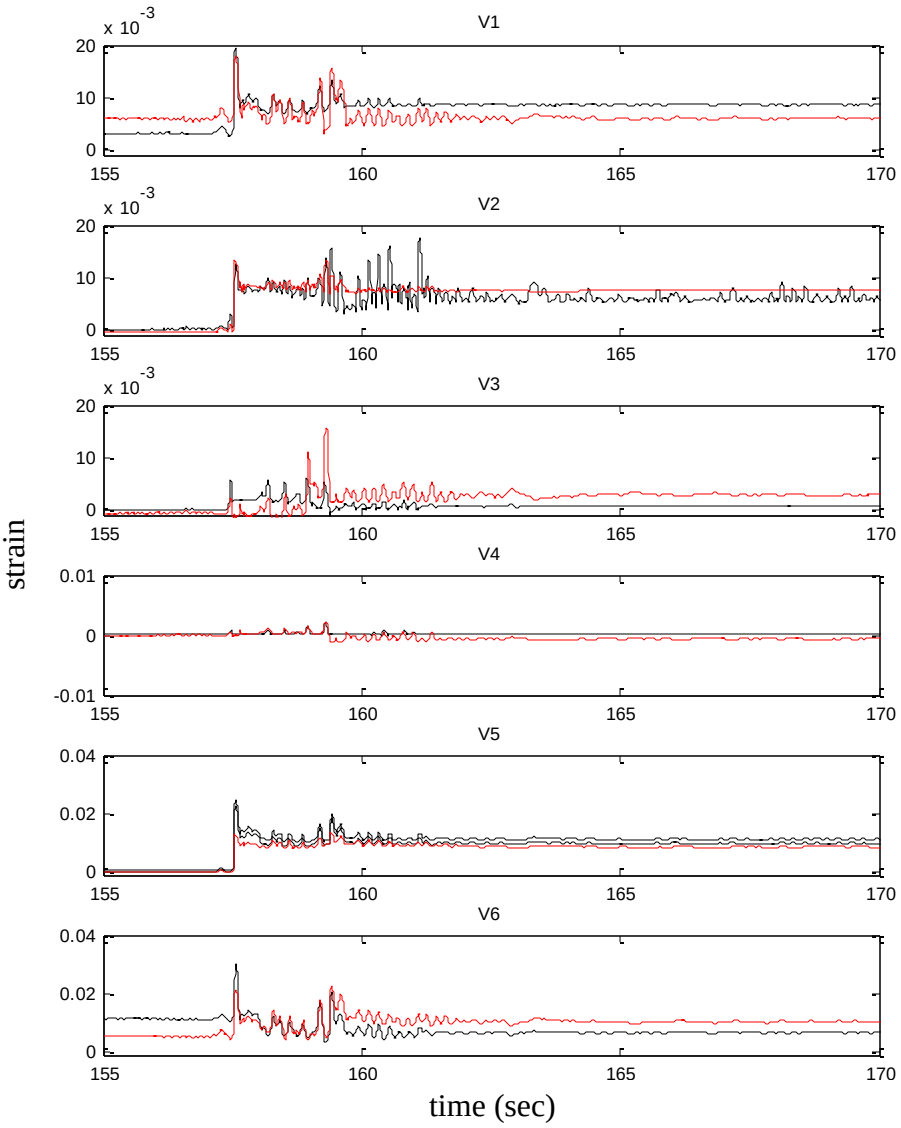

Figure 5.18 - Comparison of the experimentally recorded and numerically computed strain time histories for W-1 vertical reinforcing bars during El Centro 145% (black=experiment, red=analysis)

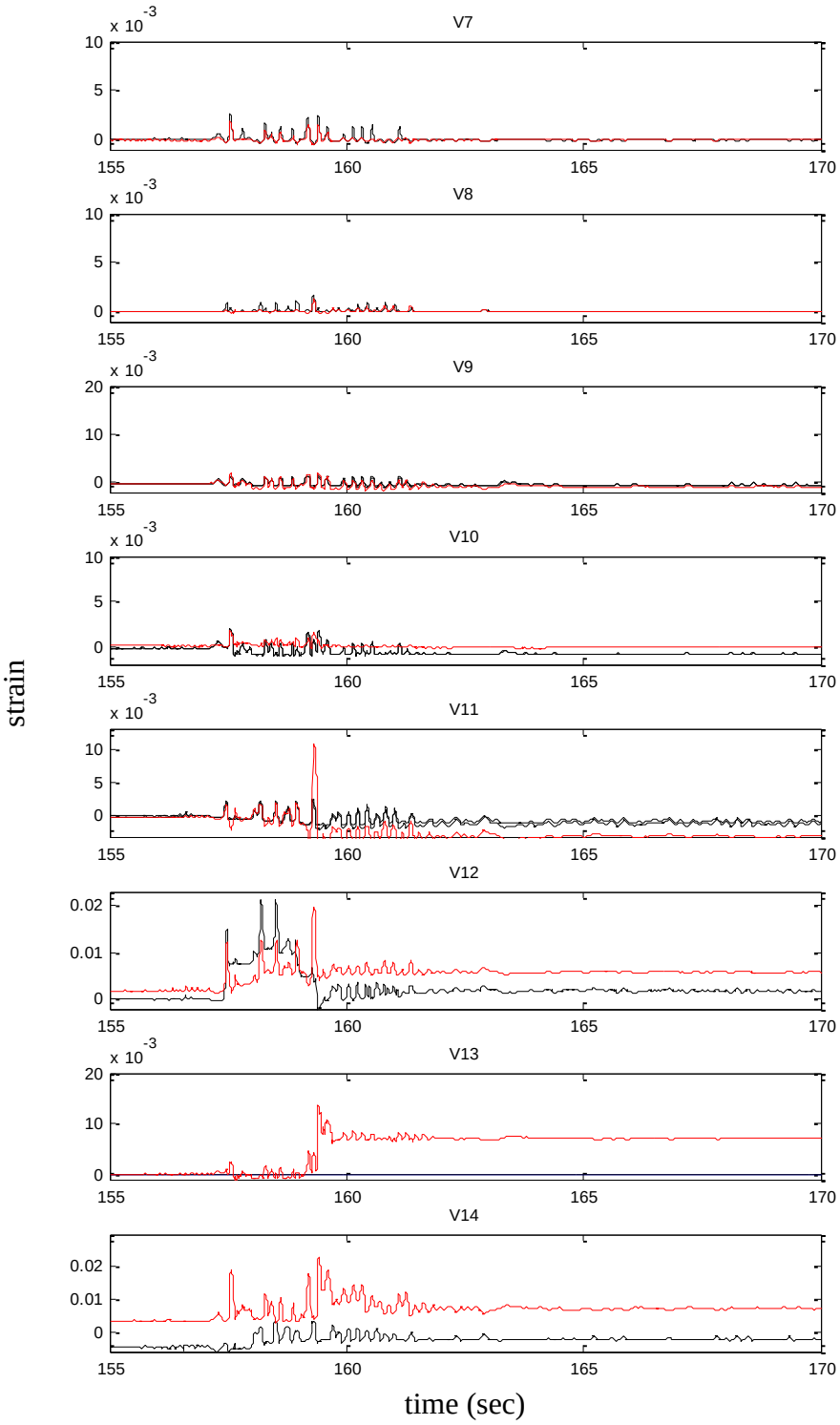

Figure 5.19- Comparison of the experimentally recorded and numerically computed strain time histories for W-2 vertical reinforcing bars during El Centro 145% (black=experiment, red=analysis)

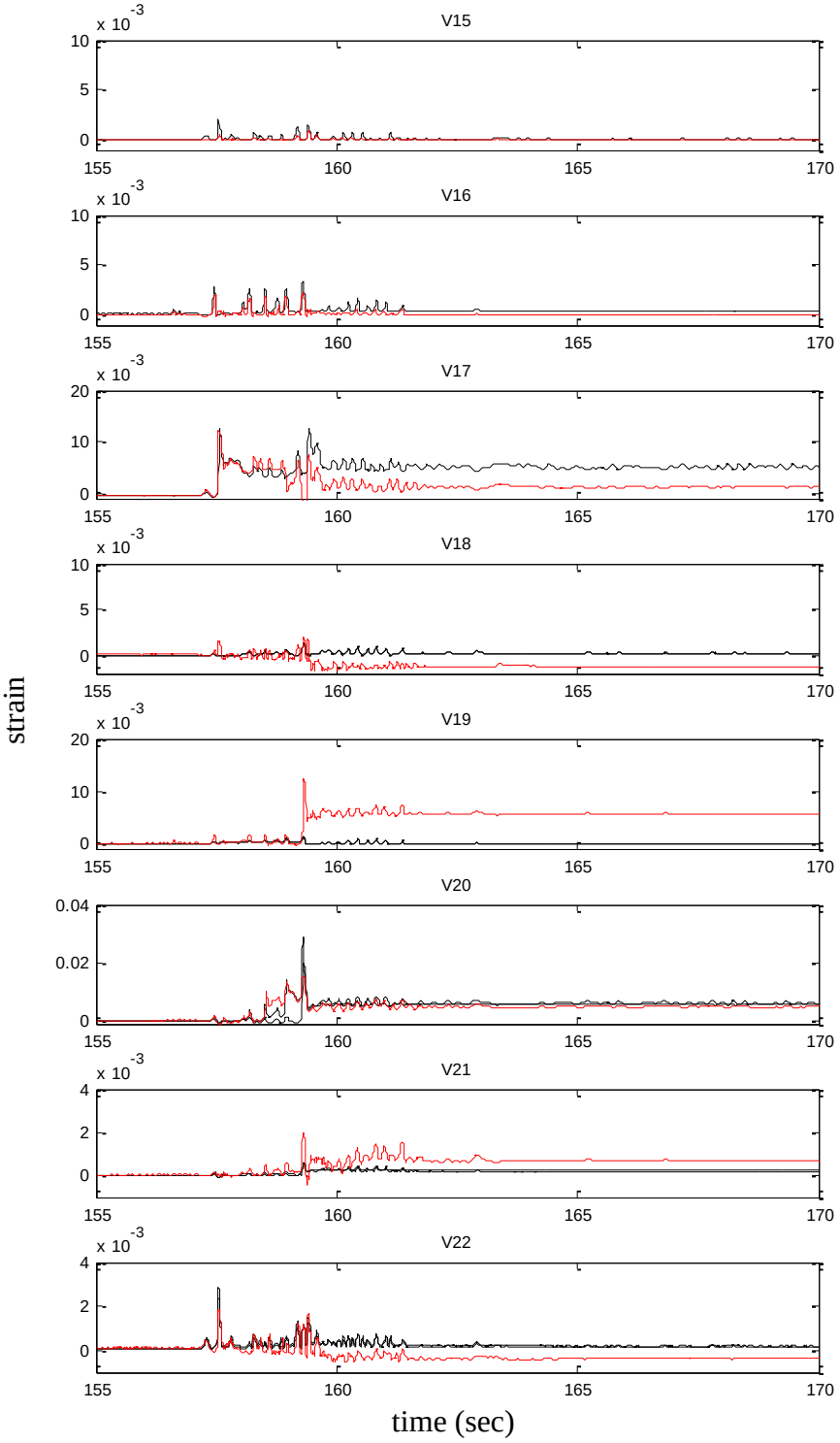

Figure 5.20 - Comparison of the experimentally recorded and numerically computed strain time histories for W-3 vertical reinforcing bars during El Centro 145% (black=experiment, red=analysis)

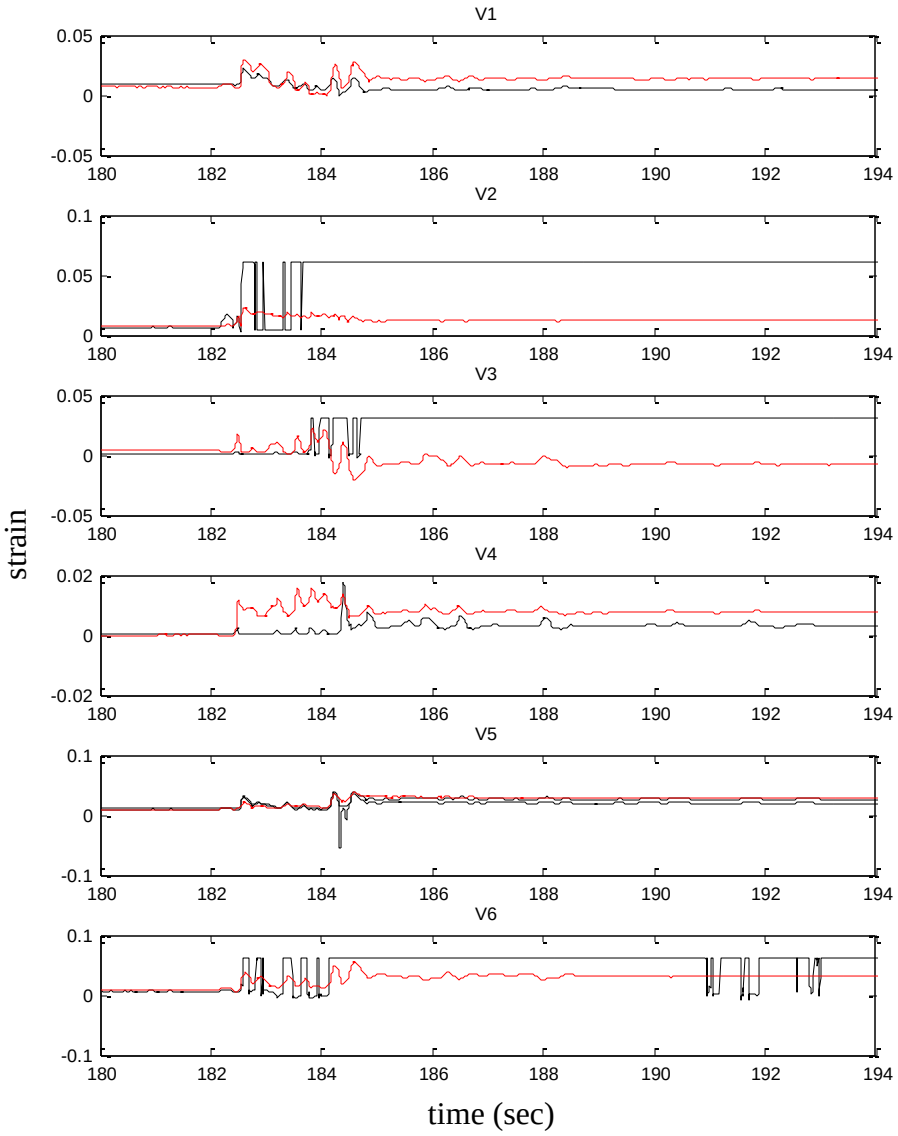

Figure 5.21 - Comparison of the experimentally recorded and numerically computed strain time histories for W-1 vertical reinforcing bars during El Centro 160% (black=experiment, red=analysis)

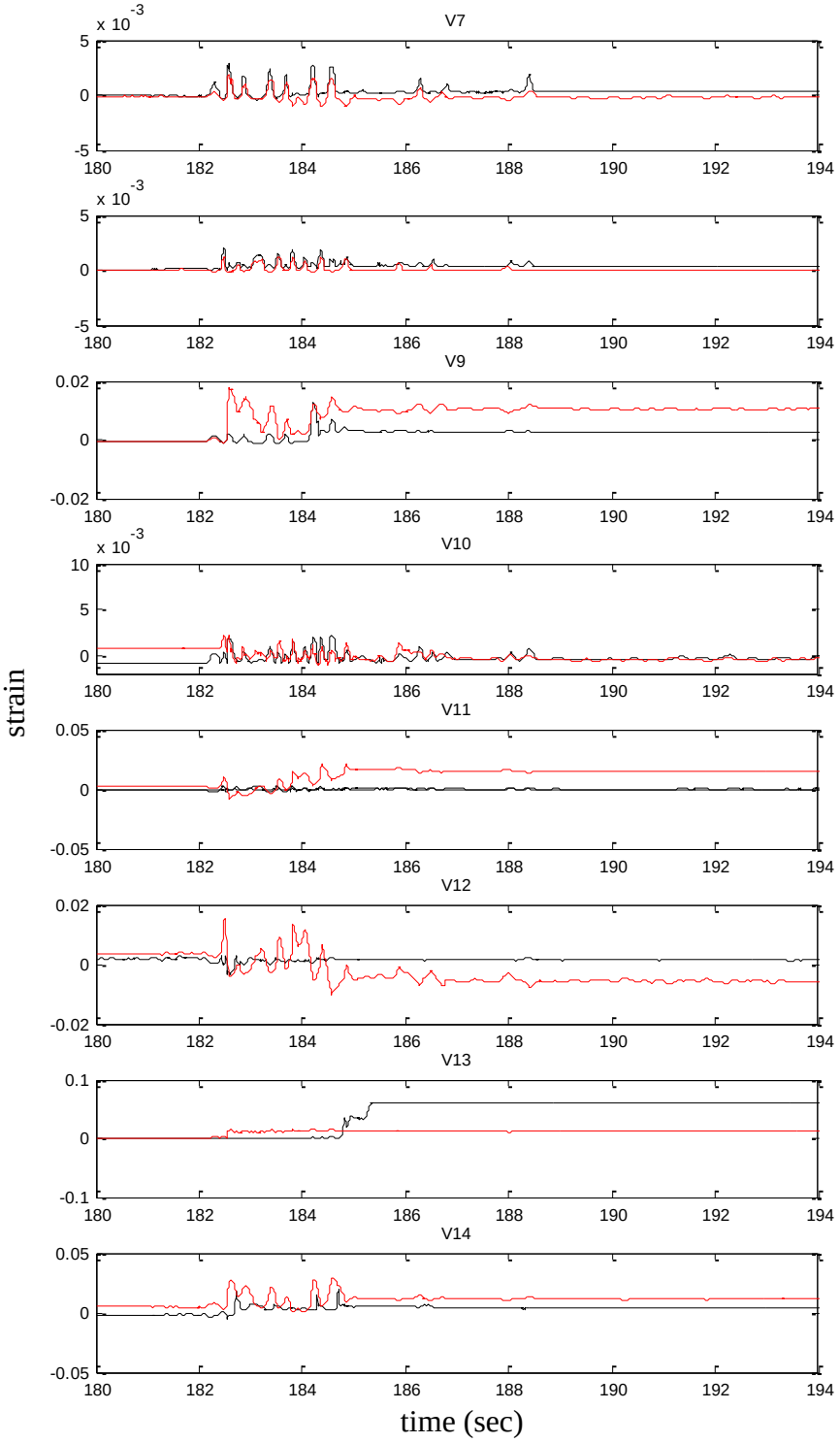

Figure 5.22- Comparison of the experimentally recorded and numerically computed strain time histories for W-2 vertical reinforcing bars during El Centro 160% (black=experiment, red=analysis)

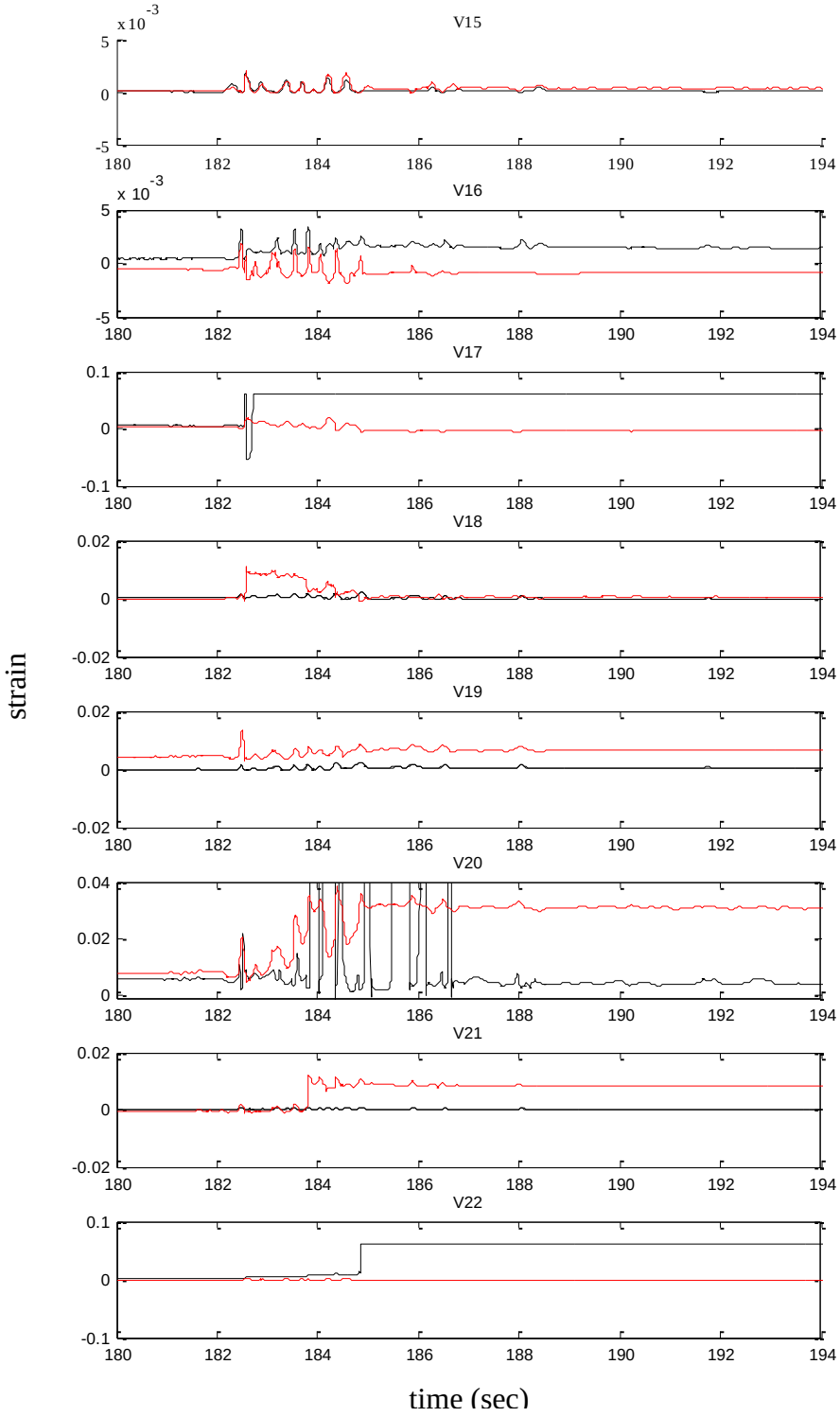

Figure 5.23 - Comparison of the experimentally recorded and numerically computed strain time histories for W-3 vertical reinforcing bars during El Centro 160% (black=experiment, red=analysis)

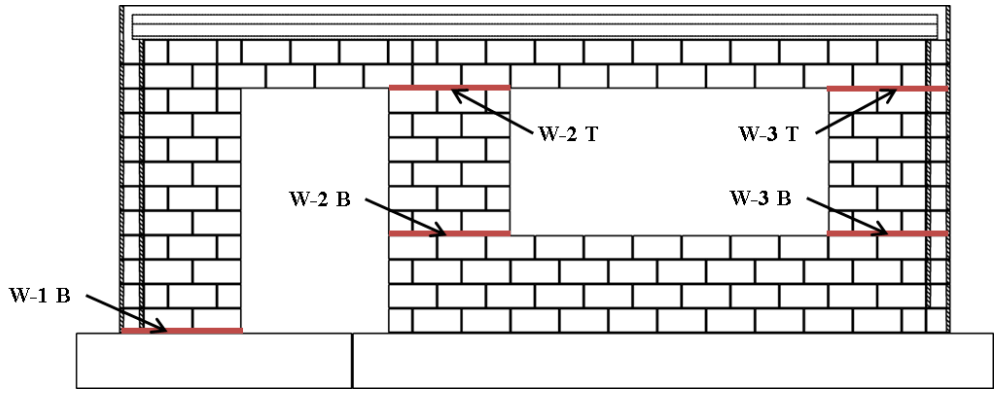

Figure 5.24 - Locations where the numerically computed and experimentally recorded sliding is compared.

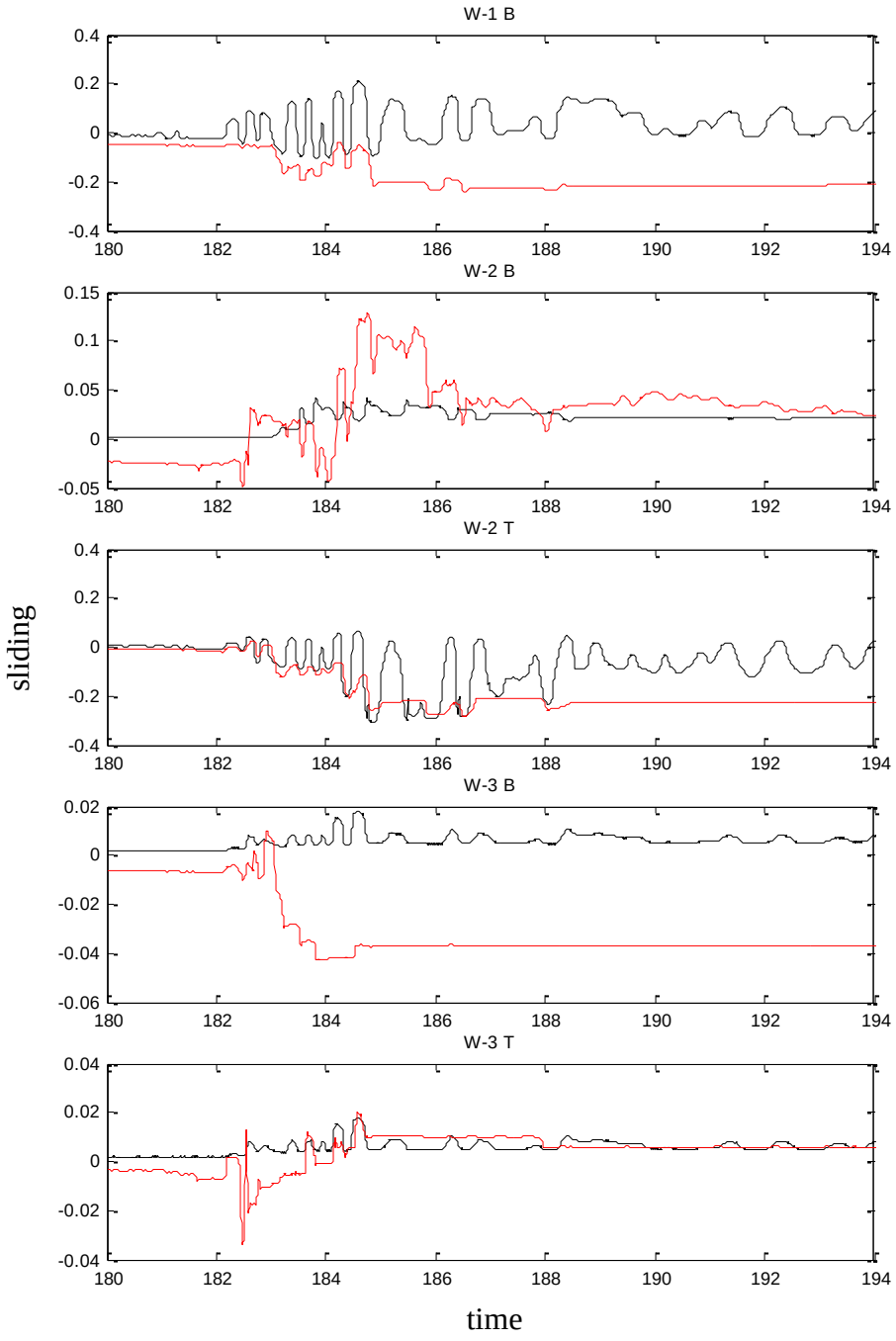

Figure 5.25 - Comparison of the experimentally recorded and numerically computed sliding time histories at selected locations during El Centro 160% (black=experiment, red=analysis)

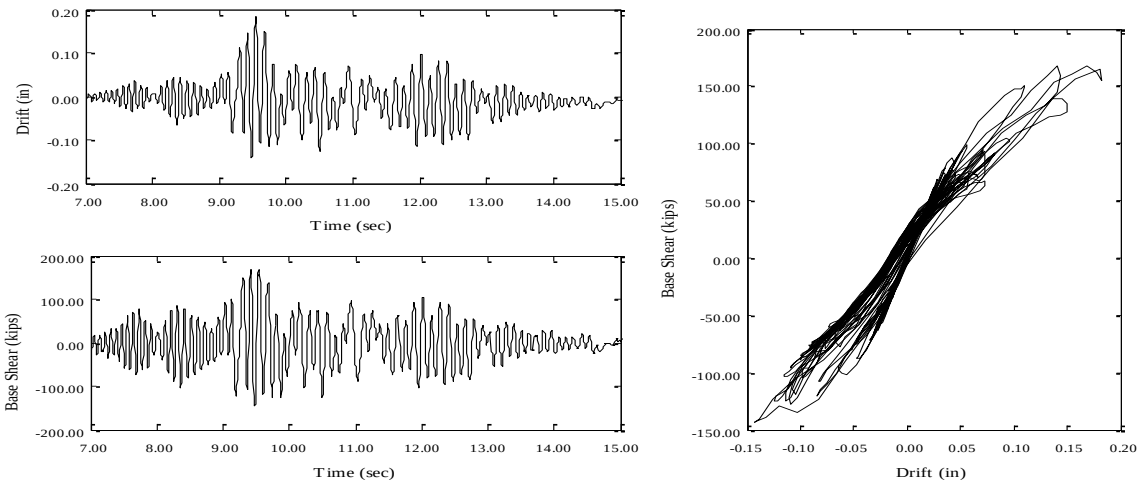

Figure 5.26 - First-story drift time history, base shear time history and base shear vs. first-story drift from the analysis with the DE (El Centro 85%) applied directly to the undamaged structure

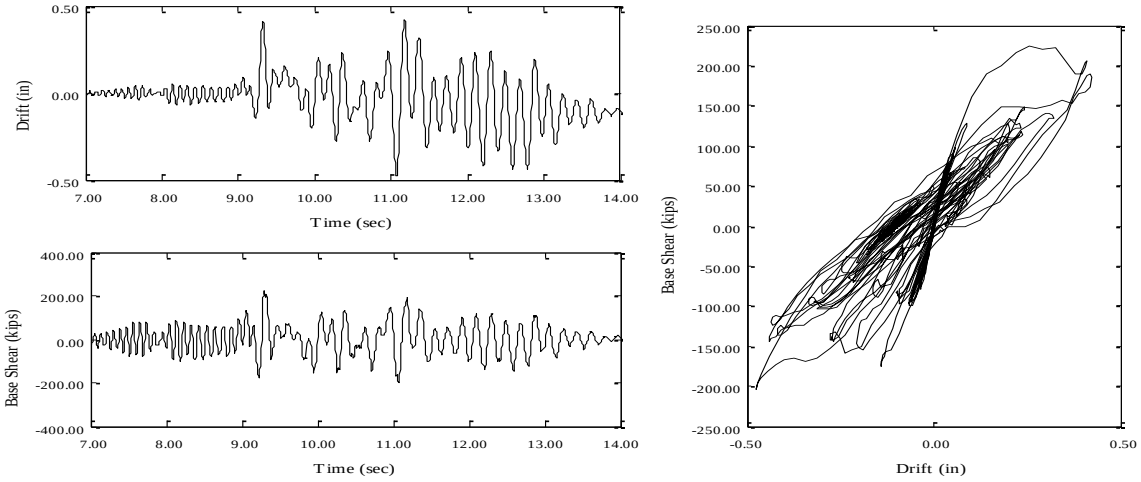

Figure 5.27 - First-story drift time history, base shear time history and base shear vs. first-story drift from the analysis with the MCE (El Centro 128%) applied directly to the undamaged structure

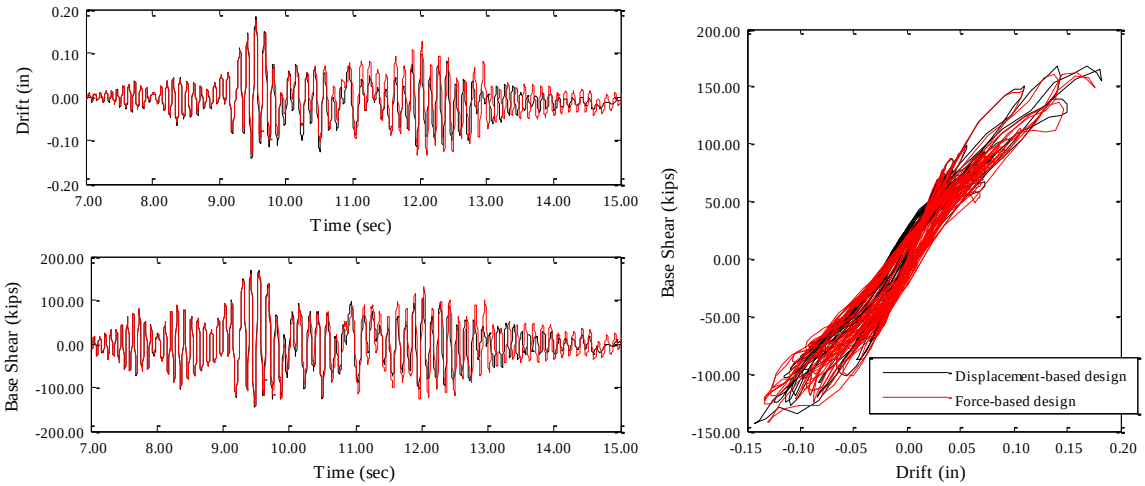

Figure 5.28 – Comparison of the displacement-based and forced-based designs with the DE (El Centro 85%) applied directly to the undamaged structures

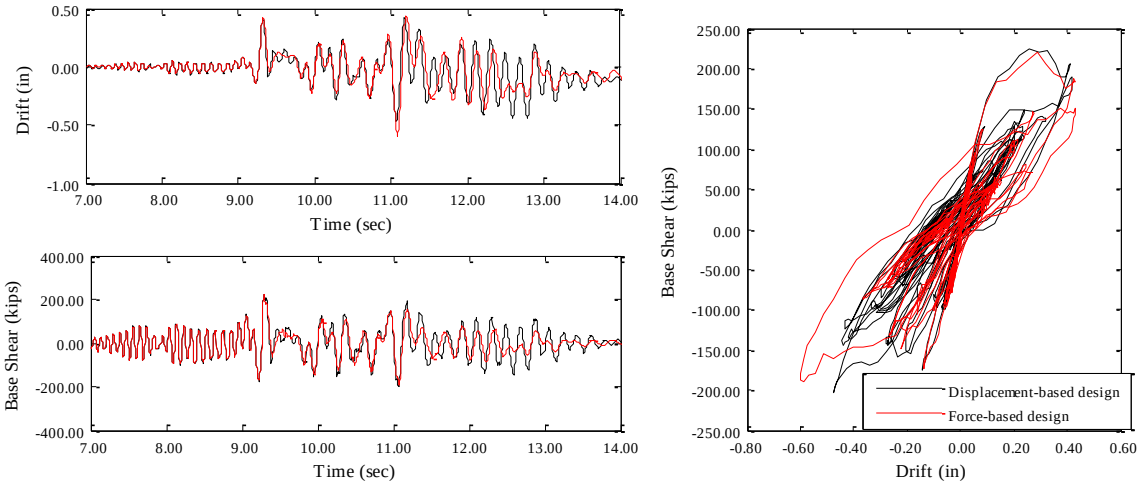

Figure 5.29 – Comparison of the displacement-based and forced-based designs with the MCE (El Centro 128%) applied directly to the undamaged structures

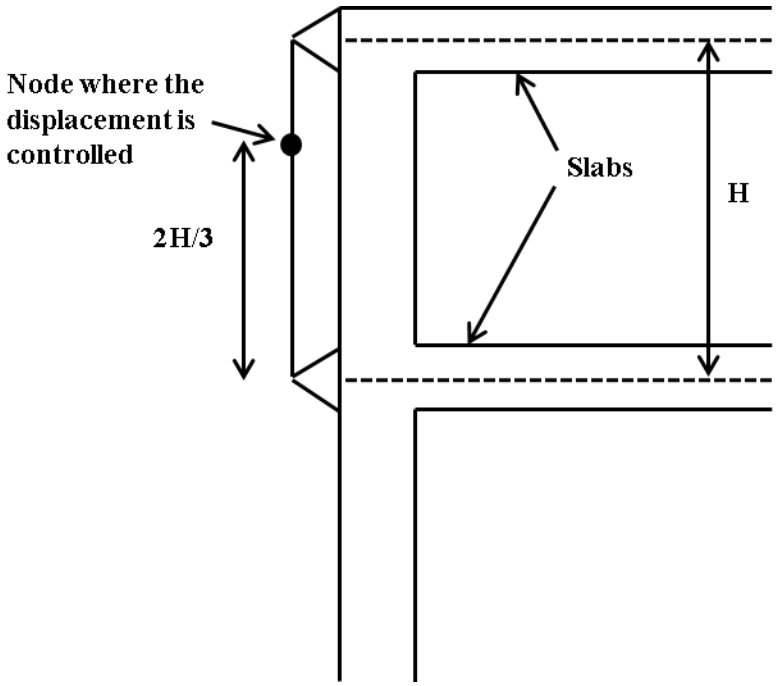

Figure 5.30 – Loading scheme for the pushover analysis

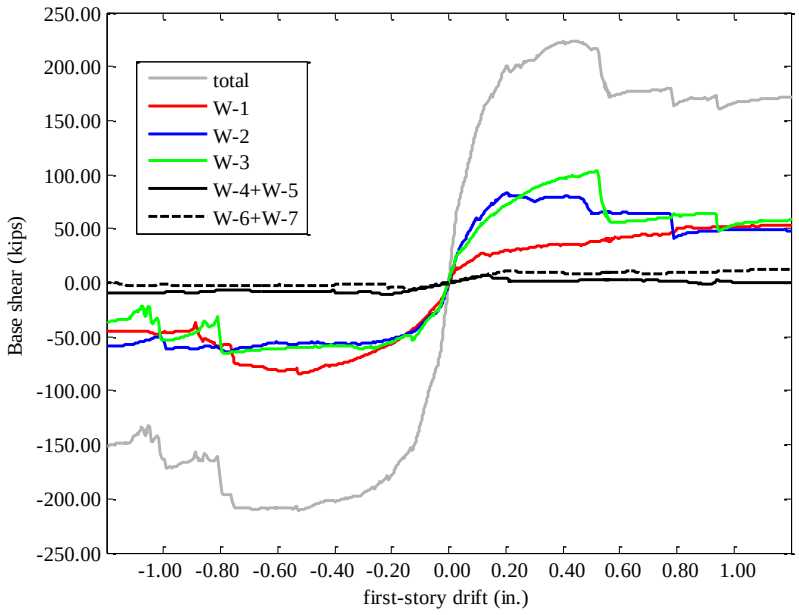

Figure 5.31 – Base shear-vs-first-story drift from pushover analysis with the out-of-plane walls

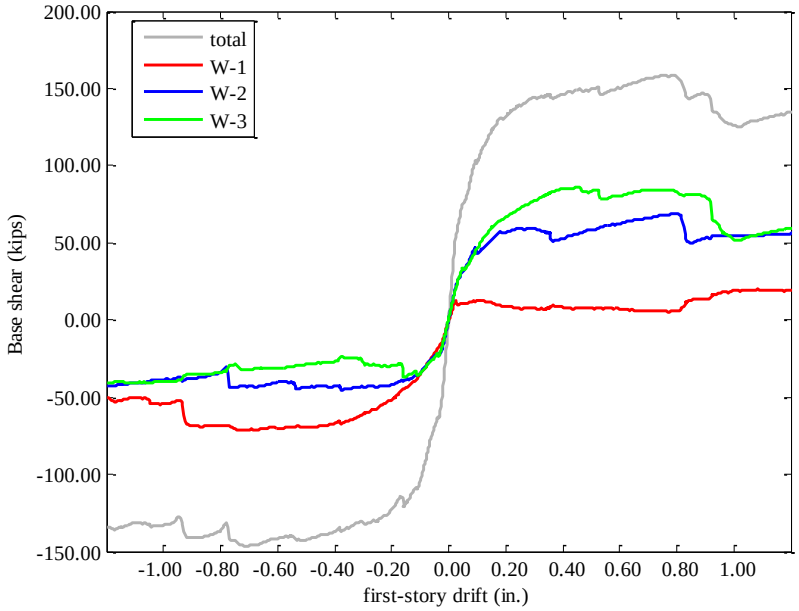

Figure 5.32 – Base shear-vs-first-story drift from pushover analysis without the out-of-plane walls

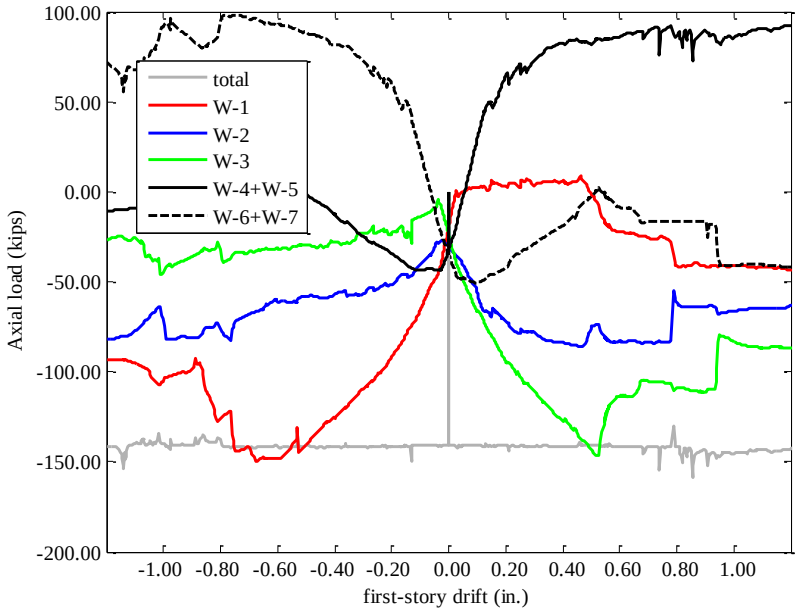

Figure 5.33 - Axial load-vs-first-story drift from pushover analysis with the out-of-plane walls

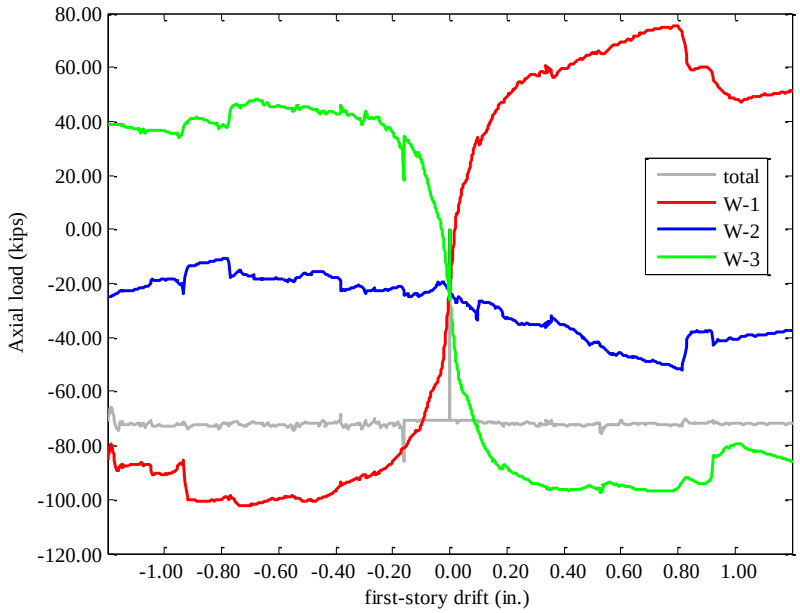

Figure 5.34 - Axial load-vs-first-story drift from pushover analysis without the out-of-plane walls

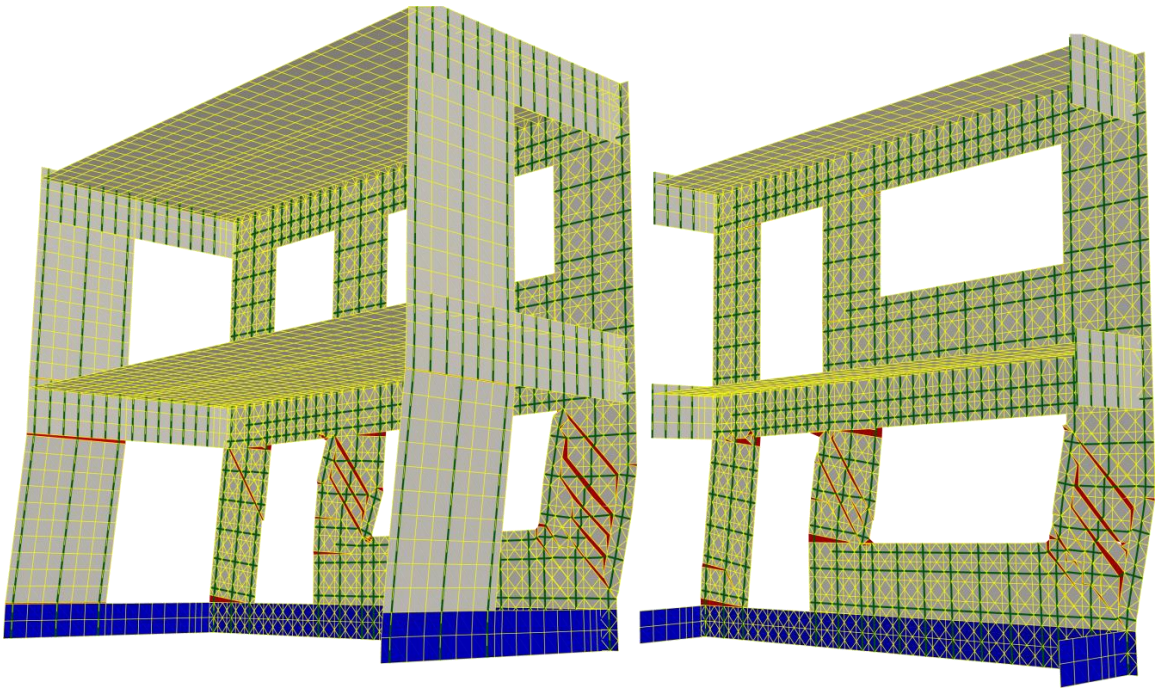

(a) (b)

Figure 5.35 – Deformed mesh of the structure for positive drift from pushover analyses: a) with out-of-plane walls, b) without out-of-plane walls

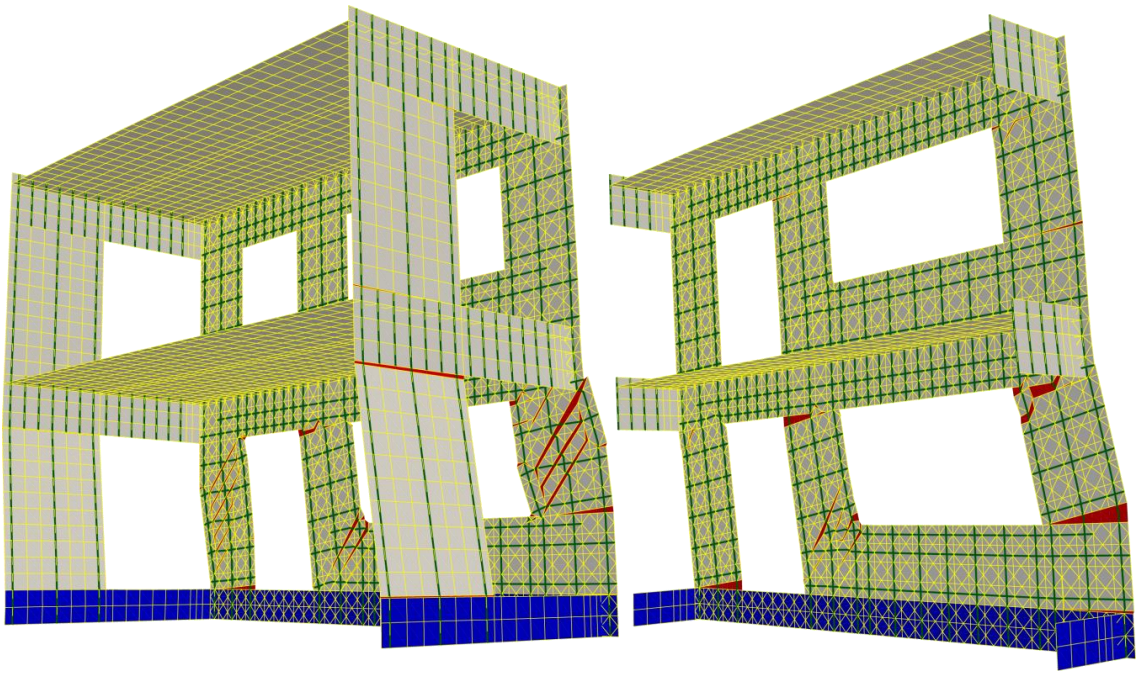

(a) (b)

Figure 5.36 – Deformed mesh of the structure for negative drift from pushover analyses: a) with out-of-plane walls, b) without out-of-plane walls

6. SUMMARY AND CONCLUSIONS

6.1. Summary

This dissertation aims to provide insight on the seismic performance of reinforced masonry structural wall systems through experimental and numerical investigations. Experimental data from the shake-table testing of a full-scale two-story reinforced masonry structure that had been designed with the displacement-based method by Ahmadi et al. (2013a, 2013b) have been analyzed and interpreted. Additionally, a new finite element modeling scheme has been developed in this research to analyze the nonlinear behavior of reinforced masonry structures. The modeling scheme has been validated by results of quasi-static tests conducted on reinforced masonry wall segments and the aforementioned shake-table testing of the two-story wall structure. The finite element analysis results have provided additional understanding of the seismic performance of the two-story structure, which cannot be directly acquired from the test data. An additional numerical study has been performed with the finite element model to evaluate the performance of the two-story structure redesigned with the code-based approach.

The validation of the displacement-based design is one of the main goals of the shake-table tests conducted on the two-story structure. The uniaxial shake-table facility at the University of California at San Diego was used for the experimental study. The two-story structure consisted of one wall parallel to the direction of shaking and two walls perpendicular to the directions of shaking. The former resisted the horizontal seismic forces by in-plane action while the latter by out-of-plane action. The in-plane wall had

three wall components separated by a door opening and a window opening in each story, while each of the out-of-plane walls had two door openings in each story. The two wall components in the in-plane wall adjacent to the window opening were expected to be shear-dominated, and the displacement limits used in the design were based on the shear-dominated behavior. The structure was subjected to a sequence of ground motion records of increasing intensity up to the MCE level.

The finite element modeling scheme proposed here consists of smeared-crack shell elements, which adopt a plasticity law to describe the compressive behavior of the uncracked material and an orthotropic law for the cracked material. To better capture the behavior of diagonal shear and sliding cracks, discrete cohesive interface elements have been employed. The interfaces are placed horizontally and diagonally to be able to capture flexural, sliding, and shear cracks. The reinforcement is simulated with truss elements with a uniaxial constitutive law that can reproduce the cyclic behavior of steel. In order to simulate the bond-slip and the dowel action behavior of the reinforcement, a special interface element has been developed. This bond-slip/dowel action interface connects the truss elements to the shell elements. It employs two uncoupled constitutive laws to describe the bond-slip and dowel action behavior independently.

6.2. Main observations and conclusions

The experimental investigation has shown that the two-story structure tested on the shake table behaved as expected under the design-level earthquake. The maximum displacements were within the design limits and the structure had only minor cracking. The deformations of the wall components were dominated by flexure with the yielding of

some vertical reinforcing bars. At the MCE level, the structure suffered extensive damage with severe diagonal cracking in the two wall components adjacent to the window opening in the bottom story. The structural displacements considerably exceeded the design limits used for the MCE level. However, the structure did not collapse.

There is strong evidence that the exterior walls perpendicular to the direction of shaking had a significant contribution to the lateral load resistance of the structure. They exerted additional axial compression on the in-plane wall components as the latter rocked. This increase of axial compression increased the flexural and shear strengths of the wall components. Based on the finite element analyses, the out-of-plane walls could have increased the base shear capacity of the structure by a factor of 1.7.

A redesign of the structure using the code-compliant forced-based approach results in a lower amount of vertical reinforcement in the walls. The amount of vertical and horizontal reinforcement will be further lowered if the prescriptive reinforcement spacing requirements of the MSJC code are not followed. Since it has been shown that the two short wall components adjacent to the window opening are shear-dominated, any reduction in the reinforcement would result in a lower resistance and worse performance.

The numerical results have demonstrated the capability of the finite element modeling scheme to capture the flexure-, shear- and sliding-dominated behaviors of reinforced masonry walls. The models can predict accurately the initial stiffness, the load capacity, the strength degradation, the post peak behavior, and the hysteretic energy dissipation of the walls that were tested quasi-statically. Moreover, the analyses capture the failure mechanism and the evolution of damage experienced by the walls, including the crack pattern and the crushing of the masonry.

The importance of introducing the cohesive interface elements and the bond-slip/dowel-action interface elements to the finite element model depends on the failure mechanism of the wall. It has been demonstrated that in the absence of the bond-slip/dowel-action interfaces, the capacity and the overall behavior of walls dominated by diagonal shear or sliding can be significantly affected. However, the impact is negligible for flexure-dominated walls. When the discrete cohesive interfaces are omitted, the model overestimates the strength, ductility, and hysteretic energy dissipation for shear-dominated walls.

The finite element modeling scheme successfully predicts the complex three-dimensional behavior of the two-story reinforced masonry structure tested on the shake-table. The numerical results have confirmed the significant influence of the out-of-plane walls on the lateral resistance of the structure. Although the direct contribution of the out-of-plane walls through their bending capacity is insignificant, their indirect contribution by increasing the axial compressive loads on the in-plane wall components can be as high as 25% of the total base shear capacity.

Finally, the numerical investigation of the displacement-based and force-based designs has shown that under the same seismic loading, the latter results in higher inter-story drifts. However, both designs seem to produce adequate performance. One factor that contributes to the adequate performance of the force-based design is that the beneficial influence of the out-of-plane walls has been ignored in the force-based design. This has made the design more conservative.

REFERENCES

Abrams, D.P. and Paulson, T.J. Modeling Earthquake Response of Concrete Masonry Building Structures. *ACI Structural Journal*, 88, 4 (1991), 475-485.

Ahmadi, F. *Displacement-based Seismic Design and Tools for Reinforced Masonry*. Ph.D Thesis, Department of Civil Engineering, The University of Texas at Austin, 2012.

Ahmadi, F., Mavros, M., Klingner, R. E., Shing, P. B., and McLean, D. Displacement-based Seismic Design for Reinforced Masonry Shear-wall Structures, Part 1: Background and Trial Application. *Earthquake Spectra*, 31, 2 (2013a), 969-998.

Ahmadi, F., Mavros, M., Klingner, R. E., Shing, P. B., and McLean, D. Displacement-based Seismic Design for Reinforced Masonry Shear-wall Structures, Part 2:Validation with Shake-table Tests. *Earthquake Spectra*, 31, 2 (2013b), 999-1019.

Aristizabal-Ochoa, J. D. Cracking and Shear Effects on Structural Walls. *Journal of Structural Engineering* , 109, 5 (1983), 1267-1277.

ASCE 7-10. *Minimum design loads for buildings and other structures.* ASCE, Reston, Va., 2010.

Bazant, Z. P. and Oh, B. H. Crack Band Theory for Fracture of Concrete. *Materials and Structures*, 16, 3 (1983), 155-177.

Bruggi, M. Generating strut-and-tie patterns for reinforced concrete structures using topology optimization. *Computers & Structures*, 87, 23-24 (2009), 1483-1495.

Burchnall, D. *Formulation and Validation of a Nonlinear Shell Element for the Analysis of Reinforced Concrete and Masonry Structures*. MS Thesis, Virginia Polytechnic Institude and State University, Blacksburg, VA, 2014.

Clough, R. W., Benuska, K. L., and Wilson, E. L. Inelastic Earthquake Response of Tall Buildings. (Auckland and Wellington, New Zealand 1965), Proceedings of the Third Word Conference on Earthquake.

Cyrier, W. B. *Performance of Concrete Masonry Shear Walls With Integral Confined Concrete Boundary Elements*. MS Thesis, Department of Civil and Enviromental Engineering, Washington State University, 2012.

Dei Poli, S., Di Prisco, M., and Gambarova, P.G. Dowel Action as a Means of Shear Transmission in RC Elements: a State of the Art and New Test Results. *Sudi e Ricerche, Scholl for the Design of R/C Structures, Milan University of Technology* (1988), 217-

303.

Dodd, L. L. and Restrepo-Posada, J. I. Model for Predicting cyclic behavior of reinforcing steel. *Journal of Structural Engineering*, 121 (1995), 433-445.

Giberson, M. F. *The Response of Nonlinear Multi-Story Structures Subjected to Earthquake Excitation*. Ph.D Thesis, California Institude of Technology, Pasadena, California, 1967.

Hilber, H. M., Hughes, T. J. R., and Talor, R. L. Improved Numerical Dissipation for Time Integration Algorithms in Structural Dynamics. *Earthquake Engineering and Structural Dynamics*, 5 (1977), 282-292.

Hrennikof, A. Solution of Problems of Elasticity by the Framework Method. *Journal of Applied Mechanics*, 8, 4 (1941), 169-175.

Hsu, T. T. *Unified Theory of Reinforced Concrete*. CRC Press, 1993.

Kaba, S. and Mahin, S. *Refined Modeling of Reinforced Concrete Columns of Seismic Analysis*. Earthquake Engineering Research Center, University of California, Berkeley, 1984.

Kapoi, C. M. *Experimental Performance of Concrete Masonry Shear Walls Under In-Plane Loading*. MS Thesis, Department of Civil and Enviromental Engineering, Washington State University, 2012.

Keshavarzian, M. and Schnobrich, W. C. Computed Nonlinear Analysis of R/C Coupled Shear Walls. *Earthquake Engineering & Structural Dynamics*, 13, 4 (1985), 695-702.

Kim, S. H. *Cyclic Uniaxial Constitutive Model for Steel Reinforcement*. MS Thesis, Department of Civil and Enviromental Engineering, Virginia Polytechnic Institude and State University, 2015.

Kottari, A. 2015. Personal Communication.

Koutromanos, I. *Numerical Analysis of Masonry-Infilled Reinforced Concrete Frames Subjected to Seismic loads and Experimental Evaluation of Retrofit Techniques." Ph.D. Dissertation*. Ph.D Thesis, University of California, San Diego, La Jolla, CA, 2011.

Koutromanos, I. 2015. Personal Communication.

Koutromanos, I. and Shing, P. B. A cohesive crack model to simulate cyclic response of concrete and masonry structures. *ACI Structural Journal* (2011).

Leiva, G. and Klingner, R.E. *In-Plane Seismic Resistance of Two-Story Concrete Masonry Shear Walls with Openings*. United States-Japan Coordinated Program for Masonry Building Research, The University of Texas at Austin, Austin, Texas, 1991.

Lotfi, H. R. and Shing, P. B. An appraisal of smeared crack models for masonry shear wall analysis. *Journal of Computers and Structures*, 41 (1991), 413-425.

Mahin, S., Bertero, V., and Vitelmo, V. *An evaluation of some methods for predicting seismic behavior of reinforced concrete buildings*. Earthquake Engineering Research Center, University of California, Berkeley, 1975.

Mansour, M. and Hsu, T. T. Behavior of Reinfroced Concrete Elements under Cyclic Shear. II: Theoretical Model. *Journal of Structural Engineering*, 131, 1 (2005), 54-65.

Massone, L. and Wallace, J. Load-Deformation Responses of Slender Reinforced Concrete Walls. *ACI Structural Journal*, 101, 1 (2004), 103-113.

Mavros, M., Ahmadi, F., Shing, P. B., Klingner, R., McLean, D., and Stavridis, A. Shake-table Tests of a Full scale Two-story Shear-dominated Reinforced Masonry Wall Structure. *Journal of Structural Engineering* (2015 (under review)).

Mazars, J., Kotronis, P., and Davenne, L. A new modelling strategy for the behaviour of shear walls under dynamic loading. *Earthquake Engineering & Structural Dynamics*, 31, 4 (2002), 937-954.

Mehrabi, A. and Shing, P. B. Finite Element Modeling of Masonry-Infilled RC Frames. *Journal of Structural Engineering*, 123, 5 (1997), 604-613.

Menegotto, M. and Pinto, P. E. *Method of Analysis for Cyclically Loaded Reinforced Concrete Plane Frames Including Changes in Geometry and Non-Elastic Behavior of Elements under Combined Normal Force and Bending*. IABSE, Final Report, Lisbon., 1973.

Miki, T. and Niwa, J. Nonlinear Analysis of RC Structural Members Using 3D Lattice Model. *Journal of Advanced Concrete Technology*, 2, 3 (2004), 343-358.

Moharrami, M., Koutromanos, I., Panagiotou, M., and Girgin, S. C. Analysis of Shear-Dominated RC Columns Using the Nonlinear Truss Analogy. *Earthquake Engineering & Structural Dynamics* (2014), 677-694.

Morsch, E. Der eisenbetonbau-seine theorie und anwendung (Reinforced concrete construction – theory and application) (1920).

MSJC. *Building Code Requirements for Masonry Structures (TMS 402-13/ACI 530-*

13/ASCE 5-13) Specification for Masonry Structures (TMS 602-13/ACI 530.1-13/ASCE 6-13) and Companion Commentaries. The Masonry Society, Boulder, Colorado, the American Concrete Institute, Farmington Hills, Michigan, and the American Society of Civil Engineers, Reston, Virginia., 2013.

Murcia-Delso, J. and Shing, P. B. Bond-slip model for detailed finite element analysis of reinforced concrete structures. *Journal of Structural Engineering*, 141, 4 (2014).

Niwa, J., Choi, I. C., and Tanabe, T. A. Analytical Study for Shear Resisting Mechanism Using Lattice Model. *Journal of Materials, Concrete Structures and Pavements* , 26, 508 (1995), 95-109.

Otani, S. and Sozen, M. A. *Behavior of Multistory Reinforced Concrete Frames During Earthquake*. University of Illinois, Urbana, Illinois, 1972.

Panagiotou, M., Restrepo, J. I., Schoettler, M., and Kim, G. Nonlinear Cyclic Truss Model fro Reinforced Concrete Walls. *ACI Structural Journal*, 109, 2 (2012), 205-214.

Paulay, T., Park, R., and Philips, M. H. Horizontal Construction Joints in Cast in Place Reinforced Concrete. *ACI-Special Publication SP-42, Shear in reinforced concrete*, 2 (1974), 599-616.

Priestley, M. J. N., Calvi, G. M., and Kowalsky, M. J. *Direct Displacement-Based Seismic Design of Structures*. Pavia, 2007.

Ritter, W. Die Bauweise Hennebique. *Schweizerische Bauzeitung*, 33, 7 (1899), 59-61.

Rots, J. G. and Blaauwendraad, J. Crack Models for Concrete: Discrete or Smeared? Fixed, multi-directional or rotating? *Heron*, 34, 1 (1989).

Roufaiel, M. S. and Meyer, C. Analytical Modeling of Hysteretic Behavior of R/C Frames. *Journal of Structural Engineering*, 113, 3 (1987), 429-444.

Saatcioglu, M., Derecho, A. T., and Corley, W. G. Parametric Study of Earthquake-resistant Coupled Walls. *Journal of Structural Engineering*, 113, 1 (1987), 141-157.

Saidi, M. and Sozen, M. A. *Simple and complex models for nonlinear seismic response of reinforced concrete structures*. Report to the National Science Foundation, University of Illinois at Urbana-Champaign, Champaign, IL, 1979.

Satyarno, I., Carr, A. J., and Restrepo. Refined pushover analysis for the assessment of older reinforced concrete buildings. In *NZSEE Technology Conference* (Wairakei, New Zealand 1998), 75-82.

Seible, F., Hegemier, A., and Kingsley, G. Simulated Seismic-Load Tests on Full-Scale Five-Story Masonry Building. *Journal of Structural Engineering*, 120, 3 (1994a), 903-924.

Seible, F., Priestley, N., Kingsley, G., and Kurkchubashe, A. Seismic response of full-scale five-story reinforced masonry building. *Journal of Structural Engineering*, 120, 3 (1994b), 925-947.

Sherman, J. D. *Effects of Key Parameters on the Performance of Concrete Masonry Shear Walls Under In-Plane Loading*. MS Thesis, Department of Civil and Enviromental Engineering, Washington State University, 2011.

Shing, P. B., Noland, J. L., Klamerus, E., and Spaeh, H. Inelastic Behavior of Concrete Masonry Shear Wall. *Journal of Structural Engineering*, 115, 9 (1989), 2204-2225.

Shing, P. B., Noland, J. L., Spaeh, H. P., Klamerus, E.W., and Schuller, M. P. *Response of Single-Story Reinforced Masonry Shear Walls to In-plane Lateral Loads*. Report, Department of civil, environmental and architectural engineering University of Colorado, 1991.

Spacone, E. and Filippou, F. C. Fibre Beam-Column model for Non-Linear Analysis of R/C Frames: Part I. Formulation. *Earthquake Engineering and Structural Dynamics* , 25, 7 (1996), 711-725.

Stavridis, A., Ahmadi, F., Mavros, M., Shing, P. B., Klingner, R., and McLean, D. Shake-table Tests of a Full-scale Three-story Reinforced Masonry Shear Wall Structure. *Journal of Structural Engineer* (2015 (under review)).

Takayanagi, T. and Schnobrich, W. Computed Behavior of Reinforced Concrete Coupled Shear Walls. *Structural Research Series 434* (1976).

Taylor, R. L. *FEAP-Finite Element Analysis Program, Version 8.4*. 2014.

Vecchio, F. J. and Collins, M. P. The modeified Compression-Field Theory for Reinfroced Concrete Elements Subjected to Shear. *ACI Journal*, 83, 2 (1986), 219-231.

Vintzeleou, E. and Tassios, T. P. Behaviour of Dowels Under Cyclic Deformations. *ACI, Structural Journal*, 84 (1987), 18-30.

Voon, K. C. *In-plane Seismic Design of Concrete Masonry Structures*. Ph.D Thesis, University of Auckland, New Zealand, 2007.

Voon, K. C. and Ingham, J. M. Experimental In-plane Shear Strength Investigation of Reinforced Concrete Masonry Walls. *Journal of Structural Engineering*, 132, 3 (2006),

400-408.

Wight, G. D., Kowalsky, M. J., and Ingham, J. M. Shake Table Testing of Posttensioned Concrete Masonry Walls with Openings. *Journal of Structural Engineering*, 133, 11 (2007), 1551-1559.

Zeris, C. A. and Mahin, S. A. Behavior of Reinforced Concrete Structures Subjected to Biaxial Excitation. *Journal of Structural Engineering*, 117, 9 (1991), 2657-2673.